Protein-Protein Interactions Regulate Iron Homeostasis in *Pseudomonas aeruginosa*

By

Yan Wang

Submitted to the graduate degree program in the Department of Chemistry and the Graduate Faculty of the University of Kansas in partial fulfillment of the requirements for the degree of Doctor of Philosophy.

Chairperson: Mario Rivera, Ph.D.

Krzysztof Kuczera, Ph.D.

David Benson, Ph.D.

Yong Zeng, Ph.D.

Blake Peterson, Ph.D.

Date Defended: May11, 2015

The Dissertation Committee for **Yan Wang**

certifies that this is the approved version of the following dissertation:

Protein-Protein Interactions Regulate Iron Homeostasis in *Pseudomonas aeruginosa*

_____

Chairperson: Mario Rivera, Ph. D.

Date approved May 11, 2015

ABSTRACT

Our lab had previously shown that the interaction between bacterioferritin (BfrB) and its associated ferredoxin (Bfd) enables mobilization of iron stored in BfrB. My research was aimed at understanding the mechanism of the BfrB-Bfd interaction and how this interaction facilitates electron transfer into the ferric core in BfrB for subsequent mobilization of Fe^{2+} from the core. Results from biochemical and structural studies allowed us to conclude that the BfrB-Bfd interaction enables heme-mediated electron transfer from the [2Fe-2S] cluster in Bfd to the Fe^{3+} mineral stored in BfrB. The Bfd fold was revealed for the first time in the X-ray crystal structure of BfrB-Bfd complex. The crystal structure revealed that Bfd has a helix-turn-helix fold, which is distinct from the canonical ferredoxin fold. Analysis of the structure, followed by studies in solution showed that the [2Fe-2S] cluster in Bfd is important to stabilizing the Bfd fold. In addition, evidence from X-ray crystallography, *in vitro* assays, and *in silico* experiments, showed that Bfd is also stabilized by the binding of a phosphate anion. The crystal structure of the BfrB-Bfd complex showed that 12 Bfd molecules bind a 24-mer BfrB, with each heme binding almost immediately above each of the 12 hemes in BfrB. The crystal structure of the BfrB/Bfd complex also allowed us to identify the residues from each of the two proteins that participate at the complex interface, and to analyze specific interactions among these residues. The interaction between BfrB and Bfd was also characterized in solution by surface plasmon resonance (SPR) and isothermal titration calorimetry (ITC). The results show Bfd binds at each of the sites on BfrB with K_d of ~ 3 μM, in an association that is driven entropically. In addition, contributions of the residues that participate at the BfrB-Bfd complex

interface were evaluated in solution, which led to the identification of the hotspot for the BfrB-Bfd interaction.

ACKNOWLEDGEMENTS

I am extremely appreciative of Prof. Mario Rivera for giving me this opportunity to work in his laboratory for all these years, which has been an invaluable life experience to me and enabled me to have learned and grown a lot. I am very grateful for his guidance, encouragement and patience to me all the time. His encouragement motivated me through my difficult times. From him, I learned how to think scientifically and how to solve scientific problems.

I also would like to extend my sincere gratitude for my committee members Dr. David Benson, Dr. Krzysztof Kuczera, Dr. Yong Zeng and Dr. Blake Peterson for their precious time and kind advice.

I also would like to extend my deepest gratitude to all our collaborators, especially Dr. Scott Lovell who solved all the crystal structures of my proteins and helped me to understand crystallography; Dr. Na Zhang who taught me to use SPR and helped me to initiate my project using SPR; Dr. Yuan Cheng, who taught me to use ITC and helped me with my projects; Dr. Ryan Kramer who taught me to use CD; and Dr. Russ Middaugh and Dr. Phillip Gao for allowing me to use their instruments.

I also feel very grateful for Dr. Huili Yao, who tremendously helped me from the beginning to the end. I feel very lucky to be able to work with her and learn from her. Many thanks to her for giving me so many suggestions and leading me through so many trouble-shooting processes. I really enjoyed discussing my projects with her.

I greatly appreciate the support and friendship of the past and present members of Rivera group: Dr. Saroja Weeratunga, Dr. Juan Carlos Rodriguez, Dr. Grace Jepkorir, Dr. Ritesh Kumar, Kate Eshelman, Pavithra Vani Nama, Mary Erickson, Harshani Wijerathne, Achala Dharmasiri, Kena Senegal and Pearl Ashitey. I am very happy to work with you all. Especially, I really appreciate that Dr. Saroja Weeratunga taught me all the experimental techniques when I entered the group. She was very helpful to me and also gave me a lot of mental support. In addition, many thanks to Kate Eshelman for helping me with my English writing.

Also, I would like to thank my dear friend Congcong Chai, who accompanied me and supported me to pass the most difficult time approaching my graduation.

In addition, I sincerely thank my parents, who live in China and stand for not being able to see me for all these years, but always supported me without any complains.

Finally, I would like to thank everyone who helped me in many ways during my Ph.D. study.

TABLE OF CONTENTS

CHAPTER I **1**

INTRODUCTION

Antibiotic Resistance 1

Bacterial Iron Homeostasis 2

Bacterial Ferritin and Bacterioferritin are Regulators of Intracellular Iron Levels 3

Genomic Studies Suggest that Iron Mobilization from Bfr Requires Protein-Protein Interactions 7

In Vitro Evidence of the Bfr-Bfd Interaction 8

Pa BfrB-Bfd Interaction Model 9

Pa-Bfd Facilitates the Mobilization of Core Iron from Pa-BfrB 12

Heme Mediates Electrons to the BfrB Ferric Core 13

Role of [2Fe-2S] Cluster in BfrB Iron Mobilization 15

RESEARCH PROBLEM AND RATIONALE 18

REFERENCES 20

CHAPTER II **25**

Characterizing the Structure and Function of Pa-Bfd

INTRODUCTION 25

EXPERIMENTAL PROCEDURES 30

Preparation of Apo-Bfd 30

BfrB iron release study with apo-Bfd 30

Pa-Bfd transfers electrons to Pa-BfrB 31

Removal of phosphate from Pa- Bfd 31

Removal of phosphate from Pa- Bfd in presence of Zn^{2+} 31

Characterization of Pa-Bfd, Pa apo-Bfd in phosphate buffer and in Tris-Base buffer by Circular Dichroism Spectroscopy 32

Crystallization of Pa BfrB-Bfd complex 32

Truncation of Pa-Bfd (M1-L56) 33

Crystallization of truncated-Bfd 34

RESULTS 34

Characterizations of apo-Bfd 34

The role of the [2Fe-2S] cluster in the Mobilization of Iron from BfrB 36

The Bfd Fold 41

C-terminal truncated Bfd fold 42

The Bfd fold is stabilized by phosphate 45

Overall Structure of the BfrB-Bfd complex 51

The Pa-BfrB−Bfd Interface 52

Bfd [2Fe-2S] cluster electron transfer pathway to the BfrB heme 56

Discussion 58

Bfd fold is a versatile metal binding motif 58

Phosphate is important for stabilizing the Bfd fold 60

References 62

CHAPTER III 64

Identifying the Hot Spot for the Interaction between Bacterioferritin (BfrB) and Its Associated Ferredoxin (Bfd)

INTRODUCTION 64

EXPERIMENTAL PROCEDURES 68

Site-Directed Mutagenesis 68

Protein Expression and Purification 69

BfrB Mutations Crystallization and Data Collection 71

Measurement of the BfrB-Bfd Binding Affinity by Surface Plasmon Resonance 77

Measurement of the BfrB-Bfd Binding Affinity by Isothermal Titration Calorimetry 78

Mobilization of iron from BfrB 78

RESULTS 78

Characterization of the BfrB-Bfd Interaction by SPR 78

Characterization of the BfrB:Bfd interaction in solution by ITC 84

Dissecting the Interacting Surface of the BfrB:Bfd Complex 87

Biochemical characterization of BfrB mutants 88

Mobilization of core iron from the BfrB mutants is compromised 91

The BfrB mutants have significantly reduced affinity for Bfd 94

X-Ray Crystal Structures of Mutant BfrB 97

Mutations on Bfd 98

Discussion 102

Bfd fold is a versatile metal binding motif 102

Phosphate is important for stabilizing the Bfd fold 103

References 104

CHAPTER IV 109

Fragment Based Drug Design for Disrupting BfrB-Bfd Interactions

INTRODUCTION 109

EXPERIMENTAL PROCEDURES 113

Mobilization of iron from BfrB in the presence of compounds 113

RESULTS 114

Inhibition effects on BfrB iron mobilization 114

Discussion 124

Factors affecting the BfrB iron mobilization efficiency 124

References 126

LIST OF TABLES

CHAPTER 1

Table 1-1	*bfr -bfd* gene proximity in several pathogens	8

CHAPTER 2

Table 2-1	Crystallographic data of C-terminal truncated Bfd 43	43
Table 2-2	Crystallographic data for BfrB-Bfd refined to 2.0Å resolution.	51
Table 2-3A	Sequence alignment of *Pa*-Bfd with Bfd-like molecules from different bacterial species. Conserved cysteine residues coordinating iron in the [2Fe-2S] cluster are highlighted by an arrow (↓) and residues buried at the *Pa*-BfrB-Bfd interface are denoted by (^). Conserved residues across the alignment are in red, conservative substitutions in green and semi-conservative substitutions in blue, sequence numbering according to *Pa*-Bfd	54
Table 2-3B	Sequence alignment of *Pa*-BfrB and Bfr from different bacterial species. Residues buried at the *Pa*-BfrB-Bfd interface are denoted by (^). Conserved residues across the alignment are in red, conservative substitutions in green and semi-conservative substitutions in blue.	55

CHAPTER 3

Table 3-1	Crystallographic data for BfrB E81A refined to 2.50 Å resolution.	72
Table 3-2	Crystallographic data for BfrB L68A refined to 2.20 Å resolution	73
Table 3-3	Crystallographic data for BfrB E85A refined to 2.55 Å resolution	74
Table 3-4	Crystallographic data for BfrB L68A/ E81A refined to 1.60 Å resolution	76
Table 3-5	Thermodynamics and kinetics of the BfrB-Bfd Binding	82
Table 3-6	Initial iron release rates and binding affinities of wild type and mutant BfrB-Bfd interactions	96

LIST OF FIGURES

CHAPTER 1

Figure 1-1	Schematic representation of bacterial iron homeostasis: Iron storage proteins likely regulate the intracellular iron levels to avoid the occurrence of the Haber-Weiss cycle.	4
Figure 1-2	Structural organization of Bfr and Ftn. (A) 24-mer assembly of Pa-FtnA (PDB:3R2K) (B) 24-mer assembly of Pa-BfrB (PDB:3IS7). (C) A subunit dimer of Pa-BfrB harboring a heme molecule (green). (D) Heme (green) is deeply buried below the Pa-BfrB protein shell surface\	6
Figure 1-3	Model of electron transfer across the Pa-BfrB shell to reduce Fe^{3+} mineral and promote release of Fe^{2+}	9
Figure 1-4	(A) Ferroxidase center of Pa-BfrB. (B) Proposed iron uptake and oxidation mechanism in Pa-BfrB	11
Figure 1-5	Binding of Pa-Bfd is necessary to promote Fe^{2+} mobilization from Pa-BfrB. (A) Normalized iron release from Pa-BfrB in the presence of Pa-Bfd (black) and without Pa-Bfd (red). (B) Time-dependent changes in the heme Soret band position upon the addition of NADPH in the presence of Pa-Bfd (black) and in the absence of Pa-Bfd (red).	13
Figure 1-6	Pa-Bfd facilitates heme mediated electron transfer to the Pa-BfrB ferric core. Time-dependent wavelength shift of the heme Soret band (red) and time–dependent increases of A_{523}	14

	upon the addition of each aliquot of NADPH (blue)	
Figure 1-7	Apo-Bfd (made *in situ*) facilitates BfrB iron mobilization (blue) in a way similar as holo-Bfd (red). Without Bfd, the iron mobilization from BfrB is slow (black)	16
Figure 1-8	Proposed model for BfrB iron mobilization where the electron transfer of FPR to BfrB heme is facilitated by apo-Bfd recruiting the FPR to the BfrB surface.	17

CHAPTER 2

Figure 2-1	[2Fe-2S] cluster coordinated by four cysteines.	26
Figure 2-2	Sequence alignment of different types of ferredoxins (Adapted from *J Bioenerg Biomembr*, 1994. 26(1): p. 67-88).	26
Figure 2-3	Example UV-vis spectra of [2Fe-2S] cluster ferredoxins ((Adapted from *J Biol Chem*, 1992. 267(16): p. 11120-5).	27
Figure 2-4	UV-vis spectrum of isolated Pa- Bfd with oxidized [2Fe-2S] cluster shows four characteristic peaks at 334 nm, 424 nm, 465 nm and 560 nm	28
Figure 2-5	Alignment of Bfd sequence in different bacteria shows that there are four conserved cysteines (red) arranged in C-X-C-X_{31-32}-C-X_2-C fold.	29
Figure 2-6	Mass spectrum of isolated apo-Bfd.	35

Figure 2-7 (A) UV-vis spectra of Pa-Bfd in 50 mM potassium phosphate pH 7.0 (black) and apo-Bfd in 200 mM potassium phosphate pH 7.0 and 5 mM TCEP (red). (B) Far UV CD spectra of Pa-Bfd in 50 mM potassium phosphate pH 7.0, 4 mM NaCl, and 0.13 mM DTT (blue) and Pa apo-Bfd in 200 mM Tris, pH 7.0, 120 mM NaCl and 1 mM TCEP (black). 36

Figure 2-8 Time dependent increase of Pa-BfrB iron release percentage containing: (blue) Pa-BfrB 0.25 μM), Pa-FPR (10 μM), and apo Pa-Bfd (10 μM). (black) Pa-BfrB (0.25 μM), Pa-FPR (10 μM), apo-Pa-Bfd (10 μM), $(NH4)_2Fe(SO_4)_2$ (20 μM), and Na_2S (20 μM); (red) Pa-BfrB (0.25 μM), Pa-FPR (10 μM), $(NH4)_2Fe(SO_4)_2$ (20 μM), and Na_2S (20 μM) 38

Figure 2-9 (A) UV-vis spectra of 30 μM oxidized Pa-Bfd (black) and reduced Pa-Bfd (red) upon addition of 0.8 equiv of sodium dithionite relative to oxidized Pa-Bfd. (B) Spectral change upon addition of 0.08 μM iron loaded Pa-BfrB (590 iron/protein) to the reduced Pa-Bfd: (red) spectrum prior to addition of Pa-BfrB. (blue) 20s, (pink) 1min, (green) 3min and (black) 5min after the addition of Pa-BfrB. (C) Difference spectrum (red) obtained from subtracting a spectrum obtained from 0.08 μM Pa-BfrB from the black trace (5min) in Figure (B). The resulted difference spectrum (red) is identical as the original oxidized Pa-Bfd at 30 μM (black). (D) Time dependent formation of $[Fe(bipy)_3]^{2+}$ complex due to the release of the Fe^{2+} during the reaction. 40

Figure 2-10	Pa-Bfd structure as a part of the Pa BfrB-Bfd complex (A) The asymmetric unit contains three BfrB subunit dimers, each of which associates with a Pa-Bfd molecule (cyan). (B) *Fo-Fc* omit map contoured at 3σ showing the electron density (magenta) of Bfd chain G. (C) Helix-turn-helix structure of Pa-Bfd. (D) The [2Fe-2S] cluster in Pa-Bfd is coordinated by C4 and C6 from L1, and C38 and C41 from L3.	42
Figure 2-11	(A) In the asymmetric unit, there are two truncated Bfd molecules. (B) The truncated Bfd structure (pink) is identical to the full-length Bfd structure (cyan)	44
Figure 2-12	(A) In the asymmetric unit, BfrB (gray) binds Bfd (chain I, G and H). Bfd chain G and I experience crystal contacts (red). (B) Main chain average B-factors in Bfd chains G (magenta), I (orange) and H. The Cys ligands are highlighted by the vertical lines. The gap in the green trace (chain H) represents the missing electron density in chain H.	45
Figure 2-13	(A) The missing electron density in chain H is represented by gray color. (B) Electron density modeled as a phosphate ion is observed in chain G. The phosphate ion is coordinated by R26, R29 and K46 in chain G, as well as K76 in a nearby BfrB molecule	46
Figure 2-14	(A) Bfd loses [2Fe-2S] cluster in the absence of phosphate. (B) Bfd loses helical structure in the absence of phosphate	47
Figure 2-15	Pa-Bfd loses the [2Fe-2S] cluster in the buffer of 150 mM Tris-Base, 150 mM NaCl, 5 mM TCEP, 125 μM (ZnSO4.7H2O), pH 7.8. Black: Pa-Bfd in phosphate buffer.	48

Red: 5 min of the reaction. Green: 30 min of the reaction

Figure 2-16	View of the "phosphate binding region" in truncated Bfd. (A) Overlay the structure of truncated Pa-Bfd (pink) and full-length Bfd (cyan) shows that the R26 and R29 in truncated structure have shifted compared to the full-length structure. (B) The "phosphate binding region" in the truncated Bfd is stabilized by a nearby molecule through crystal contacts.	50
Figure 2-17	Removal of the phosphate from the truncated Bfd results loss of [2Fe-2S] cluster.	50
Figure 2-18	(A) BfrB-Bfd complex structure (4E6K) shows that 12 Bfd molecules (cyan) bind to a 24-assembly BfrB molecule. (B) Alignment of the ferreoxidase center of the free BfrB (pink) and Bfd in the complex (green).	52
Figure 2-19	Per-residue plot of surface area buried at the complex interface contributed from (A) Bfd residues shown in cyan and (B) BfrB residues from subunit A (green) and subunit B (gray).	53
Figure 2-20	BfrB-Bfd interface showing the Bfd residues in cyan and BfrB subunit A and B in green and gray, respectively. The oxygen and nitrogen atoms are shown as red and blue, respectively. The H-bonding interactions are labeled with dotted lines.	56
Figure 2-21	Best electron transfer path from [2Fe-2S] cluster to heme calculated by the program Harlem.	57

Figure 2-22	[2Fe-2S] cluster transfers electron via heme to the core Fe^{3+} to mobilize Fe^{2+}	57
Figure 2-23	(A) Structural alignment of Pa-Bfd (cyan) with PDH1 (PDB:1Y56) shows that Bfd matches a proportion of the a-subunit of PDH1 (magenta). (B) Structural alignment of Bfd with a portion of the N'-terminal domain of CopZ-NT (PDB:2HU9)	59
Figure 2-24	*In silico* prediction shows the phosphate stabilizes the Pa-Bfd fold. (A) Plot of per residue mobility in the phosphate bound Bfd structure. (B) Plot of the relative change of the mean square fluctuation of Bfd residues upon removing the phosphate from the Bfd structure.	61

CHAPTER 3

Figure 3-1	Structural organization of BfrB (PDB 3IS8) and its iron mobilization model. (A) View of subunit dimer harboring a heme molecule (red), which is coordinated by a conserved methionine in each of the subunits. (B) Inside view of the BfrB interior cavity where iron mineral is stored. Heme (red) is buried below the protein shell surface with the heme propionates extending into the cavity. (C) Proposed model of iron mobilization from BfrB central cavity, which is promoted by Bfd mediated electron transfer across the protein shell to reduce the Fe^{3+} mineral to Fe^{2+}.	**66**
Figure 3-2	Structure of the BfrB-Bfd complex (PDB:4E6K). (A) View of a Bfd molecule (cyan) binding at the interface of a BfrB subunit dimer above the harbored heme molecule (red). (B)	68

	A 24-assembly BfrB binds 12 Bfd molecules. (C) View of the BfrB-Bfd interface. Bfd side chains (cyan) bury into binding clefts on the BfrB surface as well as form ionic interactions (dotted lines) with BfrB surface residues; BfrB subunit A and B are shown in green and gray respectively. O, N and S are shown in red, blue and yellow respectively.	
Figure 3-3	Measuring the affinity of the BfrB-Bfd interaction using SPR. (A) Overlay of double referenced sensorgrams resulting from the injection of different concentrations of Bfd (0~40 μM) over immobilized BfrB. (B) The BfrB-Bfd binding affinity determined by steady state affinity analysis. Responses at steady state are plotted as a function of Bfd concentrations (black circles in the top panel) and fitted to the 1:1 Langmuir model (solid line). The scatchard plot is shown in the inset. The residuals plotted in the bottom panel shows the relative response difference between the generated fit and the experimental data.	81
Figure 3-4	Kinetic analysis of the BfrB-Bfd interaction. Top panel: fits generated (black lines) by globally fitting the rate equations derived from the 1:1 Langmuir model to the association and dissociation phases of all seven injections simultaneously. Bottom panel: the relative residual errors from the fits.	83
Figure 3-5	ITC characterization of the BfrB-Bfd interaction. The top panel shows the raw ITC data and the bottom panel shows the plot of integrated area under each titration peak (black circle) fitted to the 1:1 Langmuir binding model (solid line).	87
Figure 3-6	Elution volumes (Ve) of the BfrB mutants from a calibrated Superdex 200 column. BfrB wild type (magenta) 60.2 mL;	89

	BfrB L68A 60.4 mL (blue); BfrB E81A (green) 60.3 mL; BfrB E85A (cyan) 60.5 mL; BfrB L68A/E81A (orange) 60.7 mL. Inset: A zoomed-in view of the elution volumes of the BfrB WT and mutants with calibrated molecular weight.	
Figure 3-7	Oxidized (black) and reduced (red) spectra of (A) BfrB WT, (B) L68A, (C) E81A, (D) E85A and (E) L68A/E81A.	90
Figure 3-8	Iron uptake in (A) WT BfrB (B) BfrB L68A (C) BfrB E81A (D) BfrB E85A (E) BfrB L68A/E81A	93
Figure 3-9	Bfd facilitated iron mobilization from the wild type and mutant BfrB. (A) Time-dependent plot of the percentage iron mobilized from BfrB wild type (black), E81A (green), L68A (cyan), E85A (orange) and L68A/E81A (blue). The iron release in the absence Bfd is shown in red. (B) Time-dependent change in the position of the Soret band during the iron mobilization process shown in (A). 418 nm and 425 nm represent fully oxidized and fully reduced heme respectively.	94
Figure 3-10	Measuring the binding affinity between Bfd and mutant BfrB by SPR. Overlay of double referenced sensorgrams resulting from the injections of different concentrations of Bfd (0~ 228 μM) over immobilized BfrB L68A (A), E81A (B), E85A (C) and L68A/E85A (D). (E) The steady state affinity fitting plots of Bfd binding to E81A, L68A and E85A are shown in black, red and green respectively.	96
Figure 3-11	View of wild type BfrB-Bfd interface and the Bfd binding sites on mutant BfrB surface. (A) Bfd (cyan) binds to wild type BfrB at the interface of a BfrB subunit dimer (subunit A	100

in green and subunit B in gray). BfrB E_A^{81}, L_B^{68} and E_A^{85} interact with Bfd Y2, L5 and M1 through hydrophobic interactions and electrostatic interactions; O and N atoms are shown in red and blue respectively. (B)-(E) The same view as (A) to show the Bfd binding sites on the BfrB surface upon mutating the L68 to Ala (B); E81 to Ala (C); E85 to Ala (D) and L68/E81 to Ala (E).

Figure 3-12	Structural organization of Bfd (PDB 4E6K). Y2 interacts with G8 and T10 to stabilize the hairpin containing C4 and C6 (cyan). O, N and S atoms are shown in red, blue and yellow respectively.	100
Figure 3-13	UV-vis spectra of Bfd wild type (brown) and mutant Y2F (black), L5A (red) and K40A (green)	101
Figure 3-14	Iron mobilization from BfrB in the presence of Bfd mutant Y2F (black), K40A (green) and L5A (red).	101
Figure 3-15	Identification of hotspot of the BfrB-Bfd interaction. The change in BfrB-Bfd binding free energy (ΔΔG) caused upon mutation to BfrB and Bfd are shown in (A) and (B) respectively. The hotspot residues are highlighted in (C), with O in red and N in blue.	102
Figure 3-16	X-ray crystal structures of (A) Free BfrB binding cleft filled with water molecules (blue sphere) (B) Bfd binding to the BfrB cleft to exclude water molecules to the surroundings	103

CHAPTER 4

Figure 4-1	Process of finding inhibitors to disrupt the BfrB-Bfd interaction using FBDD.	111
Figure 4-2	(A) Bfd Y2 and L5 insert into the binding pockets on the BfrB surface. (B) Iron mobilization from BfrB in the presence of 10 mM FC996 (red) compared to the control (black).	114
Figure 4-3	Iron mobilization assay in the presence of several analogs designed from the structural information obtained in the co-crystal structure of FC996 bound to BfrB (A-V). The ID and concentration of the compounds are listed in the right corner of each plot. The black trace tracks the control; the red/green traces track each compound at different concentrations.	121
Figure 4-4	Iron mobilization from BfrB in the presence of different compounds identified to bind BfrB at the Bfd binding site from an *in silico* screen of the ZINC database (A-J). The largest concentration of compound in each of the plots corresponds to a value close to the solubility of the compound in phosphate buffer containing 10% (v/v) DMSO	124

ABBREVIATIONS

Bfr	Bacterioferritin
Bfd	Bacterioferritin associated ferredoxin
BSA	Bovine serum albumin
CD	Circular dichroism
DMSO	Dimethyl sulfoxide
DTT	Dithiothreitol
Ftn	Ferritin
FPR	Ferredoxin NADP reductase
HBED	N,N'-Di(2-hydroxybenzyl)ethylenediamine-N,N'-diacetic acid monohydrochloride
Hemin	Fe^{3+} complex of protoporphyrin IX
IPTG	Isopropyl-β-D-thiogalactopyranoside
ITC	Isothermal titration calorimetry
NADPH	Nicotinamide adenine dinucleotide (phosphate)
OD	Optical Density
PCR	Polymerase chain reaction
PDB	Protein Data Bank
PMSF	Phenylmethylsulfonyl flouride
SDS PAGE	Sodium dodecyl sulfate polyacrylamide gel electrophoresis
SPR	Surface plasmon resonance
STD-NMR	Saturation transfer difference-Nuclear Magnetic Resonance
TCEP	Tris (2-carboxyethyl0_phosphine hydrochloride

CHAPTER I

Introduction

Antibiotic Resistance

Antimicrobial agents, including antibiotics and similar drugs, have been used for treating patients with infections over the last 70 years [1]. By greatly reducing the illness and death from the infections, some of the antimicrobial agents that have been used as first-line treatments for infectious diseases are decades old. This long-time usage of antibacterial drugs in human therapy and in the livestock industry caused bacteria to evolve multiple mechanisms of antibiotic resistance, currently resistance mechanisms have been observed to all of the currently available antibacterial drugs [2]. The antibiotic- resistant strains have been widely spread by cross-infections from antibiotic treated patients and animals to the general community [3]. Each year in the United States, there are at least 2 million people infected with antibiotic resistant pathogens, leading to 23,000 deaths [1]. Some of the pathogens have evolved the ability to escape the effects of multiple antibiotics and hence are called multidrug resistant (MDR) strains [3]. The emergence of MDR strains renders huge challenges for managing infections during the medical procedures [4]. To solve the severe issue of antimicrobial resistance, not only new antibiotics are needed, but also novel targets must be identified [1].

Pseudomonas aeruginosa is a member of the "ESKAPE" group (***E****nterococcus faecium*, ***S****taphylococcus aureus,* ***K****lebsiella pneumonia,* ***A****cinetobacter baumannii,* ***P****seudomonas aeruginosa and* ***E****nterobacter spp).* These MDR strains are called "ESKAPE" to emphasize their ability to escape the effects of multiple antimicrobial reagents. "ESKAPE" pathogens account for a major percent of nosocomial infections. For example, *Pseudomonas aeruginosa* is

a Gram-negative opportunistic pathogen that can cause severe nosocomial infections in immuncompromised patients (*i.e.* causing chronic lung infections in ~90% of cystic fibrosis patients, burn victims and cancer patients [5]). Each year in the United States, there are 51,000 infections caused by *Pseudomonas aeruginosa.* 6,700 of these infections are multidrug resistant and have led to 440 deaths [1]. In an effort to contribute toward solving the issue of MDR infections caused by *Pseudomonas aeruginosa*, our group has initiated efforts aimed at exploring bacterial iron homeostasis as a possible target for development of novel antibiotics.

Bacterial Iron Homeostasis

Iron is an essential nutrient for bacteria to survive. It participates in multiple bacterial metabolic processes including respiration, nitrogen fixation, photosynthesis, DNA synthesis and repair [6, 7]. Iron is the fourth most abundant metal in the earth's crust; however, in the presence of oxygen it exists as insoluble Fe^{3+} (~ 10^{-18} M at pH 7.0), leading to limited bioavailability for many organisms [6, 8, 9]. Pathogenic bacteria must obtain iron from the host, but the free iron concentration in humans is maintained extremely low (~ 10^{-10} M) [10]. During infections, the free iron level in the host is even further reduced in order to deny this nutrient to invading pathogens, which is a strategy called "nutritional immunity" [11-13]. In response, pathogens have developed sophisticated mechanisms to obtain and utilize the iron from the host [6, 14-17]. In addition, it has been found that increasing availability of free iron during the pathogen infection would result in increasing virulence [18, 19]. Based on the intense competition for iron between host and bacteria, bacterial iron acquisition and homeostasis are regarded as having high potentials to serve as new targets for antibiotic development [20-22]. In order to approach to this goal, it is essential to gain fundamental understanding of iron regulation mechanisms in bacteria.

Bacterial iron homeostasis includes the regulation of iron acquisition, utilization and storage [8, 23]. Significant research has been done to improve our understanding of iron acquisition processes [24-27]. In comparison, knowledge is significantly more limited regarding the regulation of intracellular iron levels. As mentioned above, iron in the oxidized state, Fe^{3+}, has very low solubility and hence low bioavailability under physiological conditions. On the other hand, Fe^{2+} is quite soluble (~0.1 M at pH 7.0). However, free Fe^{2+} in cells can induce oxidative stress by catalyzing the Haber Weiss Cycle and generate the highly toxic hydroxyl radical [9]:

$$Fe^{2+} + H_2O_2 \rightarrow Fe^{3+} + OH^- + OH^{\cdot} \quad \text{(Reaction 1: Fenton Reactoin)}$$

Superoxide or other reducing agents in the cell reduce the Fe^{3+} back to Fe^{2+}:

$$O_2^{\cdot-} + Fe^{3+} \rightarrow O_2 + Fe^{2+} \qquad \text{(Reaction 2)}$$

Reaction 1 + Reaction 2 yield:

$$H_2O_2 + O_2^{\cdot-} \rightarrow OH^- + OH^{\cdot} + O_2 \quad \text{(Reaction 3: Haber} - \text{Weiss Reaction)}$$

This process is also shown in Figure 1-1. The accumulated hydroxyl radicals are highly reactive and can damage bacterial cells by reacting with lipids, proteins, and DNA strands in the cells [9]. Consequently, the free Fe^{2+} levels in bacterial cells are thought to be regulated at 5 ~ 10 μM in order to avoid the occurrence of the Haber-Weiss reaction while ensuring sufficiency for cell activity [28].

Bacterial Ferritin and Bacterioferritin are Regulators of Intracellular Iron Levels

Ferritin (Ftn) and Bacterioferritin (Bfr) are classical iron storage proteins that function as dynamic regulators of cytosolic iron levels. As shown in Figure 1-1, under iron sufficient

conditions, these proteins utilize O_2 and H_2O_2 as electron acceptors to oxidize the potentially toxic Fe^{2+}. Oxidized Fe^{3+} is compartmentalized into these iron storage proteins in the form of Fe^{3+} mineral, avoiding formation of Fe^{3+} precipitates in the cytosol; under iron depleted conditions, these proteins accept electrons to reduce stored Fe^{3+} to Fe^{2+} and release Fe^{2+} to the cytosol for cell activities [8]. Therefore, the functions of storing and releasing iron in iron storage proteins allow the intracellular free Fe^{2+} level to be maintained by a dynamic equilibrium between the stored Fe^{3+} mineral and free Fe^{2+}.

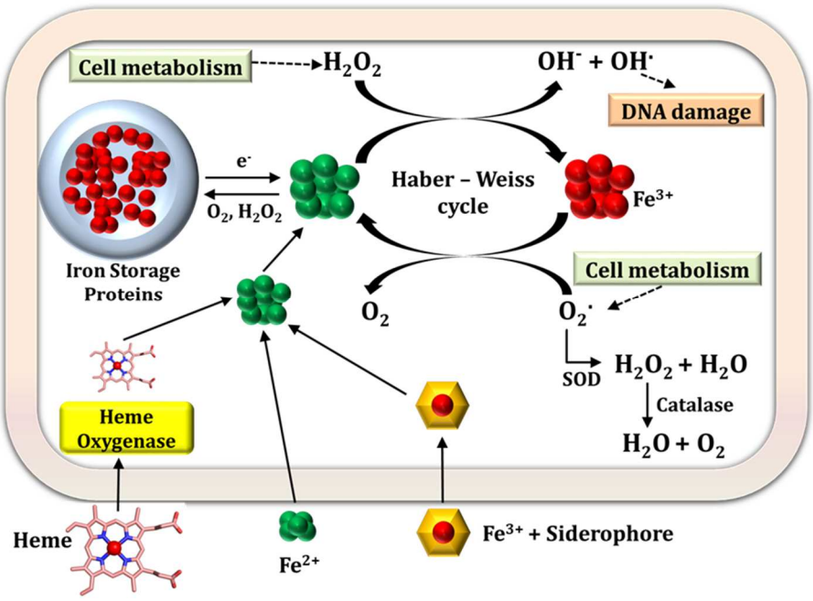

Figure 1-1 Schematic representation of bacterial iron homeostasis: Iron storage proteins likely regulate the intracellular iron levels to avoid the occurrence of the Haber-Weiss cycle (Figure adapted from Handbook of Porphyrin Science, Vol. 30, p136-179, 2014.).

Ftns are found in eukaryotes and bacteria whereas Bfrs are found only in bacteria [6, 8]. As shown in Figure 1-2 (A) and (B), Ftns and Bfrs share structural similarities. They are made from 24 subunits assembling into a nearly spherical, hollow shape with 4-3-2 symmetry. The

internal hollow cavity can hold up to 4,500 iron atoms. The 24-mer supramolecular assembly has an external diameter of ~12 nm and the internal diameter of the central cavity is about 7~ 8.5 nm. The subunit fold consists of four α-helices arranged in a 4- helix bundle with a short helix nearly perpendicular to the bundle [8, 29-31]. However, one significant structural difference between Ftns and Bfrs is that Bfrs harbor a heme group at the two-fold symmetric inter-subunit sites, where the heme-iron is coordinated by a methionine residue from each subunit (Figure 1-2 C) [8, 29, 31]. The two subunits binding heme are therefore defined as a subunit dimer. The heme molecules in Bfr are buried deep below the protein shell surface (~ 13 Å) so that the heme propionates extend into the Bfr interior cavity where the Fe^{3+} mineral is stored (Figure 1-2 D) [8, 29].

Ftns and Bfrs in bacteria play a significant role in the life cycle and virulence of pathogens. In 1999, Chen *et al* found that a Bfr-deficient mutant of *Nisseria gonorrhoeae* showed impaired growth under iron-limiting conditions. The mutant is also more sensitive to the killing by hydrogen peroxide [32]. In 2008, Expert *et al.* found that a mutation of the *bfr* gene in in the plant pathogen *Erwinia chrysanthemi* leads to impaired iron utilization and growth [33]. A recent study suggests the mutants of *Mycobacterium tuberculosis* suffer from iron–mediated oxidative stress toxicity and show reduced virulence in mice and guinea pig models of infection [34, 35]

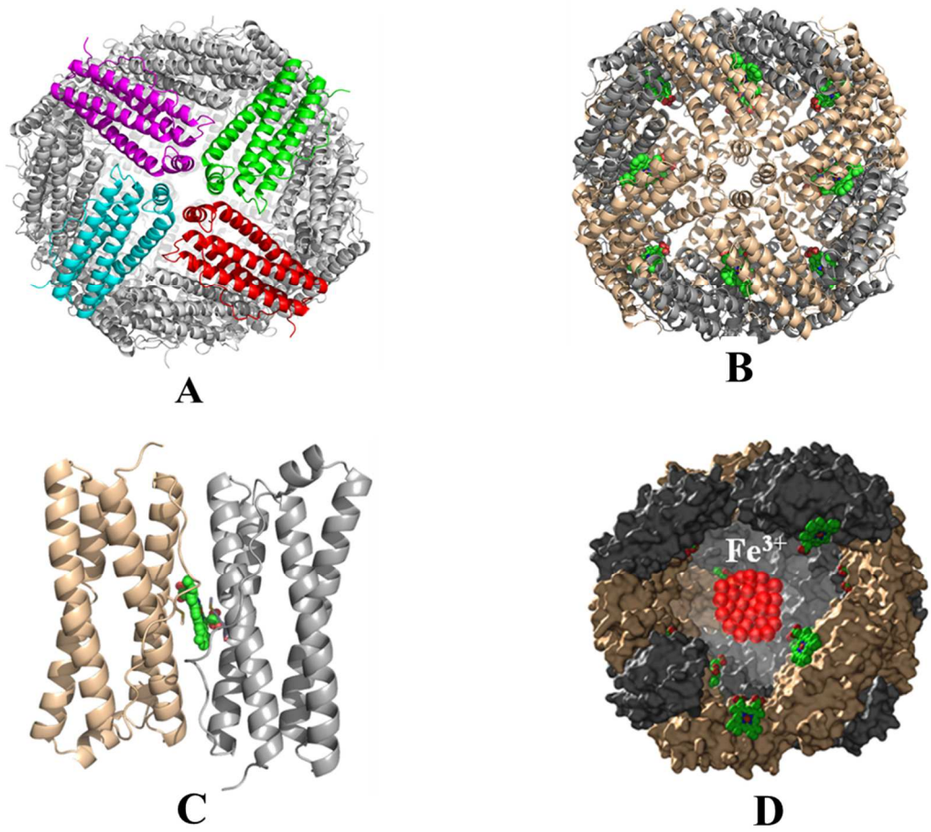

Figure 1-2 Structural organization of Bfr and Ftn (Figures adapted from Ref 8) (A) 24-mer assembly of Pa-FtnA (PDB:3R2K) (B) 24-mer assembly of Pa-BfrB (PDB:3IS7) (C) A subunit dimer of Pa-BfrB harboring a heme molecule (green). (D) Heme (green) is deeply buried below the Pa-BfrB protein shell surface

As mentioned above, the two key functions of Ftn and Bfr are thought to be in iron storage and iron mobilization. Significant advances have been made on understanding Fe^{2+} oxidation and uptake processes in Ftn and Bfr [8, 36, 37]. However, much less is known about their iron reduction and mobilization process[8]. For Ftn, the physiological partner or the protein-protein interactions that enable iron mobilized from the Ftn core remains unknown. For Bfr, genomic studies that have been carried out on multiple bacteria (especially *Pseudomonas*

aeruginosa), which suggested that iron mobilization from Bfr might need protein-protein interaction with its associated ferredoxin (Bfd) [8]. Also, previous *in vitro* studies on *Pseudomonas aeruginosa* Bfr (*Pa*-BfrB) in our group proved that *Pa*-Bfd is necessary in mobilizing iron from *Pa*-BfrB [38]. These indications and evidence are described below in more detail.

Genomic Studies Suggest that Iron Mobilization from Bfr Requires Protein-Protein Interactions

In 1989, an *E.coli* gene coding for a putative ferredoxin was found to be adjacent to the *bfr* gene [39]. Due to its proximity to the *bfr* gene and the ability of its protein product to bind a [2Fe-2S] cluster, which is typical of ferredoxins [40, 41], this gene was named *bfd* (bacterioferritin-associated ferredoxin). Also, a more extensive search of genomic data on multiple bacteria (Table 1-1) shows the *bfr-bfd* gene association is common to several important pathogens[42]. In addition, a study on the genetic response of *Pseudomonas aeruginosa* to iron starvation conditions shows that among 118 up-regulated genes by iron starvation, only two genes encode electron transfer proteins, *bfd* (200 –fold up-regulated) and *fpr (*codes for ferredoxin NADP reductase, 3-fold up-regulated). Meanwhile, the *bfr* gene is down regulated [43].

By mining the available genomic data, our group proposed that the BfrB and Bfd association is important for iron mobilization from bacterioferritin in bacteria: The up-regulation of *bfd* and *fpr* genes, concomitant with the down-regulation of *bfrB* in under iron starvation conditions, suggested that the roles of Bfd and Fpr may be as electron carriers to reduce the ferric iron stored in BfrB, therefore facilitating iron mobilization [8, 38, 42]. The

conserved proximity of the *bfr* and *bfd* genes also suggested that Bfr and Bfd might function similarly in a variety of bacteria.

Table 1-1 *bfr -bfd* gene proximity in several pathogens [42] (Adapted from *J. Am. Chem. Soc.* 2012, 134, 13470-13481)

Microorganism	**Locus ID**	
	Bfr	Bfd
Pseudomonas aeruginosa PAO1	PA3531	PA3530
Escherichia coli O157	Z4695	Z4696
Salmonella typhimurium	STM3443	STM3444
Klebsiella pneumoniae	KPN_03722	KPN_03723
Yersinia pestis	YPO0206	YPO0205
Aeromonas salmonicida	ASA_0467	ASA_0466
Vibrio cholerae E1	VC_0365	VC_0364
Shigella dysenteriae	SDY_3498	SDY_3499
Enterobacter sp. 638	Ent638_3754	Ent638_3755
Serratia sp.	Spro_4546	Spro_4547
Acinetobacter sp.	ACIAD3330	ACIAD3328

In Vitro Evidence of the Bfr-Bfd Interaction

(1) Ec Bfr-Bfd Interaction

The finding of the formation of *E. Coli* Bfr -Bfd complex was the first *in vitro* evidence of the Bfr-Bfd interaction [40]. Garg *et al* found that a Ni-IDA column pretreated with his-tagged Bfd binds both purified Bfr and overexpressed Bfr in a cell extract. The binding was demonstrated to be specific by either substituting the Bfr for bovine serum albumin and carbonic anhydrase, or substituting the Bfd for a C-terminal His-tagged rubredoxin-like protein from *A.* V*inelandii* [40]. These authors suggested that the BfrB interaction might be important in iron uptake by Bfr, or in the mobilization of iron stored in Bfr. The importance of Bfd in iron

mobilization from Bfr was postulated and demonstrated by our group using the proteins from P. aeruginosa [38](see below).

(2) Pa BfrB-Bfd Interaction

In 2009, Weeratunga *et al.* also demonstrated the Bfr and Bfd from *Pseudomonas aeruginosa (Pa* BfrB and *Pa* Bfd*)* form a complex. In an experiment, the *Pa* BfrB was mixed with *Pa* Bfd and the protein mixture was passed through a calibrated Superdex-200 column. The elution volumes of the peaks suggested there are about 12 Bfd molecules bound to 1 BfrB molecule [38].

Pa BfrB-Bfd Interaction Model

By mining the genomic information and the results from the *in vitro* studies above, our group proposed a model for *Pa*-BfrB iron mobilization (Figure 1-3). *Pa-Bfd* mediates electrons from *Pa*-FPR to *Pa*-BfrB to reduce the Fe^{3+} in the BfrB core to Fe^{2+} and the Fe^{2+} is subsequently released from the core.

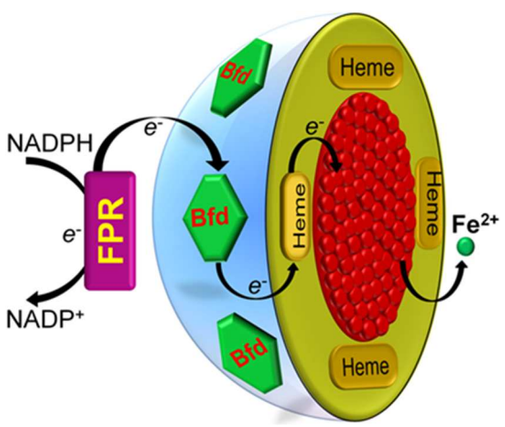

Figure 1-3 Model of electron transfer across the Pa-BfrB shell to reduce Fe^{3+} mineral and promote release of Fe^{2+} (Figure adapted from Ref 8)

To test this model, the *fpr, bfd, and bfrB* genes from *P. aeruginosa* were cloned and expressed in *E. coli*. The recombinant proteins were purified and characterized.

(1) *Pa*-BfrB

In common with the structure of other bacterioferritins mentioned above, *Pa*-BfrB is composed of 24 subunits. Each subunit is built of four nearly parallel α-helices with a short C'-terminal helix almost perpendicular to the four helices bundle (Figure 1-2A). One heme molecule is harbored at each subunit dimer, axially coordinated by a methionine (Met52) from each adjacent subunit (Figure 1-2C). The heme molecules are deeply buried below the protein shell surface with their propionates extending into the interior cavity where the Fe^{3+} mineral is stored (Figure 1-2D) [29].

There is a ferroxidase center (FC) located at the middle of each four helix bundle, which allows the Fe^{2+} to be captured and oxidized to Fe^{3+} and stored into the hollow cavity[8,29]. As shown in Figure 1-4A, the ferroxidase center in *Pa*-BfrB coordinates two iron ions with the residues E51 and E127 that function as bridging ligands and the residues H52, H130, E18 and E94 function as capping ligands [8, 29]. The mechanism of iron uptake in *Pa*-BfrB has been proposed (Figure 1-4B) [8, 29]. The Fe^{2+} is captured at the FC of each subunit to form a di-Fe(II) center. The di-Fe(II) center is oxidized to a μ-oxo/hydroxo di-Fe (III) moiety using O_2 and H_2O_2 as electron acceptors. The iron ions in the di-Fe (III) moiety are transported to the *Pa*-BfrB internal cavity and hence allow the empty FC to be able to capture Fe^{2+} and start a new cycle [8, 29].

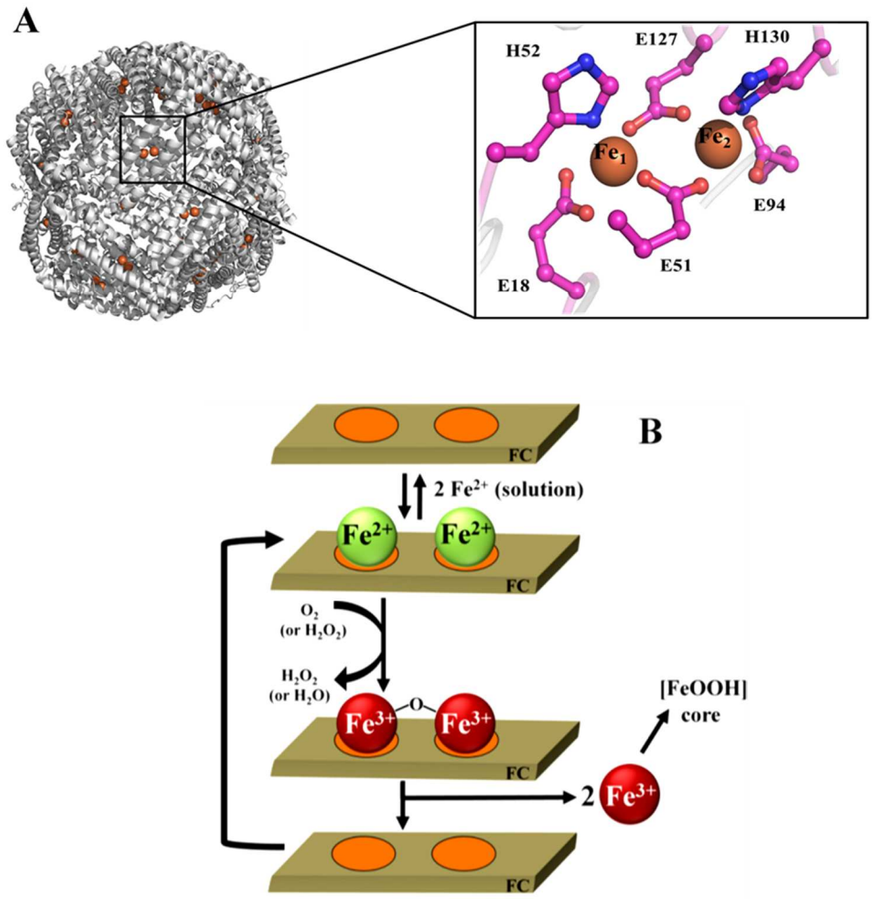

Figure 1-4 (A) Ferroxidase center of Pa-BfrB (Figure adapted from Ref 8). (B) Proposed iron uptake and oxidation mechanism in Pa-BfrB (Figure adapted from Ref 8)

(2) *Pa*-Bfd

Pa-Bfd is a 73 amino acid protein that harbors a [2Fe-2S] cluster. Its sequence has four conserved cysteines: C4, C6, C38 and C41. These four cysteines are thought to coordinate the [2Fe-2S] cluster, which is a typical electron carrier. Until my current work (see Chapter 2), the structure of Bfd remained unknown [44].

(3) *Pa*-FPR

Pa-Fpr is a nicotinamide adenine dinucleotide phosphate (NADPH)-dependent flavin-containing enzyme, which is also thought to transfer the electrons required by *Pa*-heme oxygenase for the oxidative breakdown of heme into biliverdin and free iron [44]

Pa-Bfd Facilitates the Mobilization of Core Iron from Pa-BfrB

To test the *Pa*-BfrB iron mobilization model mentioned above, *Pa*-BfrB containing 600 iron atoms in its interior cavity was mixed under anaerobic conditions with *Pa*-Bfd and *Pa*-Fpr in a cuvette containing excess 2'2-bipyridine (bipy) [38]. The reaction was initiated by adding excess NADPH. Mobilization of iron from *Pa*-BfrB was monitored by tracking the time-dependent formation of the $[Fe(bipy)_3]^{2+}$ complex, which absorbs at 523 nm. The percentage of iron release was obtained by normalizing the ΔA_{523} to the total absorbance change expected upon removal of all iron ions from *Pa*-BfrB. The black and red circles in Figure 1-5A indicate that only in the presence *Pa*-Bfd the iron mobilization can be facilitated [38]. Clearly, *Pa*-Bfd is necessary for the efficient and quantitative release of Fe^{2+}.

It is also noteworthy that during the *Pa*-Bfd-facilitated rapid release of iron, the heme Soret band from BfrB shifts from 418 nm (oxidized heme) to 425 nm (reduced heme), indicating full reduction of the heme in *Pa*-BfrB (Figure 1-5B black trace) [38]. In contrast, the Soret band remains unchanged in the absence of *Pa*-Bfd, indicating the heme remains oxidized (Figure 1-5B red trace). This concomitant reduction of heme only in the presence of *Pa*-Bfd agrees with the proposed model in the respect that *Pa*-BfrB heme accepts electrons from *Pa*-Bfd. However, more experimental support was needed in order to validate the conductive nature of heme in the iron mobilization process [38].

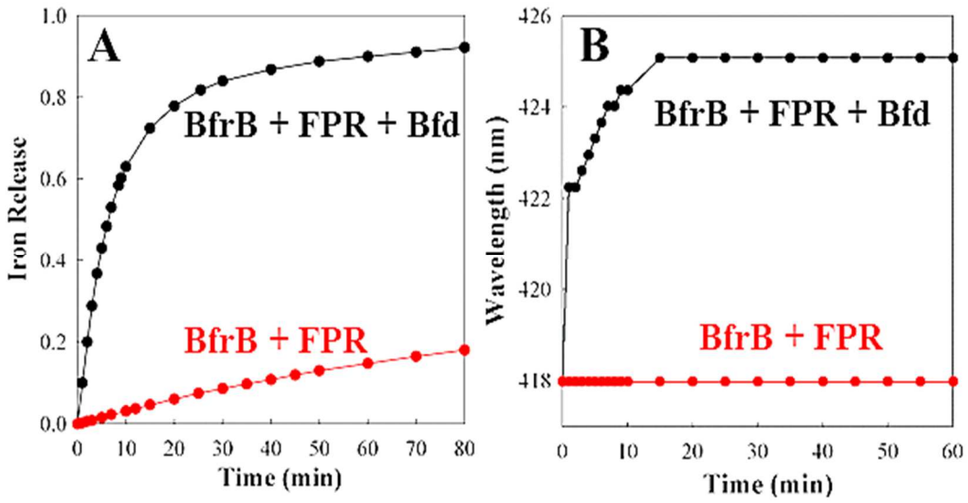

Figure 1-5 Binding of Pa-Bfd is necessary to promote Fe^{2+} mobilization from Pa-BfrB. (A) Normalized iron release from Pa-BfrB in the presence of Pa-Bfd (black) and without Pa-Bfd (red). (B) Time-dependent changes in the heme Soret band position upon the addition of NADPH in the presence of Pa-Bfd (black) and in the absence of Pa-Bfd (red).

Heme Mediates Electrons to the BfrB Ferric Core

The hypothesis, heme mediating electron transfer from the surface to the Fe^{3+} mineral, was further proved in a similar iron mobilization experiment [38]. Instead of adding extra NADPH, aliquots delivering 15% NADPH of the total electron equivalents required to reduce all the stored iron in BfrB were added. A rapid and quantative release of Fe^{2+} corresponding to the added electrons upon each addition of NADPH was observed (blue trace in Figure 1-6) [38]. It was also observed that the Soret band shifted rapidly from 418 nm toward 425 nm and gradually shifted back to 418 nm, indicating a buildup of reduced heme followed by the re-oxidation (red trace in Figure1-6) [38]. This reducing/re-oxidizing process of heme not only suggests that heme mediates electrons from *Pa*-Bfd to the *Pa*-BfrB core, but also indicates that the *Pa*-Bfd transfers electrons to heme faster than heme shuttles electrons to the core mineral.

As the addition of NADPH aliquots proceeded, the concentration of the accumulated reduced heme increased. This suggested that with more Fe^{2+} being released, the shrinking Fe^{3+} core has less demand of electron flux from the heme. Hence, if the electron flux from *Pa*-Bfd to the heme in BfrB remains similar after each addition of NADPH, but the electron flux from the heme to the iron core becomes less, there is a higher transient buildup of reduced heme [8, 38].

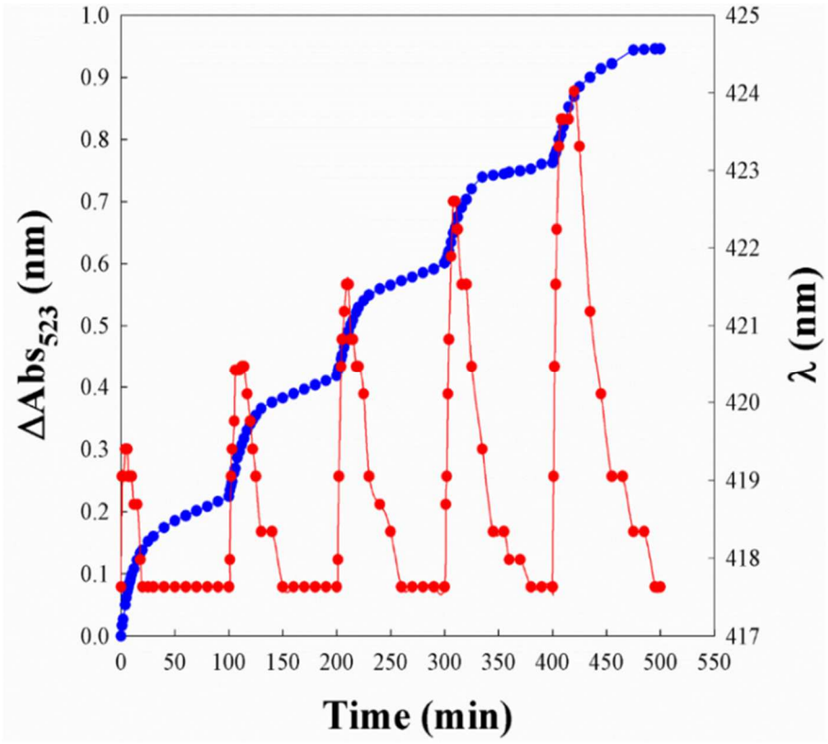

Figure 1-6 Pa-Bfd facilitates heme mediated electron transfer to the Pa-BfrB ferric core. Time-dependent wavelength shift of the heme Soret band (red) and time–dependent increases of A_{523} upon the addition of each aliquot of NADPH (blue) (Figure adapted form Ref 38)

The first indication that heme serves as an electron mediator in the iron mobilization process was obtained from stopped-flow studies with *Azotobacter vinelandii* Bfr (*Av*-Bfr) by Richards *et al.* [45]. In this study, *Av*-Bfr iron core was reduced with sodium dithionite and the

release of Fe^{2+} was monitored by measuring the formation of $[Fe(bipy)_3]^{2+}$. The oxidation state of heme was monitored using stopped flow experiments. The biphasic kinetics observed in the stopped-flow experiments suggested that heme is reduced first and then core iron is reduced by the electrons transferred from heme[45]. Also, a more recent study with *Ec*-Bfr shows that *Ec*-Bfr with 5 heme/24-mer protein has a higher iron release rate upon the addition of sodium dithionite than the *Ec*-Bfr with 1 heme/24-mer protein [46]. These phenomena are in agreement with the notion that heme mediates electron transfer from Bfd to the Bfr core mineral [46].

In summary, the results above indicate: (i) the heme in bacterioferritin mediates electron transfer to the iron core; (ii) the interaction of *Pa*-BfrB and *Pa*-Bfd is a prerequisite for making the heme in BfrB "conductive". Hence,the model proposed by our group for iron mobilization from BfrB (Figure 1-3) is partially supported by the above described results. Nevertheless, details pertaining the mechanism of the BfrB-Bfd interaction, as well as the electron transfer process, including the role of the Bfd [2Fe-2S] cluster, remain to be explored. These issues have been addressed by my work and the results will be presented throughout this dissertation.

Role of [2Fe-2S] Cluster in BfrB Iron Mobilization

Previously, Weeratunga *et al.* tried to probe the role of the [2Fe-2S] cluster during the BfrB iron mobilization process [38]. In the assay, the [2Fe-2S] cluster was removed from the Bfd *in situ* to make apo-Bfd, which was not separated from free Fe^{2+} and S^{2-}. This solution containing apo-Bfd and free Fe^{2+} and S^{2-} was used to investigate whether apo-Bfd can function in the mobilization of iron from BfrB. As shown in Figure 1-7, the apo-Bfd shows similar stimulatory effect as the holo-Bfd in facilitating mobilization of iron from BfrB. This phenomenon led the authors to propose that the [2Fe-2S] cluster was not important in this iron

mobilization process, and therefore the Bfd might not be participating in the electron transfer process as proposed in the model.

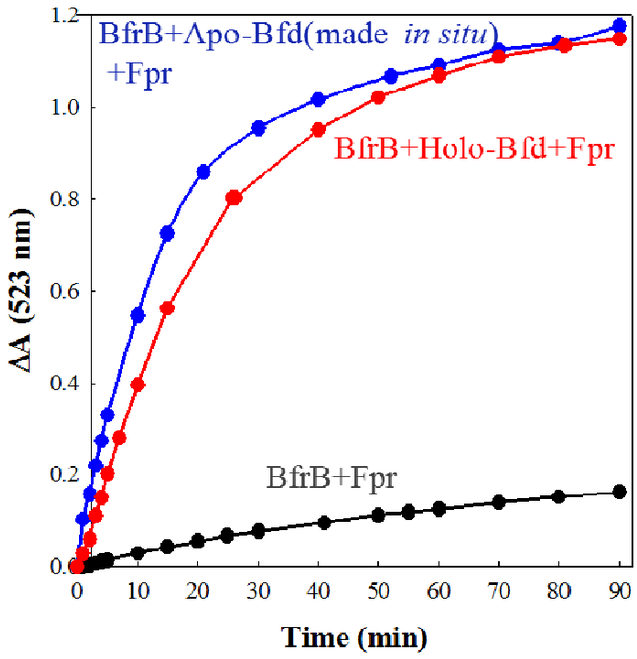

Figure 1-7. Apo-Bfd (made *in situ*) facilitates BfrB iron mobilization (blue) in a way similar as holo-Bfd (red). Without Bfd, the iron mobilization from BfrB is slow (black) (Figure adapted from Ref 38)

Consequently, an alternative model was proposed (Figure 1-8), where the apo-Bfd functions in facilitating electron transfer from FPR to BfrB by recruiting FPR to the BfrB surface. Clearly, this model had to be challenged rigorously by preparing and isolating apo-Bfd prior to reconstituting it with Pa-BfrB and Pa-FPR. In Chapter 2, I will describe how I carried out this work, which led to the unambiguous conclusion that the [2Fe-2S] cluster in Bfd is necessary to transfer electrons to the heme in BfrB [42],

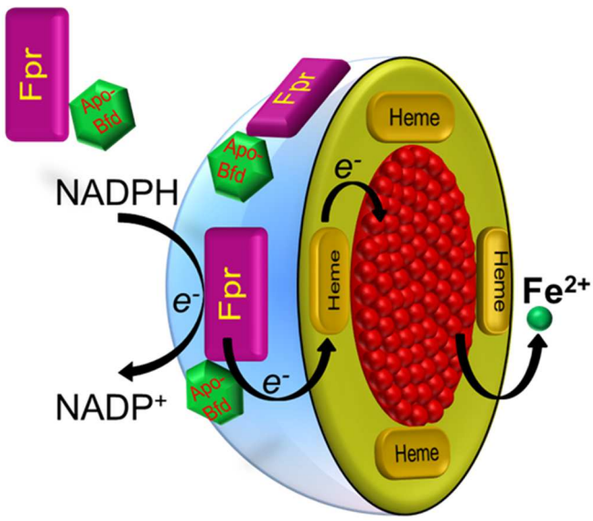

Figure 1-8. Proposed model for BfrB iron mobilization where the electron transfer of FPR to BfrB heme is facilitated by apo-Bfd recruiting the FPR to the BfrB surface.

Research Problem and Rationale

Bacterial iron homeostasis is essential for bacteria to survive, thus iron homeostasis provides a potential novel target for antibiotic development. To progress toward this goal, a molecular level understanding of how iron is regulated in bacterial cells is crucial. Protein-protein interactions play an important role in bacterial iron homeostasis. More specifically, the BfrB-Bfd interaction has been shown to facilitate iron mobilization from the BfrB in *Pseudomonas aeruginosa* [8, 38]. However, as mentioned earlier, the detailed mechanisms of the BfrB-Bfd interaction and the electron transfer pathway of iron mobilization were unknown. Consequently, our studies were focused on evaluating the two models of iron mobilization from BfrB to identify the most likely mechanism of iron mobilization from BfrB, characterizing the BfrB-Bfd interaction, and identifying the protein-protein interaction hotspot in solution. This fundamental work has been important to inform other activities in our lab, which are concerned with developing small modulators that interfere with the BfrB-Bfd interaction in order to disrupt the iron regulation in *Pseudomonas aeruginosa.* In the long-term, the significance of the BfrB-Bfd interaction and the potential of inhibitors to disrupt the interaction will be tested *in Pseudomonas aeruginosa* cells and *in vivo* models of infection.

More specifically, the first aim of my work was focused on understanding the functional role played by the [2Fe-2S] cluster in Bfd in iron mobilization from BfrB, because it determines which of the two models that had been previously proposed provides a more reasonable mechanism. As will be shown in Chapter 2, apo-Bfd was prepared and isolated, and the pure protein was biochemically characterized using UV-vis and CD spectroscopy. To elucidate the participation of the [2Fe-2S] cluster in iron mobilization from BfrB, apo-Bfd was used for mobilizing iron stored in BfrB. Upon confirming that the [2Fe-2S] cluster is required for

mobilizing iron stored in BfrB, we used biochemical assays to define the specific function of the [2Fe-2S] as an electron carrier to transfer electrons to heme in BfrB. These results, together with the x-ray crystal structure of the BfrB-Bfd complex, which shows that the [2Fe-2S] cluster is placed close to the heme in BfrB, showed that the [2Fe-2S] cluster in Bfd functions in the transfer of electrons to heme in BfrB. In addition, the Bfd fold was revealed for the first time in our X-ray crystal structure of the BfrB/Bfd complex. Details regarding these findings are presented in chapter 2. The solution of X-ray crystal structure of BfrB-Bfd complex provided us with insights into the interaction interface and allowed us to analyze the specific interactions among the residues at the interface. Further, to corroborate some of the findings from the X-ray crystallography, we studied the BfrB-Bfd interaction in solution using surface plasmon resonance (SPR) and isothermal titration calorimetry (ITC), as described in chapter 3. These studies provided thermodynamic and kinetic parameters of the interaction. In order to identify the contribution of the important interacting residues at the BfrB-Bfd interface suggested by the x-ray crystal structure of the BfrB-Bfd complex, we mutated these residues to Ala and studied their binding affinity and functional activity in solution. Results obtained from these studies were used in our lab to design and screen a fragment library, with the goal of discovering inhibitors of the BfrB-Bfd interaction. My familiarity with the BfrB-Bfd interaction allowed me to contribute to these studies by optimizing an assay directed at evaluating the efficiency of small molecules at slowing or inhibiting the mobilization of iron stored in BfrB.

References

1. Prevention, C.f.D.C.a.; Available from: http://www.cdc.gov/drugresistance/.
2. Janet Woodcock, M.D., *21st Century Cures: Examining Ways to Combat Antibiotic Resistance and Foster New Drug Development*. 2014.
3. Nikaido, H., *Multidrug resistance in bacteria.* Annu Rev Biochem, 2009. **78**: p. 119-46.
4. Infectious Diseases Society of, A., *The 10 x '20 Initiative: pursuing a global commitment to develop 10 new antibacterial drugs by 2020.* Clin Infect Dis, 2010. **50**(8): p. 1081-3.
5. Ramisse, F., et al., *Decreased virulence of a strain of Pseudomonas aeruginosa O12 overexpressing a chromosomal type 1 beta-lactamase could be due to reduced expression of cell-to-cell signaling dependent virulence factors.* FEMS Immunol Med Microbiol, 2000. **28**(3): p. 241-5.
6. Andrews, S.C., A.K. Robinson, and F. Rodriguez-Quinones, *Bacterial iron homeostasis.* FEMS Microbiol Rev, 2003. **27**(2-3): p. 215-37.
7. Theil, E.C. and D.J. Goss, *Living with iron (and oxygen): questions and answers about iron homeostasis.* Chem Rev, 2009. **109**(10): p. 4568-79.
8. Rivera, M., *Bacterioferritin: Structure Function and Protein–Protein Interactions*, in *Handbook of Porphyrin Science (Volume 30)*. p. 135-178.
9. Touati, D., *Iron and oxidative stress in bacteria.* Arch Biochem Biophys, 2000. **373**(1): p. 1-6.
10. Boukhalfa, H. and A.L. Crumbliss, *Chemical aspects of siderophore mediated iron transport.* Biometals, 2002. **15**(4): p. 325-39.

11. Hood, M.I. and E.P. Skaar, *Nutritional immunity: transition metals at the pathogen-host interface.* Nat Rev Microbiol, 2012. **10**(8): p. 525-37.

12. Bullen, J.J., et al., *Iron and infection: the heart of the matter.* FEMS Immunol Med Microbiol, 2005. **43**(3): p. 325-30.

13. Weinberg, E.D., *Iron availability and infection.* Biochim Biophys Acta, 2009. **1790**(7): p. 600-5.

14. Kim, E.J., W. Sabra, and A.P. Zeng, *Iron deficiency leads to inhibition of oxygen transfer and enhanced formation of virulence factors in cultures of Pseudomonas aeruginosa PAO1.* Microbiology, 2003. **149**(Pt 9): p. 2627-34.

15. Khan, A.G., et al., *High-affinity binding by the periplasmic iron-binding protein from Haemophilus influenzae is required for acquiring iron from transferrin.* Biochem J, 2007. **404**(2): p. 217-25.

16. Wandersman, C. and P. Delepelaire, *Bacterial iron sources: from siderophores to hemophores.* Annu Rev Microbiol, 2004. **58**: p. 611-47.

17. Wehmhoner, D., et al., *Inter- and intraclonal diversity of the Pseudomonas aeruginosa proteome manifests within the secretome.* J Bacteriol, 2003. **185**(19): p. 5807-14.

18. Wright, A.C., L.M. Simpson, and J.D. Oliver, *Role of iron in the pathogenesis of Vibrio vulnificus infections.* Infect Immun, 1981. **34**(2): p. 503-7.

19. Sazawal, S., et al., *Effects of routine prophylactic supplementation with iron and folic acid on admission to hospital and mortality in preschool children in a high malaria transmission setting: community-based, randomised, placebo-controlled trial.* Lancet, 2006. **367**(9505): p. 133-43.

20. Ballouche, M., P. Cornelis, and C. Baysse, *Iron metabolism: a promising target for antibacterial strategies.* Recent Pat Antiinfect Drug Discov, 2009. **4**(3): p. 190-205.

21. Frederick, R.E., J.A. Mayfield, and J.L. DuBois, *Iron trafficking as an antimicrobial target.* Biometals, 2009. **22**(4): p. 583-93.

22. Kaneko, Y., et al., *The transition metal gallium disrupts Pseudomonas aeruginosa iron metabolism and has antimicrobial and antibiofilm activity.* J Clin Invest, 2007. **117**(4): p. 877-88.

23. Neilands, J.B., *A brief history of iron metabolism.* Biol Met, 1991. **4**(1): p. 1-6.

24. Cornelis, P., S. Matthijs, and L. Van Oeffelen, *Iron uptake regulation in Pseudomonas aeruginosa.* Biometals, 2009. **22**(1): p. 15-22.

25. Wyckoff, E.E., M.L. Boulette, and S.M. Payne, *Genetics and environmental regulation of Shigella iron transport systems.* Biometals, 2009. **22**(1): p. 43-51.

26. Cornelissen, C.N. and P.F. Sparling, *Iron piracy: acquisition of transferrin-bound iron by bacterial pathogens.* Mol Microbiol, 1994. **14**(5): p. 843-50.

27. Vasil, M.L. and U.A. Ochsner, *The response of Pseudomonas aeruginosa to iron: genetics, biochemistry and virulence.* Mol Microbiol, 1999. **34**(3): p. 399-413.

28. Keyer, K. and J.A. Imlay, *Superoxide accelerates DNA damage by elevating free-iron levels.* Proc Natl Acad Sci U S A, 1996. **93**(24): p. 13635-40.

29. Weeratunga, S.K., et al., *Structural studies of bacterioferritin B from Pseudomonas aeruginosa suggest a gating mechanism for iron uptake via the ferroxidase center.* Biochemistry, 2010. **49**(6): p. 1160-75.

30. Crichton, R.R. and J.P. Declercq, *X-ray structures of ferritins and related proteins.* Biochim Biophys Acta, 2010. **1800**(8): p. 706-18.

31. Frolow, F., A.J. Kalb, and J. Yariv, *Structure of a unique twofold symmetric haem-binding site.* Nat Struct Biol, 1994. **1**(7): p. 453-60.

32. Chen, C.Y. and S.A. Morse, *Neisseria gonorrhoeae bacterioferritin: structural heterogeneity, involvement in iron storage and protection against oxidative stress.* Microbiology, 1999. **145 (Pt 10)**: p. 2967-75.

33. Expert, D., A. Boughammoura, and T. Franza, *Siderophore-controlled iron assimilation in the enterobacterium Erwinia chrysanthemi: evidence for the involvement of bacterioferritin and the Suf iron-sulfur cluster assembly machinery.* J Biol Chem, 2008. **283**(52): p. 36564-72.

34. Pandey, R. and G.M. Rodriguez, *A ferritin mutant of Mycobacterium tuberculosis is highly susceptible to killing by antibiotics and is unable to establish a chronic infection in mice.* Infect Immun, 2012. **80**(10): p. 3650-9.

35. Reddy, P.V., et al., *Iron storage proteins are essential for the survival and pathogenesis of Mycobacterium tuberculosis in THP-1 macrophages and the guinea pig model of infection.* J Bacteriol, 2012. **194**(3): p. 567-75.

36. Bradley, J.M., G.R. Moore, and N.E. Le Brun, *Mechanisms of iron mineralization in ferritins: one size does not fit all.* J Biol Inorg Chem, 2014. **19**(6): p. 775-85.

37. Honarmand Ebrahimi, K., P.L. Hagedoorn, and W.R. Hagen, *Unity in the biochemistry of the iron-storage proteins ferritin and bacterioferritin.* Chem Rev, 2015. **115**(1): p. 295-326.

38. Weeratunga, S.K., et al., *Binding of Pseudomonas aeruginosa apobacterioferritin-associated ferredoxin to bacterioferritin B promotes heme mediation of electron delivery and mobilization of core mineral iron.* Biochemistry, 2009. **48**(31): p. 7420-31.

39. Andrews, S.C., P.M. Harrison, and J.R. Guest, *Cloning, sequencing, and mapping of the bacterioferritin gene (bfr) of Escherichia coli K-12.* J Bacteriol, 1989. **171**(7): p. 3940-7.

40. Garg, R.P., et al., *A [2Fe-2S] protein encoded by an open reading frame upstream of the Escherichia coli bacterioferritin gene.* Biochemistry, 1996. **35**(20): p. 6297-301.

41. Quail, M.A., et al., *Spectroscopic and voltammetric characterisation of the bacterioferritin-associated ferredoxin of Escherichia coli.* Biochem Biophys Res Commun, 1996. **229**(2): p. 635-42.

42. Yao, H., et al., *The structure of the BfrB-Bfd complex reveals protein-protein interactions enabling iron release from bacterioferritin.* J Am Chem Soc, 2012. **134**(32): p. 13470-81.

43. Ochsner, U.A., et al., *GeneChip expression analysis of the iron starvation response in Pseudomonas aeruginosa: identification of novel pyoverdine biosynthesis genes.* Mol Microbiol, 2002. **45**(5): p. 1277-87.

44. Wang, A., et al., *Biochemical and structural characterization of Pseudomonas aeruginosa Bfd and FPR: ferredoxin NADP+ reductase and not ferredoxin is the redox partner of heme oxygenase under iron-starvation conditions.* Biochemistry, 2007. **46**(43): p. 12198-211.

45. Richards, T.D., K.R. Pitts, and G.D. Watt, *A kinetic study of iron release from Azotobacter vinelandii bacterial ferritin.* J Inorg Biochem, 1996. **61**(1): p. 1-13.

46. Yasmin, S., et al., *A new role for heme, facilitating release of iron from the bacterioferritin iron biomineral.* J Biol Chem, 2011. **286**(5): p. 3473-83.

CHAPTER II

Characterizing the Structure and Function of *Pa*-Bfd

Introduction

Iron sulfur clusters are ubiquitous and versatile prosthetic groups that sustain fundamental life activities in most of the life forms. A variety of types of iron sulfur clusters including [2Fe-2S], [3Fe-4S], [4Fe-4S], [8Fe-7S] and [8Fe-8S], are found in different proteins with various functions. Due to their versatile chemical/electronic features, these clusters participate in many processes crucial to life, including electron transfer, iron/sulfur storage, substrate binding/activation, gene expression and regulation and enzyme activity [1, 2].

Ferredoxins are small, soluble, mostly acidic iron sulfur proteins found universally in biological organisms [3]. They harbor iron sulfur clusters which possess a high negative redox potential. The iron sulfur clusters in ferredoxins mainly include [2Fe-2S], [3Fe-4S] and [4Fe-4S] clusters, which typically function as electron mediators participating in a variety of metabolic process [2-4] .

Among different types of iron sulfur clusters, the [2Fe-2S] cluster is the simplest structural-functional motif observed in ferredoxins. It consists of two iron ions bridged by two sulfide ions. In ferredoxins, the iron in the [2Fe-2S] cluster is coordinated by four thiolate sulfur centers from four cysteinyl residues. The iron centers are tetrahedral (Figure 2-1). Sequence alignment of the [2Fe-2S] ferredoxins (Figure 2-2) shows that there are four conserved cysteines arranged in a conserved fold (C-X_5-C-X_2-C-X_{37}-C), which bind the [2Fe-2S] cluster [4].

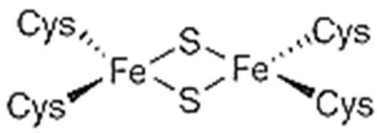

[2Fe-2S]

Figure 2-1 [2Fe-2S] cluster coordinated by four cysteines.

```
Spirulina platensis           ATYKVTLINE-AEGINETIDCDDDTYILDAA--EEAGLDLPYSCRA-GACSTCAGTITS
Anabaena 7120 vegetative      ATFKVTLINE-AEGTKHEIEVPDDEYILDAA--EEQGYDLPFSCRA-GACSTCAGKLVS
Anabaena 7120 heterocyst      ASYQVRLINK-KQDIDTTIEIDEETTILDGA--EENGIELPFSCHS-GSCSSCVGKVVE
Human mitochondrial        SSSEDKITVHIFINRDGETLTTKGKVGDSLLDVVVENNLDIDGFGACEGTLACSTCHLIFED
Bovine adrenal             SSSEDKITVHIFINRDGETLTTKGKIGDSLLDVVVQNNLDIDGFGACEGTLACSTCHLIFEQ
Putidaredoxin                    SKVVYVSHDG-TRRELDVADGVSLMQAAVSNGIYDIVGDCGGSASCATCHVYVNE

Spirulina platensis             GTIDQSD------QSFLD--DDQIEAGYVLTCVAYPTSDCTIKTHQEEGLY
Anabaena 7120 vegetative        GTVDQSD------QSFLD--DDQIEAGYVLTCVAYPTSDVVIQTHKEEDLY
Anabaena 7120 heterocyst        GEVDQSD------QIFLD--DEQMGKGFALLCVTYPRSNCTIKTHQEPYLA
Human mitochondrial             HIYEKLDAITDEENDMLD-LAYGLTDRSRLGCQICLTKSMDNMTVRVPETVADARQSIDVGKTS
Bovine adrenal                  HIFEKLEAITDEENDMLD-LAYGLTDRSRLGCQICLTKAMDNMTVRVPDAVSDARESIDMGMNSSKIE
Putidaredoxin                   AFTDKVPAANEREIGMLECVTAELKPNSRLCCQIIMTPELDGIVVDVPDRQW
```

Figure 2-2 Sequence alignment of different types of ferredoxins (Adapted from *J Bioenerg Biomembr*, 1994. 26(1): p. 67-88).

The [2Fe-2S] cluster functions as a one electron oxidation/reduction site in [2Fe-2S] ferredoxins: in the oxidized state, both iron ions adopt the Fe^{3+} state, while in the reduced state only one of the iron ions is reduced to Fe^{2+} [4]. The electron transfer function of the [2Fe-2S] ferredoxins takes place in a variety of life activities. For example, the "plant type" ferredoxins (*Spirulina platensis* ferredoxins and *Anabaena 7120* vegetative ferredoxins) transfer electrons from photosystem I to ferredoxin-$NADP^+$ reductase (FNR). *Anabaena 7120* Heterocyst ferredoxins (also a "plant type" ferredoxin) transfer electrons to the iron-protein of nitrogenase and hence play a role in nitrogen fixation. "Vertebrate type" ferredoxins (human placental and

bovine adrenal) transfer electrons from NADPH-dependent ferredoxin reductase to the cytochrome P450 enzyme. The ferredoxin from *Pseudomonas putida* (a "bacterial type" ferredoxin) specifically reduces the cytochrome $P450_{cam}$ isolated from the same species [4].

UV-vis spectroscopy is the simplest way to identify the existence of an oxidized [2Fe-2S] cluster. As shown in Figure 2-3, the oxidized [2Fe-2S] cluster in typical ferredoxins causes bands ranging from 300 to ~ 500 nm [5]. However, the reduction of the [2Fe-2S] cluster causes disappearance of these characteristic bands.

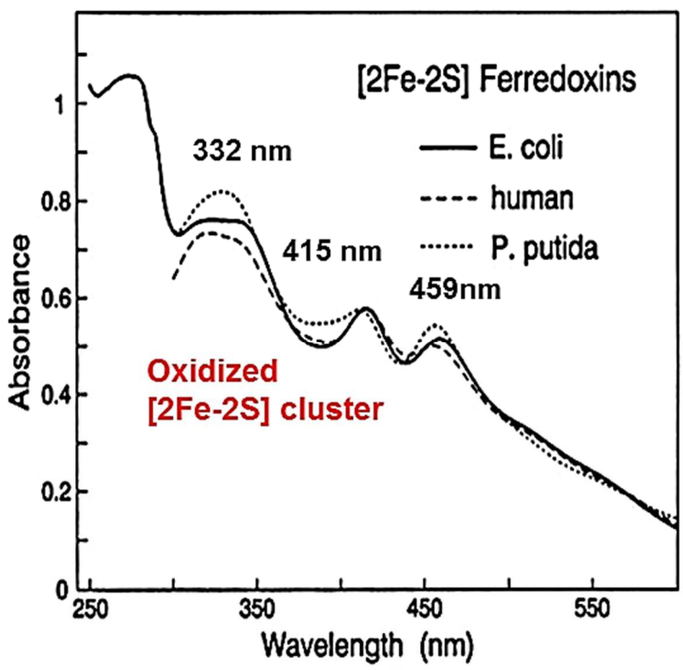

Figure 2-3 Example UV-vis spectra of [2Fe-2S] cluster ferredoxins ((Adapted from *J Biol Chem*, 1992. 267(16): p. 11120-5).

Besides ferredoxins, the [2Fe-2S] cluster is also observed in nitrogenase, the redox-sensitive transcriptional activator SoxR, the DNA-binding transcriptional regulator IscR, etc [4].

Bacterioferritin associated ferredoxin (Bfd) is a small protein (50~80 residues) whose gene is adjacent to the *bfr* gene. Similar to canonical [2Fe-2S] ferredoxins, Bfd also binds a [2Fe-2S] cluster, which is thought to be coordinated by four conserved cysteines [6]. The UV-vis spectrum of Pa-Bfd is shown in Figure 2-4.

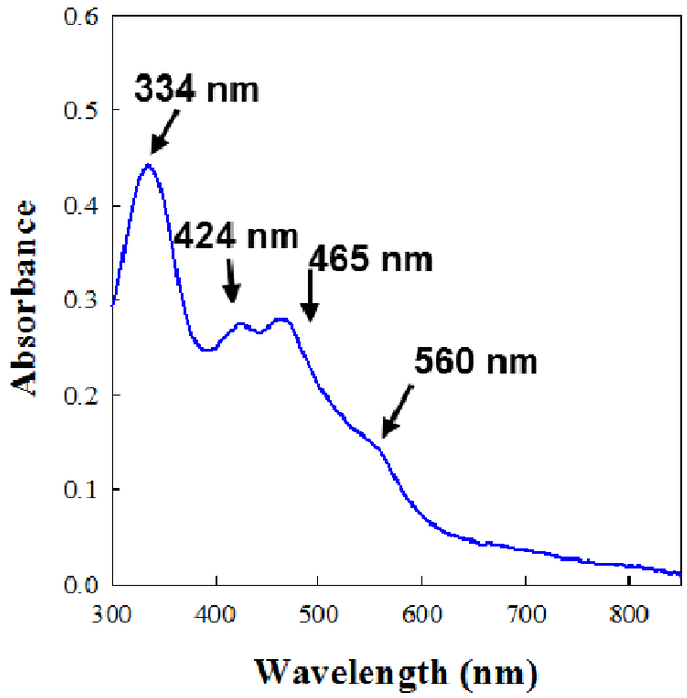

Figure 2-4 UV-vis spectrum of isolated Pa- Bfd with oxidized [2Fe-2S] cluster shows four characteristic peaks at 334 nm, 424 nm, 465 nm and 560 nm

Alignment of Bfd sequences from different bacterial species shows the four conserved cysteines arranged in a C-X-C-X_{31-32}-C-X_2-C fold (Figure 2-5), which is different from the conserved cysteine arrangement in canonical [2Fe-2S] ferredoxins [7]. In addition, Bfds are generally 50 residues shorter than canonical ferredoxins. The unique arrangement of Cys residues in the sequences, together with the shorter length of Bfds, suggest that Bfds do not belong the canonical ferredoxin family. In addition, the EPR and vibrational features of Pa-Bfd

are more similar to the features of NifU, which is a multi-domain protein for assembling metallo clusters in nitrogenase [6]. These observations, together with the above-described phenomenon that apo-Bfd made in *in situ* facilitated iron mobilization from Pa-BfrB (described in Chapter 1), it was proposed that Pa-Bfd might function as a scaffold for [2Fe-2S] cluster assembly, rather than as an electron carrier. However, more experimental data is needed to support this proposal.

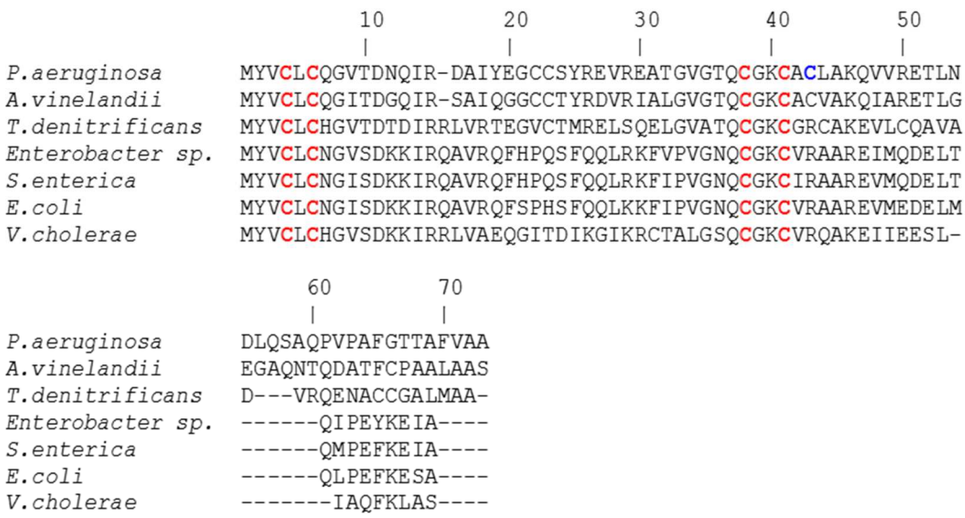

Figure 2-5 Alignment of Bfd sequence in different bacteria shows that there are four conserved cysteines (red) arranged in C-X-C-X_{31-32}-C-X_2-C fold (Figure adapted from Ref 7)

As discussed in Chapter 1, one of the key factors for understanding the BfrB-Bfd interaction mechanism is to determine the function of the [2Fe-2S] cluster during the Bfd-facilitated iron mobilization process. Therefore, in the experiments described in this chapter, we used biochemical assays to clearly define the role of the [2Fe-2S] cluster in iron mobilization from BfrB. In addition, we describe the structure of the BfrB-Bfd complex, which revealed detailed information of the BfrB-Bfd interface and thus provides us with useful information in establishing the BfrB-Bfd interaction mechanism.

Experimental Procedures

Pa-BfrB and the C43S mutant of Pa-Bfd were prepared and purified as reported previously [7].Since the same spectroscopic and functional properties were observed with C43S mutant compared to wild type, and the C43S mutant is more stable to purification storage and manipulation [7]. In this chapter, the C43S mutant will be referred to as Pa-Bfd.

Preparation of Apo-Bfd

A 0.54 mM solution of Pa-Bfd in 50 mM potassium phosphate (pH 7.0), 150 mM NaCl, and 5 mM DTT was diluted 8 times in buffer 1, consisting of sodium acetate buffer (150 mM, pH 5.5) 8 M urea, 150 mM NaCl, 5 mM tris(2- carboxyethyl)phosphine (TCEP), and 3 mM N,N′ -di-(2- hydroxybenzyl)ethylenediamine-N,N′ -diacetic acid (HBED) [8]. The resultant solution was stirred continuously at room temperature for 70 min. Iron chelated by HBED was removed by dialysis against buffer 1 at room temperature. HBED was then removed by dialysis against buffer 1 without the chelator, and the apo-protein was then dialyzed against buffer 2 (200 mM potassium phosphate, 8 M urea, 5 mM TCEP, pH 7.0) at room temperature. Refolding of apo-Bfd was carried out in two steps by dialyzing the protein against buffer 2 containing 4 M urea at 4 °C and then against buffer 2 without urea at 4 °C [8]

BfrB iron release study with apo-Bfd

The BfrB iron mobilization experiment was carried out in the presence of the isolated apo-Bfd. A previously described method was used with slight modifications [7]. In an anaerobic chamber, the isolated apo-Bfd (10 μM), Fpr (10 μM), BfrB (0.25 μM) were mixed in a cuvette containing 3 mM 2’2 –bipyridyl. The reaction was initiated by addition of 1.5 mM NADPH. Mobilization of iron from Pa-BfrB was monitored by tracking the time-dependent

formation of the $[Fe(bipy)_3]^{2+}$ complex, which absorbs at 523 nm [8]. The iron release percent was obtained by normalizing the ΔA_{523} to the total absorbance change expected upon removal of all iron ions from Pa-BfrB. The experiment was repeated by adding $(NH_4)_2Fe(SO_4)_2$ (20 μM) and Na_2S (20 μM) with the apo-Bfd to the system. Also, the experiment was repeated with holo-Bfd as a control [8].

Pa-Bfd transfers electrons to Pa-BfrB

A 30 μM solution of Pa-Bfd in 20 mM phosphate buffer pH 7.6 was placed in a cuvette. The Pa-Bfd solution was treated with 0.8 equiv of sodium dithionite and the reduction process was monitored by UV-vis spectrum. The spectrum was monitored (~15min) until no further changes took place. A small volume of a solution containing Pa-BfrB reconstituted with 590 Fe atoms/BfrB and a small volume of EDTA solution were added to produce a final Pa-BfrB concentration of 0.08 μM and final EDTA concentration of 0.1 mM. The EDTA was added to prevent precipitation of ferrous phosphate, which also causes protein precipitation and drift of the spectral baseline [8].

To monitor the iron release process during the reaction above, a similar experiment was carried out. However, instead of adding EDTA, 3 mM bipy was added prior to the addition of BfrB. The time dependent change in intensity at 523 nm was monitored [8].

Removal of phosphate from Pa- Bfd

A 780 μM solution of Pa-Bfd stock in 50 mM potassium phosphate, 150 mM NaCl, 5 mM Dithiothreitol (DTT), pH 7.0 was diluted up to 40 times into 150 mM Tris-Base, 250 mM NaCl, 3 mM TCEP (tris(2-carboxyethyl)phosphine). The dilution was made in a cuvette and the solution was monitored by UV-vis spectroscopy up to 4 hrs.

Removal of phosphate from Pa- Bfd in presence of Zn^{2+}

A 780 μM solution of Pa-Bfd stock in 50 mM potassium phosphate, 150 mM NaCl, 5 mM Dithiothreitol (DTT), pH 7.0 was diluted up to 40 times into 150 mM Tris-Base, 150 mM NaCl, 5 mM TCEP, 125 μM ZnSO4.7H2O), pH 7.8. The dilution was made in a cuvette and the solution was monitored by UV-vis spectroscopy for 30min. The resulted protein was dialyzed against 150 mM Tris-Base, 150 mM NaCl, 5 mM TCEP, 125 μM (ZnSO4.7H2O), pH 7.8 for 3hrs. The final product was measured for iron content using a previously described method [9] and the ratio of iron/protein was calculated.

Characterization of Pa-Bfd, Pa apo-Bfd in phosphate buffer and in Tris-Base buffer by Circular Dichroism Spectroscopy

Pa-Bfd was dissolved in 50 mM potassium phosphate pH 7.0, 4 mM NaCl, and 0.13 mM DTT. To obtain the CD spectra of Pa apo-Bfd in phosphate buffer and in Tris-Base buffer respectively, the following steps are used. As mentioned above, the Bfd was unfolded in 8 M urea in order to make apo-Bfd. The apo-Bfd was divided into two aliquots and was refolded by two separate dialysis against: (1) 200 mM potassium phosphate, 3 mM TCEP, pH 7.0 and (2) 200 mM Tris-Base, 200 mM NaCl, 3 mM TCEP, pH 7.0. To obtain good CD signal, the concentration of the TCEP was reduced to 1 mM and the concentration of the NaCl was reduced to 120 mM during the last step of dialysis, right before taking the CD spectra. The CD spectra of the proteins in phosphate buffer and in Tris-Base buffer were recorded on a Chirascan^{TM} Plus CD spectrometer (Applied Photophysics). Both samples were recorded at 4 °C and were scanned from 180 to 260 nm using a 0.05 cm bandwidth cuvette. The mean residue ellipticity θ (deg cm^2 dmol^{-1} residue^{-1}) was obtained using the Pro Data Software Suite.

Crystallization of Pa BfrB-Bfd complex

A 40 μM solution of Pa-BfrB in 100 mM potassium phosphate, 1mM TCEP, pH 7.6 and a 480 μM solution of Pa-Bfd in 50 mM potassium phosphate, 150 mM NaCl, 5 mM dithiothreitol (DTT), pH 7.0 were mixed in a volume ratio of 1:1. Therefore, the final molar ratio of Bfd to BfrB is 12:1 [8].

1 μL of the protein solution and 1 μL of the crystallization solution were equilibrated against 100 μL of the latter in sitting drop vapor diffusion plates at 18 °C. Crystals were grown under aerobic conditions. Small prismatic crystals were obtained in 1-2 days with condition G8 (0.8M Na/K hydrogen phosphate, pH7.5) of the Proplex HT screen (Molecular Dimensions) [8]

Truncation of Pa-Bfd (M1-L56)

The Pa-Bfd was truncated after L56. Codons coding for residue Q57 (CAG) were mutated to a stop codon (TAA). The sequences of the primers were designed for the truncated Bfd:

Forward: 5' GAAACCCTGAACGACCTGTAAAGCGCGCAGCCGGTGCCGG 3'

Reverse: 5' CCGGCACCGGCTGCGCGCTTTACAGGTCGTTCAGGGTTTC 3'

The GC content is 65% and the melting temperature is 83.3 °C.

The mutation was introduced with the aid of the Quick Change mutagenesis kit (Stratagene, La Jolla, CA) using manufacturer instructions. The pET11a plasmid harboring the gene coding for the full length Pa- Bfd was used as the template DNA. The resultant gene was transformed to *E. coli* XL1 Blue supercompetent cells for DNA amplification. Once the truncation was confirmed by sequencing (ACGT Inc. Wheeling, IL), plasmids carrying the truncated gene was transformed into *E. coli* Arctic express (DE3) RIL competent cells (Agilent Technologies, Santa Clara, CA).

The truncated Bfd was expressed and purified with the same method used for the full length Pa- Bfd. The purity of the protein was determined by SDS-PAGE. The truncation was confirmed by mass spectrometry.

Crystallization of truncated-Bfd

Purified Bfd (M1-L56) was concentrated to ~1.2 mM. During the concentration process, needle-shaped crystals were observed forming. The crystallized material was removed by spinning down the protein solution. The supernatant was screened for crystallization Compact Jr. (Emerald Biosystems) sitting drop vapor diffusion plates at 20 ^{o}C using 0.5 µL of protein in buffer containing 50 mM potassium phosphate, 150 mM NaCl, 5 mM DTT, pH 7.0 and 0.5 µL of crystallization solution equilibrated against 100 µL of the latter. The supernatant containing small crystals was used as seeds for the subsequent crystallization trials. Needle-shaped crystals were observed from various conditions within an hour and grew to their maximum size in approximately 24 hours. Crystals obtained from Crystal Screen HT (Hampton Research) condition A1 (30% (v/v) 2-methyl-2, 4-pentanediol, 100 mM sodium acetate pH 4.6, 20 mM $CaCl_2$) were used for X-ray data collection. Crystals were transferred to a fresh drop of crystallization solution and was flash frozen in liquid nitrogen for data collection. Data were collected at the Advanced Photon Source beamline 17-ID using a Dectris Pilatus 6M pixel array detector [8].

Results

Characterizations of apo-Bfd

Isolated apo-Bfd was characterized by mass spectrometry, UV-vis and CD spectroscopy. The mass spectrum of apo-Bfd shows that the molecular weight of the apo-protein is similar to the holo-Bfd (7807 ± 1 Da) (Figure 2-6).

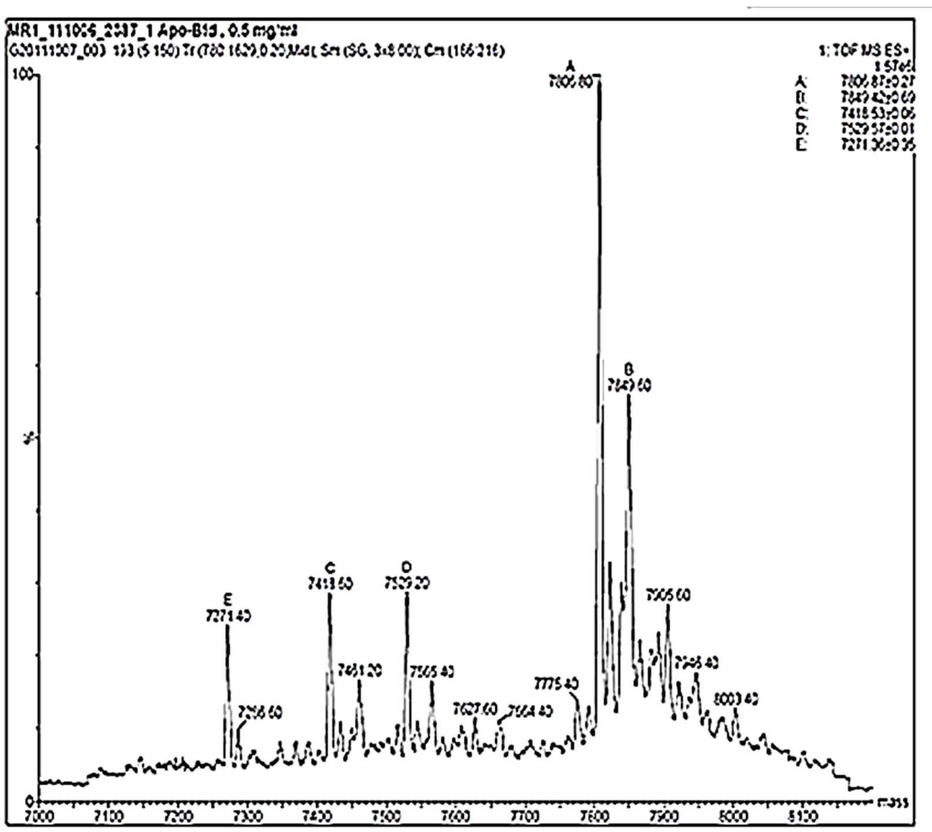

Figure 2-6 Mass spectrum of isolated apo-Bfd.

The UV-vis spectrum of apo-Bfd in Figure 2-7A shows only a 280 nm band (red trace). Clearly, the disappearance of the characteristic peaks of the [2Fe-2S] cluster (300 nm ~ 600 nm) suggest successful removal of the [2Fe-2S] cluster. The far UV-CD spectra of holo-Bfd (blue)

and apo-Bfd (black) are shown in Figure 2-7B. The holo-Bfd has double minima at 222 and 208 nm ($[\theta]_{222}/[\theta]_{208} = R \sim 1.1$), representing typical α-helical structure. Compared to the holo-Bfd, the apo-Bfd shows decrease in intensity at the 222 nm and blue shift of the high-energy band from 208 nm toward 203 nm, resulting in a ratio of $[\theta]_{222}/[\theta]_{203} = R \sim 0.45$.

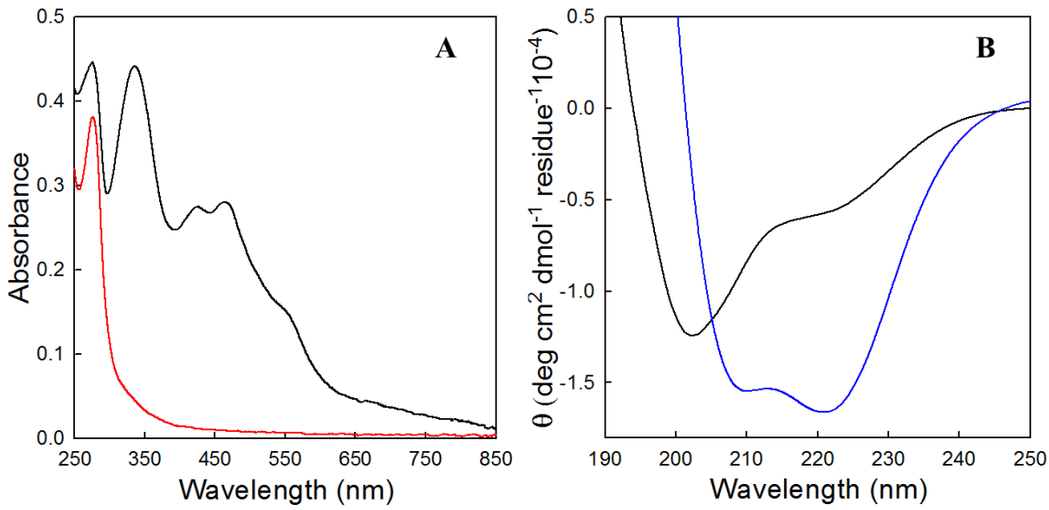

Figure 2-7 (A) UV-vis spectra of Pa-Bfd in 50 mM potassium phosphate pH 7.0 (black) and apo-Bfd in 200 mM potassium phosphate pH 7.0 and 5 mM TCEP (red) [8]. (B) Far UV CD spectra of Pa-Bfd in 50 mM potassium phosphate pH 7.0, 4 mM NaCl, and 0.13 mM DTT (blue) and Pa apo-Bfd in 200 mM Tris, pH 7.0, 120 mM NaCl and 1 mM TCEP (black) [8].

The CD spectral changes caused upon removal of the [2Fe-2S] cluster indicate partial loss of the α-helical structure [8], which suggests that the [2Fe-2S] cluster is crucial for stabilizing the Bfd fold.

The role of the [2Fe-2S] cluster in the Mobilization of Iron from BfrB

(1) Apo-Bfd in BfrB iron mobilization

As mentioned in Chapter 1, determining the function of the [2Fe-2S] cluster in the BfrB-Bfd iron mobilization is crucial for exploring the detailed mechanism of this process[7, 8].Therefore, we used our isolated apo-Bfd in the assay for measuring iron mobilization from Pa-BfrB. Unlike in the presence of holo-Bfd, no efficient iron release was observed in the presence of apo-Bfd (Figure 2-8 blue trace)**.** However, significant acceleration of iron release resulted when apo-Bfd was added into the system with Fe^{2+} and S^{2-} (Figure 2-8 black trace). In contrast, when apo-Bfd was absent, the rate of iron mobilization was sluggish, even with the presence of the Fe^{2+} and S^{2-}. (Figure 2-8 red trace). These observations not only demonstrate that the [2Fe-2S] cluster is essential for mobilizing iron from Pa-BfrB, but also suggest that the Fe^{2+} and S^{2-} might be able to readily assemble into a [2Fe-2S] cluster on apo-Bfd when BfrB is present. In the absence of BfrB, however, assembly of a [2Fe-2S] cluster in Bfd is slow and less efficient [6]. These observations also explain the phenomenon observed in the previous study [7] where apo-Bfd made *in situ,* not being separated from the Fe^{2+} and S^{2-}, was able to assemble an iron sulfur cluster, and therefore facilitated iron release from Pa-BfrB [7].

My experiments, therefore, prove that the [2Fe-2S] cluster in Bfd is required for mobilizing iron stored in BfrB. Consequently, this finding provides crucial information to evaluate the two models of iron mobilization discussed in Chapter 1. Model 2 can be rejected based on the result that the Pa apo-Bfd does not promote iron release from Pa-BfrB. In contrast, model 1, which indicates that holo Pa-Bfd mediates electron transfer from FPR to heme is supported by our experiments, and we suggest that the [2Fe-2S] cluster in Bfd functions as an electron mediator, to transfer electrons to the BfrB heme.

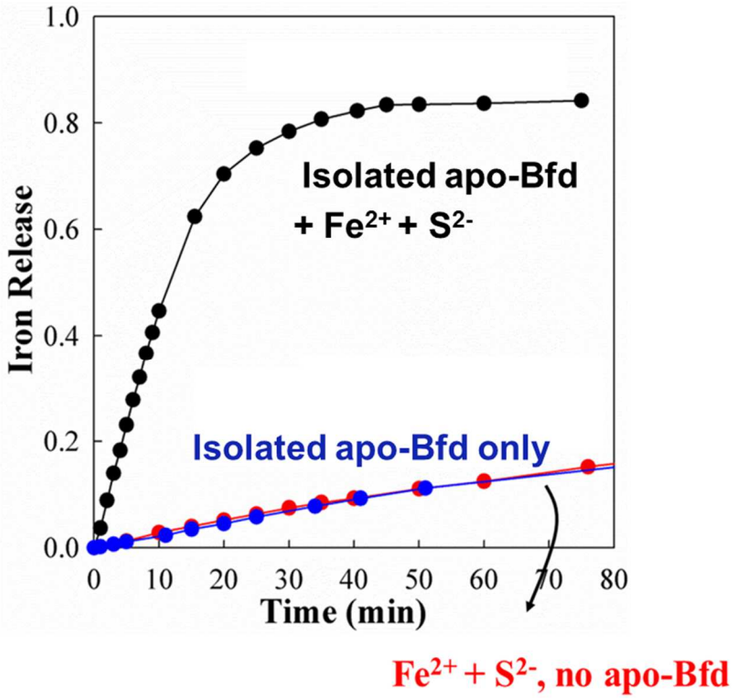

Figure 2-8 Time dependent increase of Pa-BfrB iron release percentage containing: (blue) Pa-BfrB 0.25 μM), Pa-FPR (10 μM), and apo Pa-Bfd (10 μM). (black) Pa-BfrB (0.25 μM), Pa-FPR (10 μM), apo-Pa-Bfd (10 μM), $(NH4)_2Fe(SO_4)_2$ (20 μM), and Na_2S (20 μM); (red) Pa-BfrB (0.25 μM), Pa-FPR (10 μM), $(NH4)_2Fe(SO_4)_2$ (20 μM), and Na_2S (20 μM)

(2) The [2Fe-2S] cluster in Bfd transfers electrons to the heme in BfrB

In order to test our hypotheses that the [2Fe-2S] cluster in Bfd mediates electrons to the heme in BfrB [8], a solution of holo-Pa-Bfd (30 μM) in a cuvette was reduced under anaerobic conditions by addition of 0.8 equiv of sodium dithionite [8]. The reduction was confirmed by a significant decrease in intensity of the UV-vis bands characteristic of an oxidized [2Fe-2S] cluster (Figure2-9A). The solution of reduced Bfd was then mixed with BfrB that had been reconstituted with ~590 iron, and the reaction proceeded with the spectral changes shown in Figure 2-9B. The red trace corresponds to Bfd with the reduced [2Fe-2S] cluster. After the

addition of Pa-BfrB, the Soret band in BfrB shifts from 418 nm to 424 nm within 20 s (blue trace), indicating reduction of the heme. Simultaneously, the characteristic peaks of the oxidized [2Fe-2S] cluster at 334 nm and 465 nm start to reemerge, indicating that the [2Fe-2S] cluster is being reoxidized. The shift in the Soret band (reduction of heme) which occurs concomitantly with the reemerging of the peaks characteristic of an oxidized [2Fe-2S] cluster indicate that the [2Fe-2S] cluster is passing electrons to the heme in Pa-BfrB. The magenta, green and black traces are the spectra recorded at 1 min, 3 min and 5 min of the reaction, respectively. The reoxidized [2Fe-2S] cluster peaks reach the maximum intensity at ~5min., suggesting the [2Fe-2S] cluster has completed the process of passing out electrons. Meanwhile, the Soret band shifts from 424 nm back to 418 nm, indicating the heme is being reoxidized. The reoxidation of the heme indicates that the heme molecules pass out the electrons to the Fe^{3+} mineral in the BfrB central cavity. The reoxidation of the [2Fe-2S] is visualized more clearly in Figure 2-9C, in which a difference spectrum was obtained by subtracting a spectrum of Pa-BfrB at the same concentration as used in the experiment from the black trace (5 min) in Figure 2-9B. The full recovery of the [2Fe-2S] cluster peaks indicates that the reduced Bfd conducted a complete electron transfer to the heme. In addition, the iron being released during this process was monitored in a similar experiment, which was conducted in the presence of excess bipy. The time-dependent Fe^{2+} release was detected by the formation of $[Fe(bipy)_3]^{2+}$ at 523 nm. As expected, a fast iron release was observed and the maximum $[Fe(bipy)_3]^{2+}$ level was 24 μM , which is well correlated to the reduced Bfd concentration in the solution (Figure 2-9D) [8].

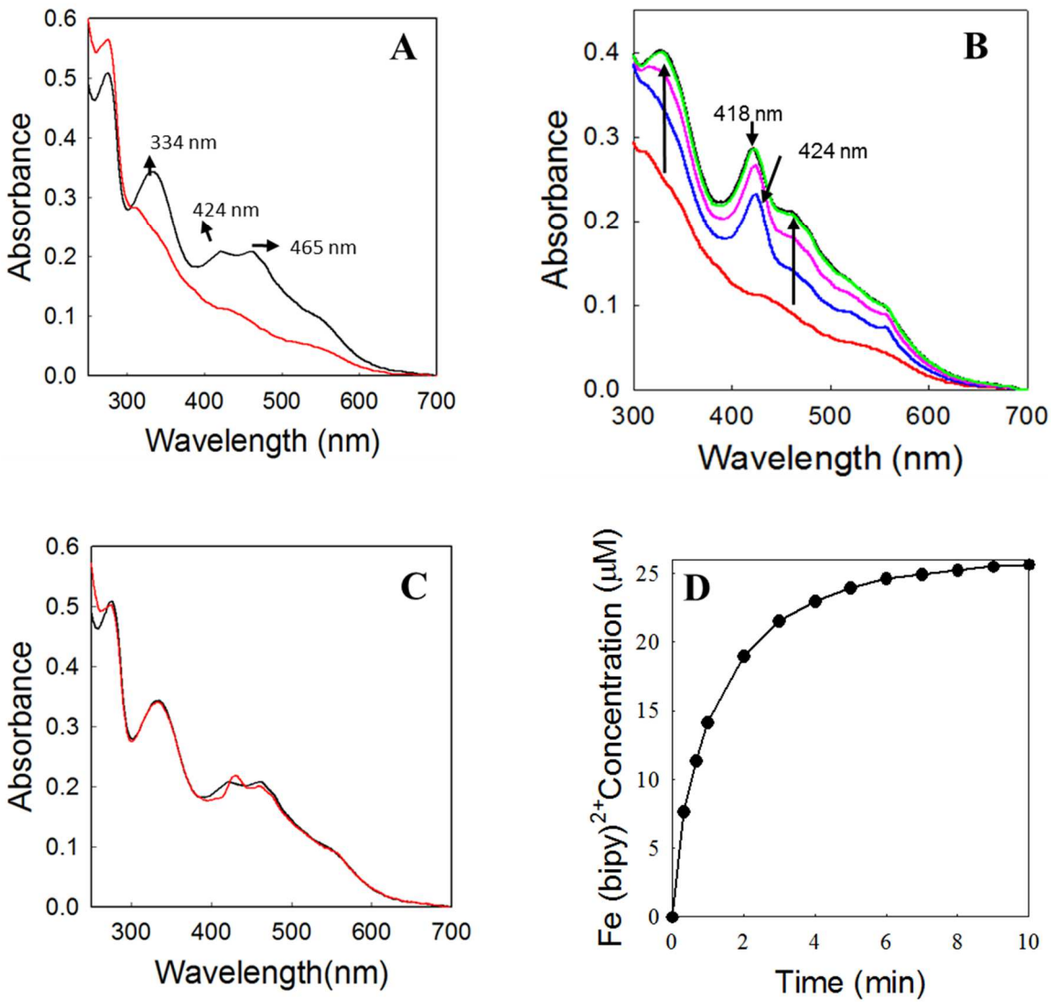

Figure 2-9 (A) UV-vis spectra of 30 μM oxidized Pa-Bfd (black) and reduced Pa-Bfd (red) upon addition of 0.8 equiv of sodium dithionite relative to oxidized Pa-Bfd [8]. (B) Spectral change upon addition of 0.08 μM iron loaded Pa-BfrB (590 iron/protein) to the reduced Pa-Bfd: (red) spectrum prior to addition of Pa-BfrB. (blue) 20s, (pink) 1min, (green) 3min and (black) 5min after the addition of Pa-BfrB [8]. (C) Difference spectrum (red) obtained from subtracting a spectrum obtained from 0.08 μM Pa-BfrB from the black trace (5min) in Figure (B). The resulted difference spectrum (red) is identical as the original oxidized Pa-Bfd at 30 μM (black)

[8]. (D) Time dependent formation of $[Fe(bipy)_3]^{2+}$ complex due to the release of the Fe^{2+} during the reaction [8].

The Bfd Fold

The Pa-Bfd fold was revealed for the first time as a part of the X-ray crystal structure of the Pa BfrB-Bfd complex [8]. As shown in Figure 2-10A and B, in the asymmetric unit, there are three BfrB subunit dimers. Well-defined electron density corresponding to Bfd molecules are observed at the interface of each BfrB subunit dimer, above each of the heme molecules. As shown in Figure 2-10C and D, the Bfd fold is a helix-turn-helix fold. Residues C4, C6, C38 and C41 located in loops 1 and 3 coordinate the [2Fe-2S] cluster. The distances of Fe-Fe, Fe-S (Cys) and Fe-S^{2-} in the [2Fe-2S] cluster are similar to those observed in structures of [2Fe-2S] containing proteins. The average Fe-Fe distance is 2.85 Å, and the average Fe-S (Cys) and Fe-S^{2-} distances are 2.31 and 2.22 Å respectively. Loop 1 contains residues C4 and C6, followed by α-1, which is a 3-turn helix. Loop 2 follows α-1 helix and leads to a 2-turn helix α-2, the shortest helix in the structure. Loop 3 follows α-2 and contains residues C38 and C41. α-3, connected by L3, is the longest helix in the structure. α-3 has 4 turns and spans from residues C41 to C57, which is the last residue that has observable electron density. The missing electron density of the last six amino acids from C terminal of Bfd suggest the C terminal tail is disordered [8].

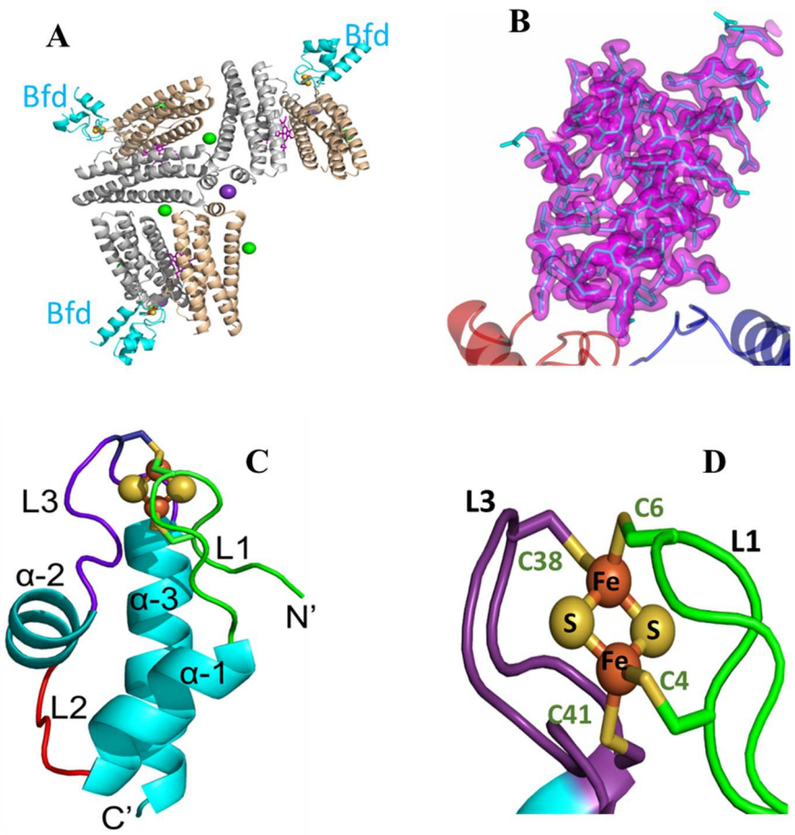

Figure 2-10 Pa-Bfd structure as a part of the Pa BfrB-Bfd complex (A) The asymmetric unit contains three BfrB subunit dimers, each of which associates with a Pa-Bfd molecule (cyan) [8]. (B) *Fo-Fc* omit map contoured at 3σ showing the electron density (magenta) of Bfd chain G [8]. (C) Helix-turn-helix structure of Pa-Bfd [8]. (D) The [2Fe-2S] cluster in Pa-Bfd is coordinated by C4 and C6 from L1, and C38 and C41 from L3 [8].

C-terminal truncated Bfd

Despite significant effort made to crystallize Pa-Bfd alone, the best crystals we could obtain were needle clusters, which did not diffract well. The structure of Pa BfrB-Bfd complex showed that the electron density of the last 6 amino acids from Pa-Bfd C-terminal are missing, which suggests that the C-terminal tail in Bfd is disordered. Hence, we hypothesized that the

disordered C-terminal tail in Pa-Bfd contributes to the difficulties in crystallizing this molecule alone. Consequently, we truncated the Pa-Bfd after Leu56 in an effort to obtain the high-resolution Pa-Bfd structure alone. We succeeded at growing crystals that diffracted to 1.25 Å, which were obtained from from Crystal Screen HT (Hampton Research) condition A1 (30% (v/v) 2-methyl-2,4-pentanediol, 100 mM sodium acetate pH 4.6, 20 mM $CaCl_2$). The crystallographic data is shown in Table 2-1.

Table 2-1 Crystallographic data of C-terminal truncated Bfd

	Bfd
Data Collection	
Unit-cell parameters (Å, °)	a=23.93, b=49.68, c=39.87, β=96.9
Space group	$P42_12$
Resolution (Å)[1]	49.68-1.25 (1.27-2.25)
Wavelength (Å)	1.0000
Temperature (K)	100
Observed reflections	86,612
Unique reflections	25,583
$\langle I/\sigma(I)\rangle$[1]	10.0 (2.3)
Completeness (%)[1]	99.6 (99.7)
Multiplicity[1]	3.4 (3.2)
R_{merge} (%)[1, 2]	5.5 (50.4)
R_{meas} (%)[1, 4]	8.5 (71.8)
R_{pim} (%)[1, 4]	4.5 (38.9)
Refinement	
Resolution (Å)	30.96-1.25
Reflections (working/test)	24,247/1,306
R_{factor} / R_{free} (%)[3]	13.3/15.7
No. of atoms (Bfd/Fe-S/water)	868/8/83
Model Quality	
R.m.s deviations	
Bond lengths (Å)	0.012
Bond angles (°)	1.786
Average B factor (Å^2)	
All Atoms	35.1
Bfd	13.8
Fe-S	10.7
Water	14.7
Coordinate error, maximum likelihood (Å)	0.12

Ramachandran Plot	
Most favored (%)	98.2
Additionally allowed (%)	1.8

1) Values in parenthesis are for the highest resolution shell.
2) $R_{merge} = \Sigma_{hkl}\Sigma_i |I_i(hkl) - \langle I(hkl)\rangle| / \Sigma_{hkl}\Sigma_i I_i(hkl)$, where $I_i(hkl)$ is the intensity measured for the ith reflection and $\langle I(hkl)\rangle$ is the average intensity of all reflections with indices hkl.
3) $R_{factor} = \Sigma_{hkl} ||F_{obs}(hkl)| - |F_{calc}(hkl)|| / \Sigma_{hkl} |F_{obs}(hkl)|$; Rfree is calculated in an identical manner using 5% of randomly selected reflections that were not included in the refinement.
4) R_{meas} = redundancy-independent (multiplicity-weighted) R_{merge}[10, 11]. R_{pim} = precision-indicating (multiplicity-weighted) R_{merge}[12, 13].

In the asymmetric unit cell, there are two Bfd molecules (Figure 2-11A). Alignment of the truncated Bfd molecule with full-length Bfd molecule shows a perfect overlay of the two structures (Figure 2-11 B.).

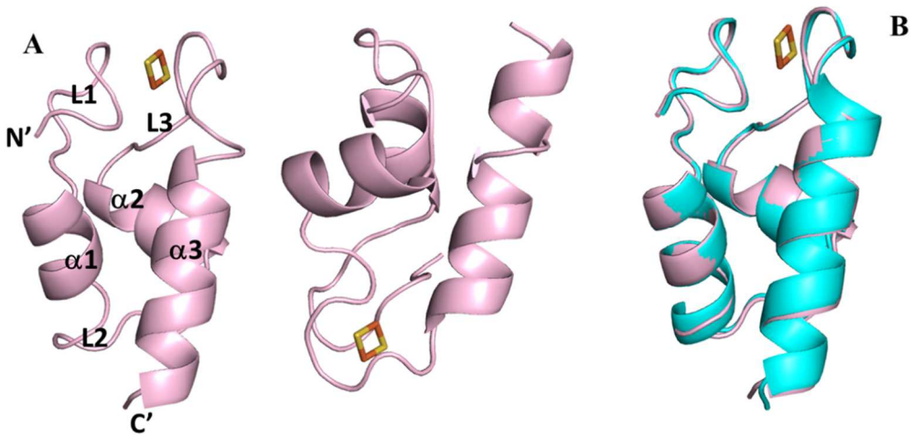

Figure 2-11 (A) In the asymmetric unit, there are two truncated Bfd molecules. (B) The truncated Bfd structure (pink) is identical to the full-length Bfd structure (cyan)

The Bfd fold is stabilized by phosphate

(1) Phosphate is incorporated into the Bfd fold

The three Bfd molecules in the asymmetric unit cell of the BfrB:Bfd complex are chain G, H and I respectively [8]. As shown in Figure 2-12 A, both chain I and chain G have crystal contacts with nearby complex molecules, while chain H is the only chain that does not experience crystal contacts. Therefore, compared to chain I and chain G, chain H is the chain that most closely represents solution conditions. The three Bfd chains are structurally similar, except that chain H has higher thermal factors and lacks electron density between residues 16 and 33. As shown in Figure 2-12B, the average B factor of chain H is 64.0 Å, which is much higher than chain G and I (25.8 and 29.0 Å) [8].

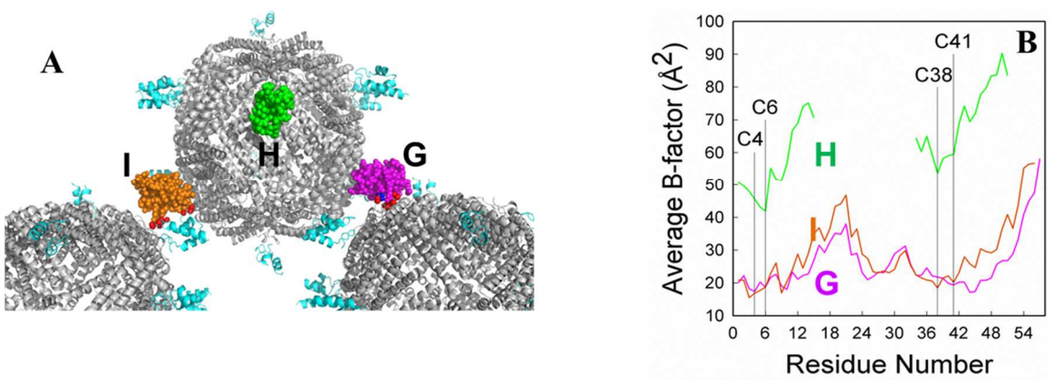

Figure 2-12 (A) In the asymmetric unit, BfrB (gray) binds Bfd (chain I, G and H). Bfd chain G and I experience crystal contacts (red) [8]. (B) Main chain average B-factors in Bfd chains G (magenta), I (orange) and H. The Cys ligands are highlighted by the vertical lines. The gap in the green trace (chain H) represents the missing electron density in chain H [8].

As shown in Figure 2-13A, the missing electron density in chain H (colored in gray), corresponds to the end of α-3, part of α-1, the whole of L2 and α-2, as well as a part of L3. In

contrast, in chain G, strong electron density corresponding to a phosphate ion is observed in this region (Figure 2-13B) [8]. The phosphate is coordinated by the side chains of R26, R29 and K46 and, via a crystal contact, by the side chain of K76 from a nearby BfrB molecule. Since R26, R29 and K46 are all positively charged, the phosphate ion is proposed to mediate otherwise repulsive interactions of these three residues [8]. Also, the phosphate enables the hydrophobic portions of these residues to pack against the Y25 side chain so that the α-2 helix could be stabilized by the hydrophobic interactions [8]. The stabilization of α-2 by phosphate maybe crucial for stabilizing the Bfd fold. This is because without the phosphate, the repulsive interactions from R26, R29 and K46 are likely to cause unfolding of the α-2 helix. The instability of α-2 could be transmitted by L3 and destabilize the [2Fe-2S] cluster. As mentioned earlier, the loss of [2Fe-2S] cluster would cause a further unfolding of the structure [8].

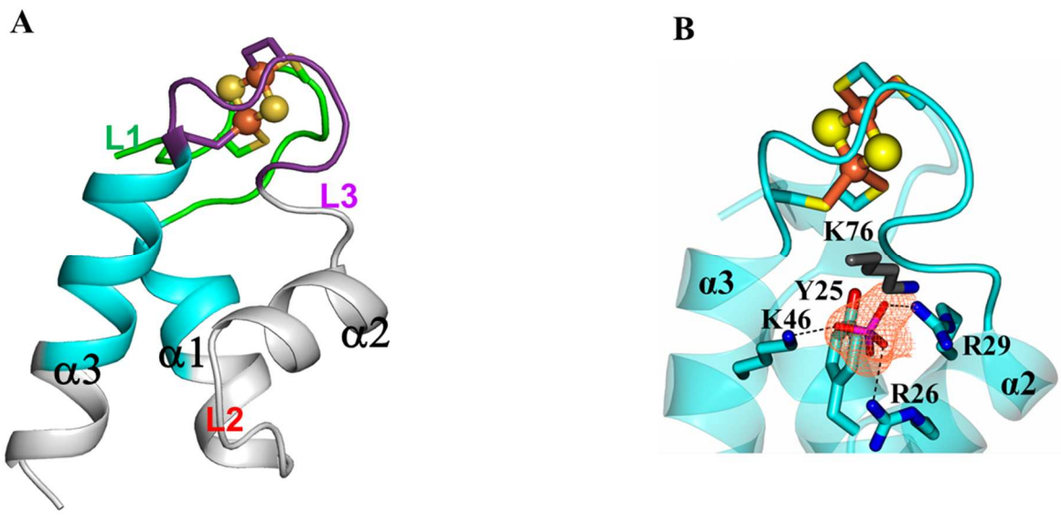

Figure 2-13 (A) The missing electron density in chain H is represented by gray color. (B) Electron density modeled as a phosphate ion is observed in chain G. The phosphate ion is coordinated by R26, R29 and K46 in chain G, as well as K76 in a nearby BfrB molecule [8].

(2) Removal of phosphate in solution causes loss of the [2Fe-2S] cluster

Holo-Bfd dissolved in a buffer containing 50 mM potassium phosphate, 150 mM NaCl and 5 mM DTT was diluted 40 times into a buffer containing 150 mM Tris-Base, 250 mM NaCl and 3 mM TCEP. Therefore, the phosphate concentration in the buffer decreased to ~ 1.2 mM after the dilution. As shown in Figure 2-14A, upon decreasing the phosphate concentration, the characteristic [2Fe-2S] cluster peaks seen in the Pa-Bfd decrease dramatically within 3 h, leaving only the 280 nm peak and a shoulder at ~320 nm (black trace) in the UV-vis spectrum, observations that are indicative of loss the [2Fe-2S] cluster [8].

The CD spectra of Pa apo-Bfd in the phosphate buffer (black) and in Tris-Base buffer (red) are shown in Figure 2-14B. Compared to the Pa apo-Bfd in phosphate buffer ($[\theta]_{222}/[\theta]_{203} = R \sim 0.45$), the Pa apo-Bfd in Tris buffer shows lower $[\theta]_{222}$ and additional blue shift of the high-energy transition toward 201nm, with R~0.23. This indicates that the Pa apo-Bfd loses α-helical structure upon removal of the phosphate, which supports the notion that the phosphate is important to stabilize the Bfd fold [8].

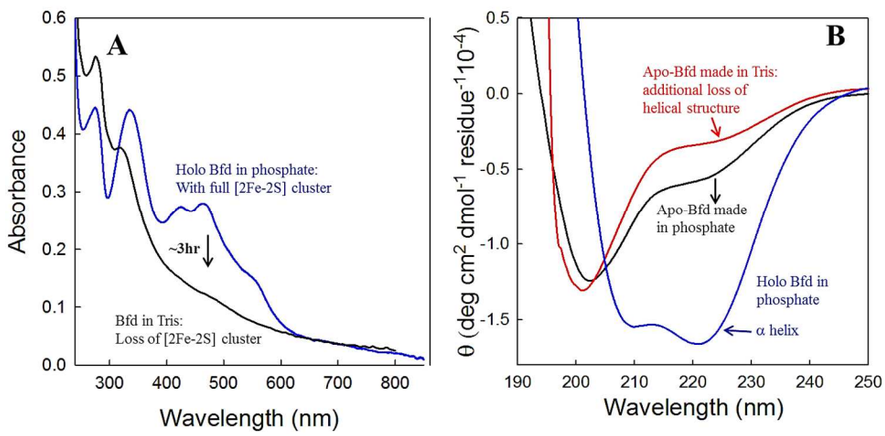

Figure 2-14 (A) Bfd loses [2Fe-2S] cluster in the absence of phosphate [8]. (B) Bfd loses helical structure in the absence of phosphate [8].

(3) Removal of the phosphate and the presence of Zn^{2+} accelerate the loss of the [2Fe-2S] cluster

As shown in Figure 2-15, upon diluting the Pa-Bfd stock into the buffer containing 150 mM Tris-Base, 150 mM NaCl, 5 mM TCEP, 125 μM (ZnSO4.7H2O), pH 7.8, a rapid decrease of the [2Fe-2S] cluster characteristic peaks was observed within 5 min of the reaction (red trace). After 30 min of the reaction, the [2Fe-2S] cluster peaks have completely disappeared, only leaving an ill-defined shoulder ~ 320 nm (green). The resultant protein was dialyzed against 150 mM Tris-Base, 150 mM NaCl, 5 mM TCEP, 125 μM (ZnSO4.7H2O), pH 7.8 for 3hrs. The UV-vis spectrum remains stable after the dialysis. Analysis of iron and protein concentration in the protein after dialysis shows a ratio of iron/protein of ~1.1. This suggest that disassembly of the [2Fe-2S] cluster in Bfd might result in the formation of a mononuclear iron center bound to Bfd. However, this hypothesis needs to be supported with additional experiments and spectroscopy.

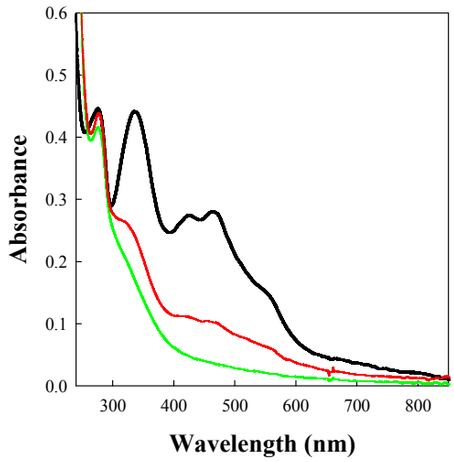

Figure 2-15 Pa-Bfd loses the [2Fe-2S] cluster in the buffer of 150 mM Tris-Base, 150 mM NaCl, 5 mM TCEP, 125 μM (ZnSO4.7H2O), pH 7.8. Black: Pa-Bfd in phosphate buffer. Red: 5 min of the reaction. Green: 30 min of the reaction

(4) Truncated Bfd needs phosphate to stabilize the fold

As describe above for full-length Bfd, structural and solution phase investigations were conducted to analyze the significance of phosphate binding to truncated Bfd. . As proposed above, in the full-length Bfd fold, R26, R29 and K46 interact with phosphate ion in solution to organize the structure delineated by L2-α-2-L3. Aligning the structure of truncated Bfd (pink) with that of full-length Pa-Bfd (cyan) molecule shows differences in the side chains of R26 and R29 (Figure 2-16A), which in the structure of the truncated Bfd form ionic interactions with a nearby molecule in the crystal (purple) through crystal contacts (Figure 2-16B). In other words, under the particular crystallization condition, 0.5 μL solution of Bfd in 50 mM potassium phosphate, 150 mM NaCl, 5mM DTT, pH 7.0, mixed with 0.5 μL crystallization solution (30% (v/v) 2-methyl-2, 4-pentanediol, 100 mM sodium acetate pH 4.6, 20 mM $CaCl_2$), the stabilization provided by phosphate in solution is replaced by contacts in the crystal. Hence, although phosphate is important to stabilize Bfd in solution, as the protein crystallizes, the role of phosphate can be replaced by interactions (crystal contacts) with other Bfd molecules in the crystal. However, when phosphate is removed in solution, the peaks characteristic of a [2Fe-2S] cluster in truncated Bfd decrease in intensity and disappear upon lowering the phosphate concentration. Hence, thse findings indicate that phosphate binding serves a structural role in the stabilization of holo-Bfd, full-length or truncated.

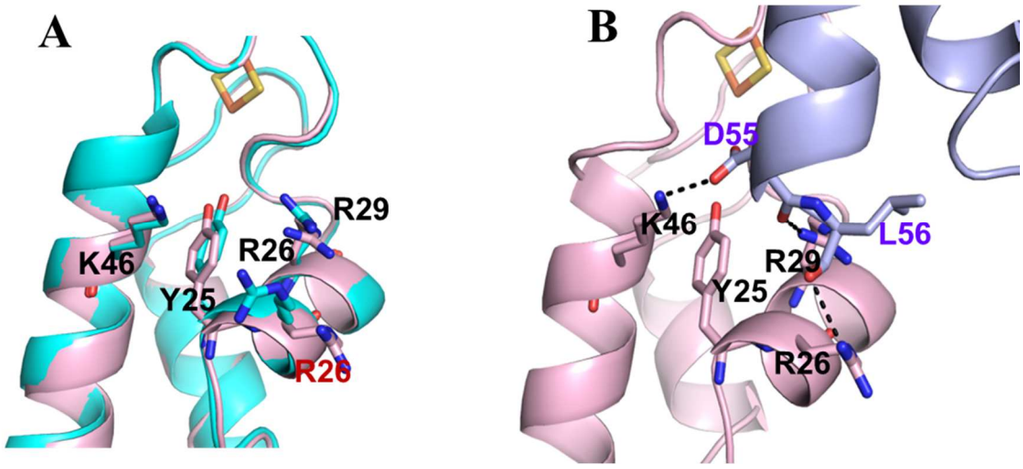

Figure 2-16 View of the "phosphate binding region" in truncated Bfd. (A) Overlay the structure of truncated Pa-Bfd (pink) and full-length Bfd (cyan) shows that the R26 and R29 in truncated structure have shifted compared to the full-length structure. (B) The "phosphate binding region" in the truncated Bfd is stabilized by a nearby molecule through crystal contacts.

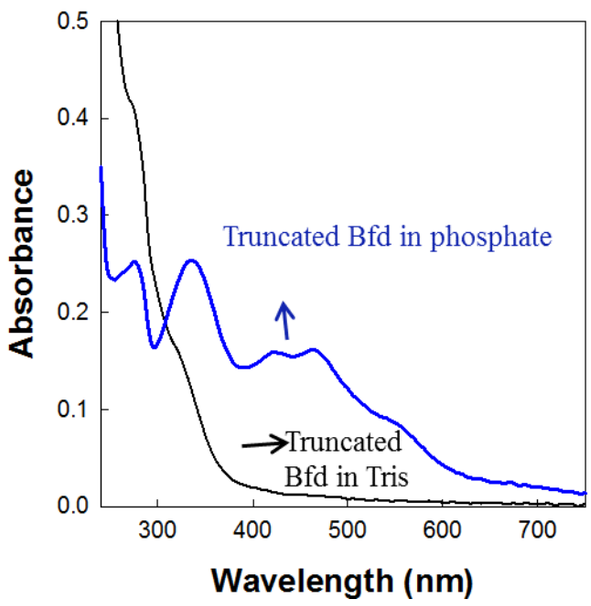

Figure 2-17 Removal of the phosphate from the truncated Bfd results loss of [2Fe-2S] cluster.

Overall Structure of the BfrB-Bfd complex

The crystal structure of the BfrB-Bfd complex was determined at 2.0 Å resolution. The crystallographic data is shown in Table 2-2. As mentioned before, the asymmetric unit cell contains three BfrB subunit dimers, each associated with a Bfd molecule above the heme molecule. Hence, the 24-mer BfrB binds 12 Bfd molecules (Figure 2-18A). Alignment of the ferroxidase center in the complex and the ferroxidase center in BfrB alone show that they adopt identical conformations (Figure 2-18B).

Table 2-2. Crystallographic data for BfrB-Bfd refined to 2.0Å resolution.

	BfrB-Bfd
Data Collection	
Unit-cell parameters (Å, °)	a=135.81, c=200.89
Space group	$P42_12$
Resolution (Å)[1]	200.89-2.00 (2.03-2.00)
Wavelength (Å)	1.0000
Temperature (K)	100
Observed reflections	1,120,495
Unique reflections	125,332
$\langle I/\sigma(I)\rangle$[1]	15.2 (3.0)
Completeness (%)[1]	100 (100)
Multiplicity[1]	8.9 (9.2)
R_{merge} (%)[1, 2]	11.7 (80.5)
R_{meas} (%)[1, 4]	13.3 (90.3)
R_{pim} (%)[1, 4]	4.4 (29.6)
Refinement	
Resolution (Å)	47.73-2.0
Reflections (working/test)	118,964/6,294
R_{factor} / R_{free} (%)[3]	15.2/18.3
No. of atoms (BfrB/Bfd/Heme/Fe-S/K^+/Na^+/phosphate/water)	7,714/1,087/258/12/3/6/5/1,062
Model Quality	
R.m.s deviations	
Bond lengths (Å)	0.011
Bond angles (°)	1.185
Average B factor (Å^2)	
All Atoms	24.0
BfrB/Bfd	20.9/41.4
Heme/Fe-S/ K^+/Na^+/phosphate	22.9/26.9/15.3/24.0/35.7
Water	39.1
Coordinate error, maximum	0.22

likelihood (Å)	
Ramachandran Plot	
Most favored (%)	99.3
Additionally allowed (%)	0.7

1) Values in parenthesis are for the highest resolution shell.

2) $R_{merge} = \Sigma_{hkl}\Sigma_i |I_i(hkl) - \langle I(hkl)\rangle| / \Sigma_{hkl}\Sigma_i I_i(hkl)$, where $I_i(hkl)$ is the intensity measured for the *i*th reflection and $\langle I(hkl)\rangle$ is the average intensity of all reflections with indices hkl.

3) $R_{factor} = \Sigma_{hkl} ||F_{obs}(hkl)| - |F_{calc}(hkl)|| / \Sigma_{hkl} |F_{obs}(hkl)|$; Rfree is calculated in an identical manner using 5% of randomly selected reflections that were not included in the refinement.

4) R_{meas} = redundancy-independent (multiplicity-weighted) R_{merge}[2, 12]. R_{pim} = precision-indicating (multiplicity-weighted) R_{merge}[13, 14].

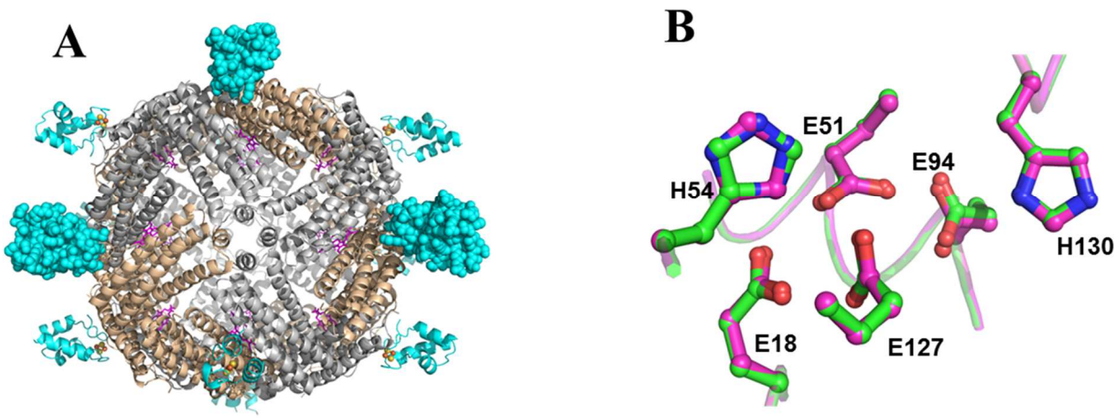

Figure 2-18 (A) BfrB-Bfd complex structure (4E6K) shows that 12 Bfd molecules (cyan) bind to a 24-assembly BfrB molecule [8]. (B) Alignment of the ferreoxidase center of the free BfrB (pink) and Bfd in the complex (green) [8].

The Pa-BfrB−Bfd Interface

At the BfrB-Bfd complex interface, a Bfd molecule binds between two BfrB subunits resulting in the burial of 607 Å^2 at the interface of the complex [8]. The identities of residues

participating at the interface and their relative contribution to the buried surface are shown in Figure 2-19. The contribution of Bfd residues and BfrB residues to the total buried surface are plotted in Figure 2-19A and B respectively. The (*) and (:) on top of each bar respectively indicate that a particular residue is conserved or conservatively replaced in the amino acid sequence alignments of several BfrB and Bfd sequences from a number of pathogens (Table 2-3A and B). The conservation of the interacting residues at the interface suggest that the Pa BfrB-Bfd interaction is biologically relevant and support the notion that the Pa BfrB-Bfd interaction is a wide spread mechanism for regulating cytosolic iron level in various Gram negative bacteria [8].

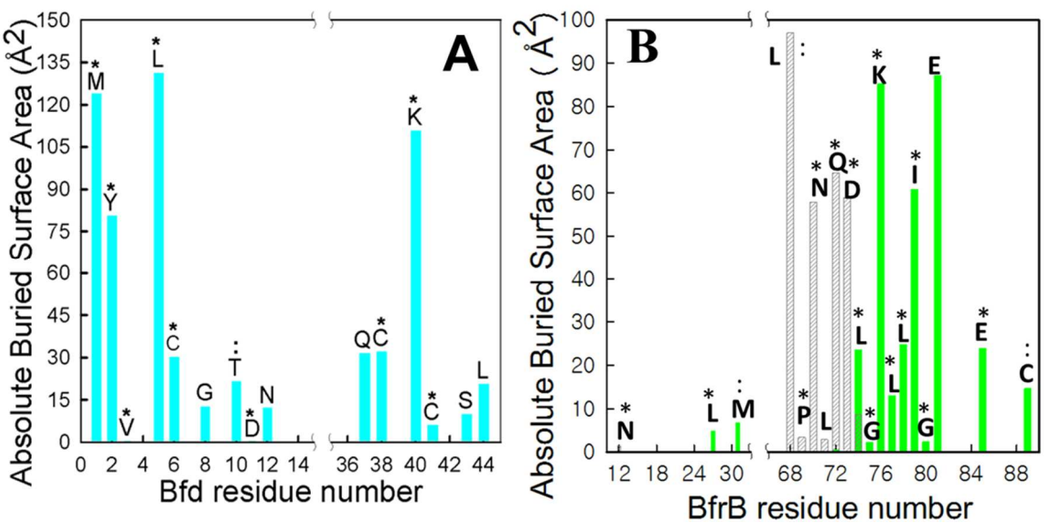

Figure 2-19 Per-residue plot of surface area buried at the complex interface contributed from (A) [8] Bfd residues shown in cyan and (B) BfrB residues from subunit A (green) and subunit B (gray) [8].

Table 2-3A Sequence alignment of *Pa*-Bfd with Bfd-like molecules from different bacterial species. Conserved cysteine residues coordinating iron in the [2Fe-2S] cluster are highlighted by an arrow (↓) and residues buried at the *Pa*-BfrB-Bfd interface are denoted by (^). Conserved residues across the alignment are in red, conservative substitutions in green and semi-conservative substitutions in blue, sequence numbering according to *Pa*-Bfd [8]

```
                                      1       10        20        30        40        50
                                      |↓ ↓    |         |         |        ↓|↓  ↓     |
Pseudomonas aeruginosa PAO1       -----MYVCLCQGVTDNQIRDAIYEGCCS-YREVREATGVGTQCGKCACLAKQVVRETL-
Escherichia coli O157             -----MYVCLCNGVSDKKIRQAVRQFHPQSFQQLRKFIPVGNQCGKCIRAAREVMQDEL-
Escherichia coli K12              -----MYVCLCNGISDKKIRQAVRQFSPHSFQQLKKFIPVGNQCGKCVRAAREVMEDEL-
Salmonella typhimurium            -----MYVCLCNGISDKKIRQAVRQFHPQSFQQLRKFIPVGNQCGKCIRAAREVMQDEL-
Salmonella enterica serovar Typhi -----MYVCLCNGISDKKIRQAVRQFHPQSFQQLRKFIPVGNQCGKCIRAAREVMQDEL-
Salmonella enterica choleraesuis  -----MYVCLCNGISDKKIRQAVRQFHPQSFQQLRKFIPVGNQCGKCIRAAREVMQDEL-
Klebsiella pneumoniae             -----MYVCLCNGVSDKKIRQVVRQFQPQSFQQLRKFVPVGNQCGKCVRAAREVMEDEL-
Yersinia pestis                   -----MYVCLCNAVSDKVIRKAVRQHQPHTVKQLRQLVPIGSDCGKCIRQAREILIEEL-
Yersinia pseudotuberculosis       -----MYVCLCNAVSDKVIRKAVRQHQPHTVKQLRQLVPIGSDCGKCIRQAREILIEEL-
Yersinia enterocolitica           -----MYVCLCNAVSDKVIRNAVRQHHPHTIQQLRQLVPIGTDCGKCIRQAREILIEER-
Aeromonas salmonicida             -----MYVCLCRGITDTQIRKAVQAGKSE-FRQLKQSLEVGAQCGKCVRMTMEIIAAELD
Vibrio cholerae El                -----MYVCLCHGVSDKKIRRLVAEQGITDIKGIKRCTALGSQCGKCVRQAKEIIEESL-
Vibrio cholerae 0395              -----MYVCLCHGVSDKKIRRLVAEQGITDIKGIKRCTALGSQCGKCVRQAKEIIEESL-
Vibrio vulnificus                 -MSCNMYVCLCHGVSDKKIRKLVIEQGVADIRGIKKCTALGSQCGKCIRMAKEIINETA-
Shigella flexneri 2a 2457T        -----MYVCLCNGVSDKKIRQAVRQFHPQSFQQLRKFIPVGNQCGKCIRAAREVMQDEL-
Shigella flexneri 2a str301       -----MYVCLCNGVSDKKIRQAVRQFHPQSFQQLRKFIPVGNQCGKCIRAAREVMQDEL-
Shigella dysenteriae              -----MYVCLCNGVSDKKIRQAVRQFHPQSFQQLRKFIPVGNQCGKCIRAAREVMQDEL-
Erwinia carotovora                -----MYVCLCNAISDKAIRNAVRQHQPQSMQQLRKLVPIGTDCGKCIRQARVIFEEEQ-
Enterobacter cloacae              -----MYVCLCNGVSDTKIRQAVRQFQPQSFQQLRKFVPVGNQCGKCVRAAREIMQDEL-
Serratia sp.                      -----MYVCLCNAVTDKAIRKAVRQHNPHTMKQLRELVPIGTDCGKCIRQARQIMVEES-
Citrobacter koseri                -----MYVCLCNGVSDKKIRQAVRQFHPQSFQQLRKFIPVGNQCGKCVRAAREVMQDEL-
Acinetobacter sp.                 MRMTLMYVCLCRGITDQDIKDAVASGAES-YREVRERLDLGTCCGRCAPEAKSIINEEL-
                                       ^^^ ^^ ^ ^^^                       ^^ ^^ ^^

                                            60        70
                                            |         |
Pseudomonas aeruginosa PAO1       ----NDLQSAQPVPAFGTTAFVAA
Escherichia coli O157             ----MQMPEFKEIA----------
Escherichia coli K12              ----MQLPEFKESA----------
Salmonella typhimurium            ----TQMPEFKEIA----------
Salmonella enterica serovar Typhi ----TQMPEFKEIA----------
Salmonella enterica choleraesuis  ----TQMPEFKEIA----------
Klebsiella pneumoniae             ----TTMPEFKEIA----------
Yersinia pestis                   ----ANIPEMNDVA----------
Yersinia pseudotuberculosis       ----ANIPEMNDVA----------
Yersinia enterocolitica           ----ANIPEMNDVA----------
Aeromonas salmonicida             KAELETAPLYYEVA----------
Vibrio cholerae El                ------IAQFKLAS----------
Vibrio cholerae 0395              ------IAQFKLAS----------
Vibrio vulnificus                 ------PALFKQAS----------
Shigella flexneri 2a 2457T        ----MQMPEFKEIA----------
Shigella flexneri 2a str301       ----MQMPEFKEIA----------
Shigella dysenteriae              ----MQMPEFKEIA----------
Erwinia carotovora                ----AKIPDMYKVA----------
Enterobacter cloacae              ----MQIPEYKEIA----------
Serratia sp.                      ----GTIIPMHEVA----------
Citrobacter koseri                ----MQMPEFKEIA----------
Acinetobacter sp.                 ----AEIAARISVAA---------
```

Table 2-3B Sequence alignment of *Pa*-BfrB and Bfr from different bacterial species. Residues buried at the *Pa*-BfrB-Bfd interface are denoted by (^). Conserved residues across the alignment are in red, conservative substitutions in green and semi-conservative substitutions in blue [8].

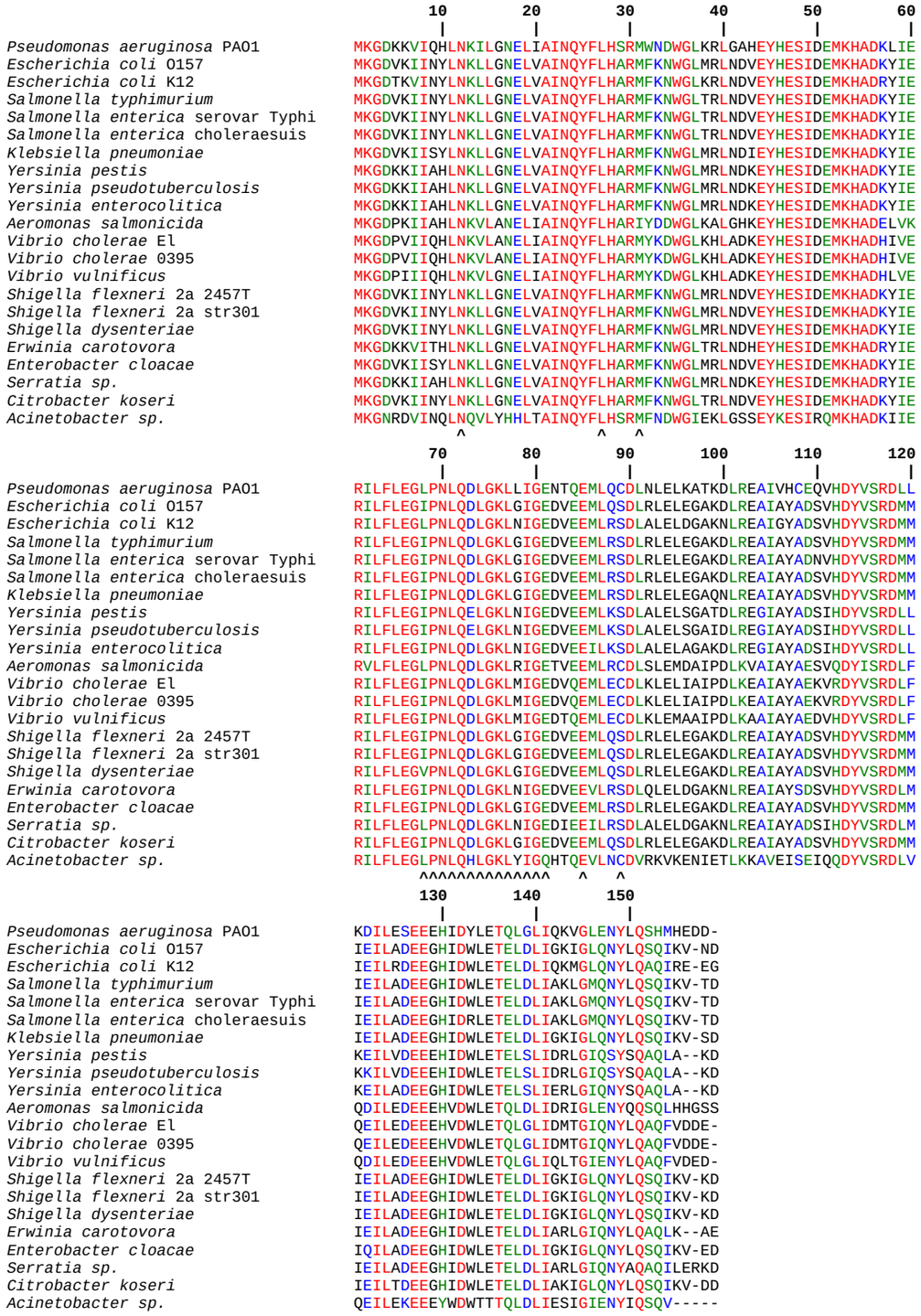

A zoomed-in view of the Pa BfrB-Bfd interface is shown in Figure 2-20. Pa-Bfd (cyan) is bound at the interface of Pa-BfrB subunit A (green), and subunit B (gray). Y2, L5, K40 and M1 are the four residues with the largest contributions to the buried Pa Bfd surface: (1) Bfd Y2 is held by a binding cleft on BfrB surface formed by E_A^{81} and L_B^{68}, (2) Bfd L5 buries in a pocket on the BfrB surface formed by BfrB L_B^{68}, P_B^{69}, N_B^{70}, L_B^{71}, Q_B^{72}, L_A^{77} and I_A^{79}, (3) Bfd K40 interacts hydrophobically with BfrB K_A^{76} and forms hydrogen bonds with carbonyl oxygen of BfrB Q_B^{72} and L_A^{74}, and (4) the Bfd amine group of M1 forms hydrogen bonds with carboxyl side chains of E_A^{85} and E_A^{81} on BfrB and interacts hydrophobically with BfrB L_A^{77} L_A^{78}, I_A^{79}, G_A^{80} and C_A^{89}.

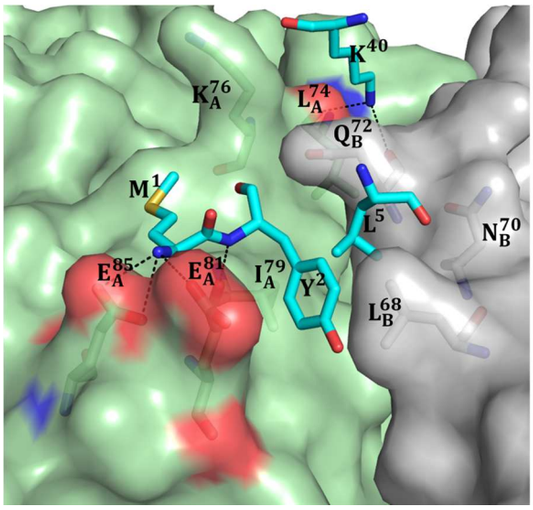

Figure 2-20 BfrB-Bfd interface showing the Bfd residues in cyan and BfrB subunit A and B in green and gray, respectively. The oxygen and nitrogen atoms are shown as red and blue, respectively. The H-bonding interactions are labeled with dotted lines.

Bfd [2Fe-2S] cluster electron transfer pathway to the BfrB heme

From the functional studies discussed above, we concluded the role of the [2Fe-2S] cluster is to transfer electrons to the heme in Pa-BfrB. The structure of the Pa BfrB−Bfd complex reveals that the edge-to-edge distance between the [2Fe-2S] cluster in Pa-Bfd and

heme in Pa-BfrB is 15.1 Å [8]. Using the coordinates of the Pa Bfr-Bfd complex, the most probable path for electron transfer from the [2Fe-2S] cluster to the heme was calculated with the aid of the program Harlem. The electron is likely to proceed from S2 in the iron sulfur cluster of Pa-Bfd to a heme vinyl β carbon (CBB) in Pa-BfrB, via conserved residues Q72 and L71 in subunit B (Figure 2-21) [8].

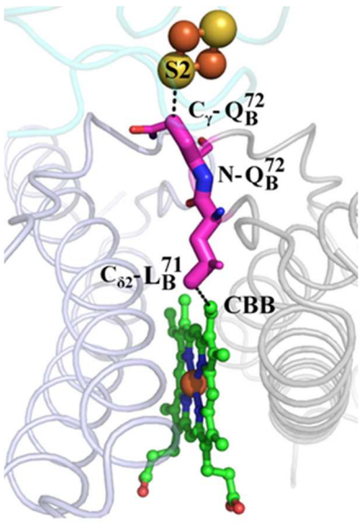

Figure 2-21 Best electron transfer path from [2Fe-2S] cluster to heme calculated by the program Harlem [8].

Taken together, the results from the *in vitro* functional studies, the structure of the BfrB-Bfd complex, and the calculation of the electron transfer path allow us to summarize the process of electron transfer from the Bfd to the core Fe^{3+} in Figure 2-22, where the [2Fe-2S] cluster mediates electrons to heme, and the heme further passes the electrons to the BfrB Fe^{3+} core to reduce and mobilize the stored irons.

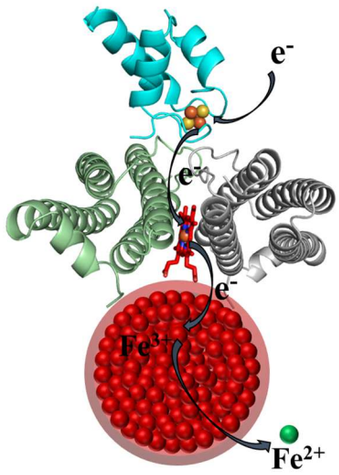

Figure 2-22 [2Fe-2S] cluster transfers electron via heme to the core Fe^{3+} to mobilize Fe^{2+}

Discussion

Bfd fold is a versatile metal binding motif

As mentioned above, sequence alignments of Pa Bfd and Bfd in different bacteria show that in Bfd four conserved cysteines are arranged in a unique C-X_1-C-X_{31-32}-C-X_2 motif, which is distinct from the C-X_5-C-X_2-C-X_{37}-C arrangement in classical ferredoxins [6]. Bfds are ~50 residues shorter than [2Fe-2S] ferredoxins from bacteria, plants, fungi, and vertebrates [6]. The helix-turn–helix fold of Bfd is also distinct from the classical [2Fe-2S] ferredoxins, which usually incorporates a β sheet. Although the [2Fe-2S] cluster in Pa-Bfd has been shown to function as electron carrier in Pa-BfrB iron mobilization process, yet there might be other functions of Bfd that haven't been explored. For example, the possibility that the Bfd also functions as a scaffold for [2Fe-2S] cluster assembly has not been excluded. Therefore, we conclude that Bfd is a class of [2Fe-2S] ferredoxin distinct from the classical ferredoxins.

Using the Bfd sequence to search database [8, 14] shows that the Bfd sequence matches a large, manually curated Pfam fimily, Fer2_BFD (PF04324). This family contains single and multiple domain proteins where the C-X1-C arrangement is highly conserved and the C-X2-C arrangement is partially conserved. The Fer2_Bfd sequence has been found in a variety of multidomain enzymes, such as nitrate, nitrite, and sulfite reductases, FAD-dependent oxidoreductases, nitrogen fixation (NifU) proteins, and copper and mercury transport proteins. Searching and aligning the Bfd structure using I-COFACTOR [15], DALI [16] and PdBeFold[17] strongly suggest that the Bfd fold has been observed for the first time in a single domain protein. However, the Bfd fold matches closely to certain portions of several multidomain proteins. For example, heterooctameric proline dehydrogenase (PDH1) from Pirococcus Horikoshii does not have significant sequence similarity to Bfd, however, a small portion of its α-subunit (magenta) is found to contain an equivalent of the Bfd fold (cyan) (Figure 2-23A) [8]. Chaperone CopZ from Archaeoglobus fulgidus is a two-domain protein that binds a Zn^{2+} and a [2Fe-2S] cluster in its N-terminal domain. It is a member of the Fer2_BFD family, who shares 60% sequence similarity with Pa-Bfd in the stretch flanking the C-X1-C motif. As shown in Figure 2-23B, in CopZ-NT, the [2Fe-2S] cluster is coordinated by C75, C77, C109 and C119. The C75 an C77 in CopZ are structurally equivalent to the C4 and C6 in Bfd. A subsequent α-helix in CopZ-NT (magenta) is also aligned with the α-1 helix in Pa-Bfd (cyan). C119 in CopZ is structurally equivalent to C41 in Pa-Bfd. In contrast, C109 is on a on a one-turn α-helix (green) in CopZ-NT and therefore is structurally distinct from C38 in Pa-Bfd L3. Taken together, the structural and sequence alignments above show that Bfd fold is a versatile metal-binding structural motif that has been incorporated into larger proteins with various functions, both from the Fer2_BFD family and non Fer2_BFD family [8].

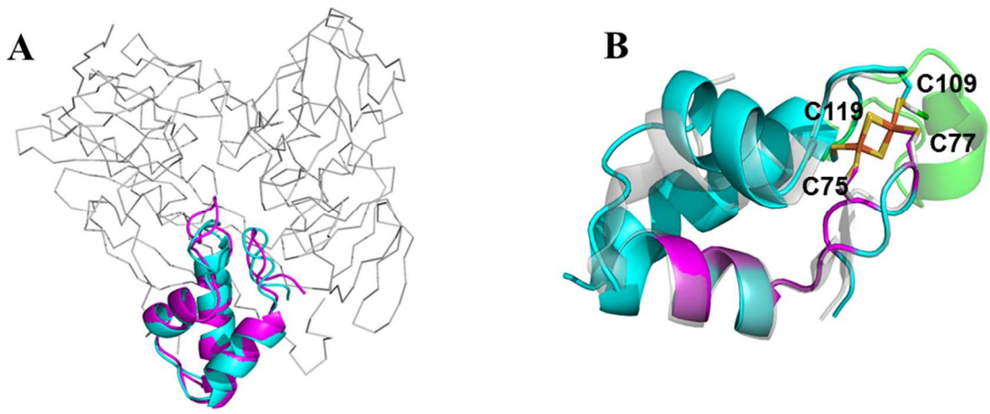

Figure 2-23 (A) Structural alignment of Pa-Bfd (cyan) with PDH1 (PDB:1Y56) shows that Bfd matches a proportion of the a-subunit of PDH1 (magenta) [8]. (B) Structural alignment of Bfd with a portion of the N'-terminal domain of CopZ-NT (PDB:2HU9) [8]

Phosphate is important for stabilizing the Bfd fold

From the structural analysis as well as UV-vis and CD spectral analysis above, phosphate is important to stabilize the Bfd fold. In addition, this idea was also proved by comparing the structural fluctuations in the phosphate-bound Pa-Bfd and phosphate –free Pa-Bfd structures *in silico* using a coarse-grained normal-mode analysis [8]. As shown in Figure 2-24, the calculation suggest that in the phosphate bound structure (Figure 2-24A), the residue G21, C38, C39 and K40 have larger fluctuations than other residues. Removal of phosphate causes a relatively large increase in the fluctuations of Y25, R26, and R29 in α-2 and A42 and K46 in α-3 (Figure 2-24B)[8]. This is consistent with the structural analysis that the binding of the phosphate stabilizes these residues on α-2 and α-3 helices. In addition, this conclusion is also supported by the facts that (1) the recombinant Pa-Bfd can only be purified in a phosphate buffer. (2) The preparation and isolation of apo-Bfd can only be achieved with the high concentration of phosphate. (3) The Pa BfrB-Bfd complex can only be obtained if both proteins

are dissolved in phosphate buffer and if the crystallization solution contains high phosphate concentrations [8].

Taken together, the results from crystallography biochemical experiments in solution and experiments in *silico* allow us to conclude that in solution Bfd experiences an equilibrium between a folded α-helical structure and a partially disordered structure, which is regulated by the binding of the phosphate ion. Since the repulsive interactions from R26, R29 and K46 contribute to the instability of the α-2 helix, we propose that mutating one of the R26 or R29 residues to a negatively charged residue, for example, Glu, may stabilize this region so that the Bfd fold may be stabilized without the need of phosphate. However, more experiments need to be carried out to support this idea.

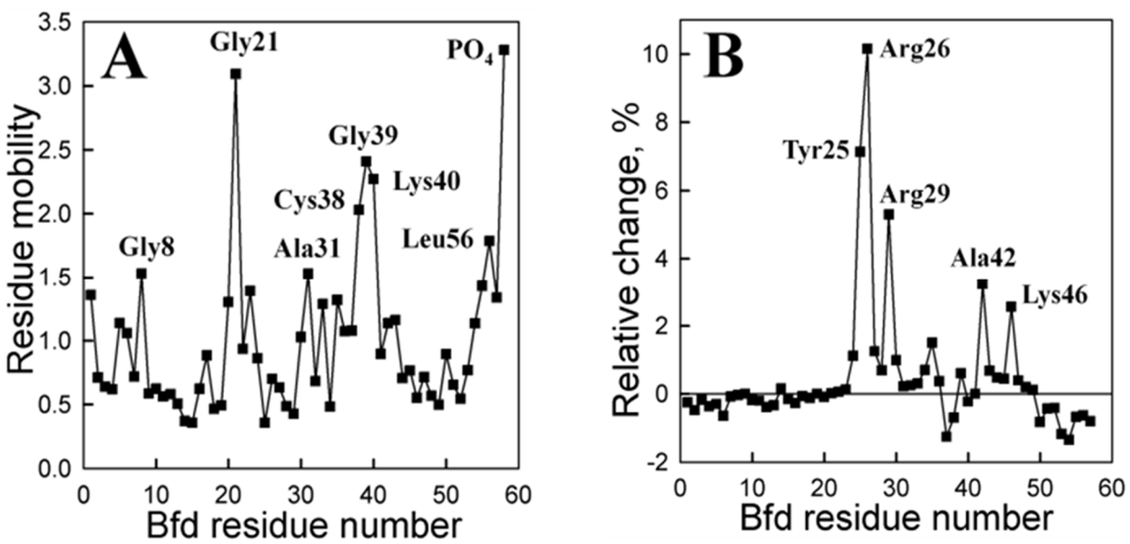

Figure 2-24 *In silico* prediction shows the phosphate stabilizes the Pa-Bfd fold. (A) Plot of per residue mobility in the phosphate-bound Bfd structure [8]. (B) Plot of the relative change of the mean square fluctuation of Bfd residues upon removing the phosphate from the Bfd structure [8].

References

1. Beinert, H., R.H. Holm, and E. Munck, *Iron-sulfur clusters: nature's modular, multipurpose structures.* Science, 1997. **277**(5326): p. 653-9.
2. Johnson, D.C., et al., *Structure, function, and formation of biological iron-sulfur clusters.* Annu Rev Biochem, 2005. **74**: p. 247-81.
3. Cassier-Chauvat, C. and F. Chauvat, *Function and Regulation of Ferredoxins in the Cyanobacterium, Synechocystis PCC6803: Recent Advances.* Life (Basel), 2014. **4**(4): p. 666-80.
4. Holden, H.M., et al., *Structure-function studies of [2Fe-2S] ferredoxins.* J Bioenerg Biomembr, 1994. **26**(1): p. 67-88.
5. Ta, D.T. and L.E. Vickery, *Cloning, sequencing, and overexpression of a [2Fe-2S] ferredoxin gene from Escherichia coli.* J Biol Chem, 1992. **267**(16): p. 11120-5.
6. Wang, A., et al., *Biochemical and structural characterization of Pseudomonas aeruginosa Bfd and FPR: ferredoxin NADP+ reductase and not ferredoxin is the redox partner of heme oxygenase under iron-starvation conditions.* Biochemistry, 2007. **46**(43): p. 12198-211.
7. Weeratunga, S.K., et al., *Binding of Pseudomonas aeruginosa apobacterioferritin-associated ferredoxin to bacterioferritin B promotes heme mediation of electron delivery and mobilization of core mineral iron.* Biochemistry, 2009. **48**(31): p. 7420-31.
8. Yao, H., et al., *The structure of the BfrB-Bfd complex reveals protein-protein interactions enabling iron release from bacterioferritin.* J Am Chem Soc, 2012. **134**(32): p. 13470-81.

9. Ringeling, P.L., et al., *Iron metabolism in Rhodobacter capsulatus. Characterisation of bacterioferritin and formation of non-haem iron particles in intact cells.* Eur J Biochem, 1994. **223**(3): p. 847-55.

10. Evans, P.R., *An introduction to data reduction: space-group determination, scaling and intensity statistics.* Acta Crystallogr D Biol Crystallogr, 2011. **67**(Pt 4): p. 282-92.

11. Evans, P., *Scaling and assessment of data quality.* Acta Crystallogr D Biol Crystallogr, 2006. **62**(Pt 1): p. 72-82.

12. Diederichs, K. and P.A. Karplus, *Improved R-factors for diffraction data analysis in macromolecular crystallography.* Nat Struct Biol, 1997. **4**(4): p. 269-75.

13. Weiss, M.S., *Global indicators of X-ray data quality.* Journal of Applied Crystallography, 2001. **34**: p. 130-135.

14. Punta, M., et al., *The Pfam protein families database.* Nucleic Acids Res, 2012. **40**(Database issue): p. D290-301.

15. Roy, A., J. Yang, and Y. Zhang, *COFACTOR: an accurate comparative algorithm for structure-based protein function annotation.* Nucleic Acids Res, 2012. **40**(Web Server issue): p. W471-7.

16. Holm, L. and P. Rosenstrom, *Dali server: conservation mapping in 3D.* Nucleic Acids Res, 2010. **38**(Web Server issue): p. W545-9.

17. Krissinel, E. and K. Henrick, *Secondary-structure matching (SSM), a new tool for fast protein structure alignment in three dimensions.* Acta Crystallogr D Biol Crystallogr, 2004. **60**(Pt 12 Pt 1): p. 2256-68.

CHAPTER III

Identifying the Hot Spot for the Interaction between Bacterioferritin (BfrB) and Its Associated Ferredoxin (Bfd)

Introduction

Iron is essential for bacteria due its involvement in multiple metabolic processes including respiration (heme-containing cytochromes, [Fe-S]-containing ferredoxins) and key enzymatic reactions ([Fe-S]-containing proteins, such as fumarase and aconitase of the TCA cycle) [1]. Pathogenic bacteria must obtain iron from the host to support growth, but humans maintain extremely low concentrations of free iron, which are further reduced during infections [2, 3]. In bacterial cells iron homeostasis plays a pivotal role in guarding against iron-induced toxicity caused by the propensity of free iron to stimulate the formation of reactive oxygen species (ROS) such as superoxide, hydrogen peroxide and the highly destructive hydroxyl radical [4]. Consequently, free levels of iron in bacteria are tightly regulated to insure sufficiency for metabolic needs, while preventing iron-induced toxicity [5]. In humans, iron is stored in ferritin (Ftn) [6], while in bacteria iron reserves are stored in Ftn and in bacterioferritin (Bfr), of which the latter is present only in bacteria [7, 8]. Ftns, bacterial Ftns and Bfrs assemble from 24 subunits into a spherical and hollow structure with an outer diameter of 120 Å and an inner diameter of 80 Å, where ≈3,500 iron atoms can be stored in the form of an Fe^{3+} mineral. Despite the superficial structural similarity between eukaryotic and prokaryotic Ftns and Bfrs, the small amino acid sequence homology (<18%) strongly influences the packing of the 24-mer protein shell, as well as its function [9, 10].

Bfrs are unique in possessing intrinsic heme groups, which are bound at 2-fold intersubunit sites by axial coordination of the heme-iron by methionine residues from adjacent subunits (Figure 3-1A). Hence, a 24-mer Bfr can be thought as being assembled from 12 subunit dimers, each harboring a heme, which is buried deep below the protein surface (≈13 Å), such that the heme propionates reach into the interior cavity (Figure 3-1B) [7]. Bfrs function by: (*i*) utilizing O_2 or H_2O_2 to oxidize Fe^{2+} and store Fe^{3+} in their internal cavity (core), and (*ii*) accepting electrons to reduce Fe^{3+} in their core and mobilize Fe^{2+} to the cytosol [11, 12] In bacteria, the free iron concentration (Fe^{2+}) required for Fur regulation is maintained by a dynamic equilibrium between Fe^{3+} stored in ferritin-like molecules and free, available Fe^{2+}. Hence, one function of ferritin-like molecules is to maintain the cytosolic Fe^{2+} concentrations that enable Fur, the major iron-responsive regulator which is conserved in many bacteria [13], to perform its broad range of regulatory functions that link iron homeostasis to broader bacterial metabolism [14-16]. For example, Bfr mutants of *Mycobacterium tuberculosis* suffer from iron-mediated oxidative stress and are unable to persist in mice and guinea pig models of infection [17, 18]. A Bfr-deficient mutant of *Nisseria gonorrhoeae* is growth impaired in iron-limited medium and more sensitive to killing by hydrogen peroxide [19], and in the plant pathogen *Erwinia chrysanthemi*, mutation of the bfr gene results in impaired iron utilization and growth defects [20].

Early studies with *Escherichia coli* suggested that mobilization of iron from Bfr requires interactions with a ferredoxin, dubbed Bfd (**b**acterioferritin-associated **f**erre**d**oxin) because the *bfd* gene is adjacent to the *bfr* gene [21-23]. Mining the global genetic response of *P. aeruginosa* to high and low iron conditions [24], we noticed that of the ≈120 genes reported to be up-regulated by low-iron conditions, the expression of *bfd* is up-regulated 200 fold and that of a gene coding for a ferredoxin reductase (*fpr*) is increased 3-fold[24]. In contrast, the *bfrB*

gene is down-regulated under iron limiting conditions [25]. The strong up-regulation of the *bfd* gene in response to low iron led us to hypothesize that the Bfd protein functions in the mobilization of iron stored in BfrB, by accepting electrons from the ferredoxin reductase (FPR) and transferring these to the ferric iron in BfrB for subsequent mobilization of Fe^{2+} (Figure 3-1B) [26]. We cloned the genes, characterized the BfrB, Bfd, and FPR proteins biochemically and structurally [27, 28], and showed that Bfd, FPR and NADPH are sufficient to mobilize iron from BfrB *in vitro* (Figure 3-1C) [26].

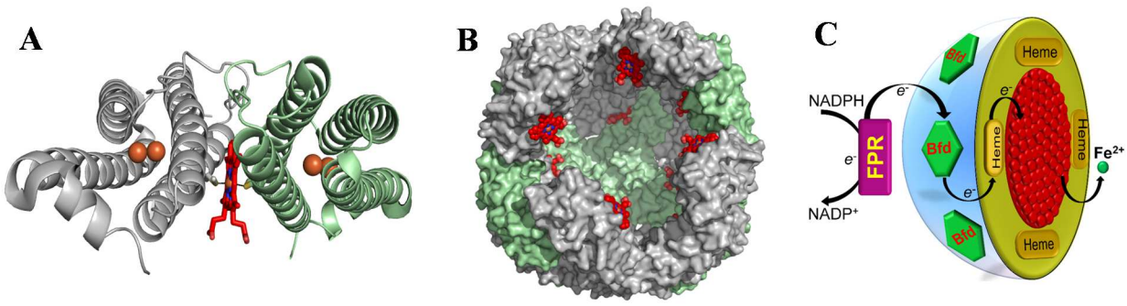

Figure 3-1 Structural organization of BfrB (PDB 3IS8) and its iron mobilization model. (A) View of subunit dimer harboring a heme molecule (red), which is coordinated by a conserved methionine in each of the subunits. (B) Inside view of the BfrB interior cavity where iron mineral is stored. Heme (red) is buried below the protein shell surface with the heme propionates extending into the cavity. (C) Proposed model of iron mobilization from BfrB central cavity, which is promoted by Bfd mediated electron transfer across the protein shell to reduce the Fe^{3+} mineral to Fe^{2+}.

More recently, we solved the X-ray crystal structure of the BfrB-Bfd complex [12]. The asymmetric unit cell contains three BfB subunit dimers, each associated with a Bfd molecule (Figure 3-2A), so that the biological assembly is a nearly spherical 24-mer BfrB with 12 Bfd molecules (Figure 3-2B). Each Bfd binds at an identical site on BfrB, at the interface of a subunit dimer, above each of the heme molecules, placing the [2Fe-2S] cluster of Bfd 15.1 Å

from the heme-iron in BfrB, which is buried within each subunit dimer (Figure 3-2A). Studies in solution demonstrated that formation of the BfrB-Bfd complex enables the heme in BfrB to conduct electrons from the [2Fe-2S] cluster in Bfd to the mineral core, thus accelerating reduction of the Fe^{3+} mineral core and mobilization of Fe^{2+} [12, 26]. A zoomed-in view of one of the 12 identical Bfd-binding sites on BfrB (Figure 3-2C) illustrates the proximity of the [2Fe-2S] cluster to the BfrB surface and shows the interactions that are likely important to stabilize the complex: (*i*) The side chain of Y2 in Bfd buries in a cleft on the BfrB surface, which is formed by the side chains of E81 in subunit A (E_A^{81}) and L68 in subunit B (L_B^{68}), (*ii*) the side chain of L5 in Bfd buries in a pocket formed mostly by L_B^{68}, N_B^{70}, L_B^{71}, and L_A^{77}, (*iii*) the backbone NH group of M1 forms H-bonds with carboxyl side chains in E_A^{85} and E_A^{81} on BfrB and its side chain interacts hydrophobically with L_A^{77} L_A^{78}, I_A^{79}, G_A^{80} and C_A^{89} on the BfrB surface, and (*iv*) the side chain of K40 in Bfd interacts hydrophobically with the side chain of K_A^{76} in BfrB and forms hydrogen bonds with carbonyl oxygen of BfrB Q_B^{72} and L_A^{74}.

In this study we examined the BfrB-Bfd interaction in solution with the aid of surface plasmon resonance (SPR) and isothermal titration calorimetry (ITC) and determined that the 12 Bfd-binding sites on BfrB, which are structurally identical, are also equivalent and independent. Bfd binds at each of the sites on BfrB with K_d of approximately 3 μM, and the interaction, although endothermic, is favored by a relatively large change in entropy. Having obtained a benchmark for the interaction between the two proteins, we mutated several residues participating at the interface to alanine. These experiments allowed us to understand how the different side chains contribute to the stability of the complex, and to determine that the cleft and pocket on BfrB where the side chains of Y2 and L5 bury to anchor Bfd are essential to the stability of the BfrB complex and to the Bfd-promoted mobilization of core iron from BfrB.

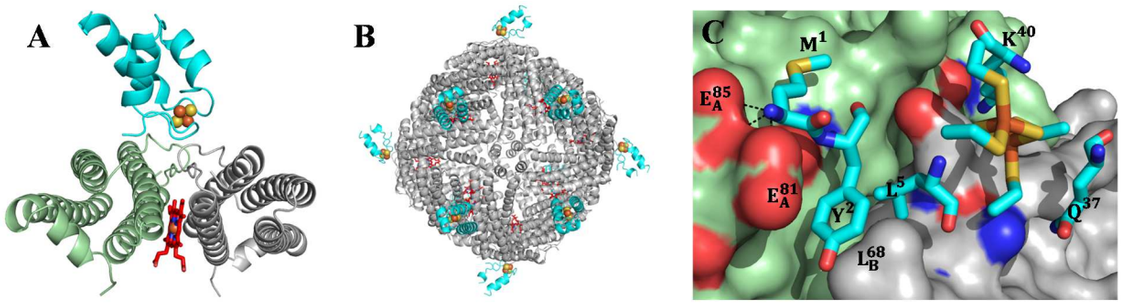

Figure 3-2 Structure of the BfrB-Bfd complex (PDB:4E6K). (A) View of a Bfd molecule (cyan) binding at the interface of a BfrB subunit dimer above the harbored heme molecule (red). (B) A 24-assembly BfrB binds 12 Bfd molecules. (C) View of the BfrB-Bfd interface. Bfd side chains (cyan) bury into binding clefts on the BfrB surface as well as form ionic interactions (dotted lines) with BfrB surface residues; BfrB subunit A and B are shown in green and gray respectively. O, N and S are shown in red, blue and yellow respectively.

Experimental Procedures

Site-Directed Mutagenesis

Mutations were introduced to the recombinant *bfrB* (L68A, E81A, E85A, L68A/E81A) and *bfd* (L5A, Y2F, Y2A, K40A) genes with the aid of the Quick Change mutagenesis kit (Stratagene, La Jolla, CA) using manufacturer instructions. Primer pair sequences are provided in Supporting Information. Mutations were confirmed by sequencing (ACGT Inc. Wheeling, IL). Plasmids carrying the desired mutations were transformed into *E. coli* Arctic express (DE3) RIL competent cells (Agilent Technologies, Santa Clara, CA).

Below listed the information of the primers for the mutations:

L68A: Forward: 5' CGTATTCTGTTTCTGGAAGGTGCGCCGAATCTGCAGGATCTGGG 3'

Reverse: 5' CCCAGATCCTGCAGATTCGGCGCACCTTCCAGAAACAGAATACG 3'

E81A: Forward: 5' GGGCAAACTGCTGATTGGTGCGAACACCCAGGAAATGCTGCAG 3'

Reverse: 5' CTGCAGCATTTCCTGGGTGTTCGCACCAATCAGCAGTTTGCCC 3'

E85A: Forward: 5 'GGTGAAAACACCCAGGCGATGCTGCAGTGCGATC 3'

Reverse: 5' GATCGCACTGCAGCATCGCCTGGGTGTTTTCACC 3'

Y2A: Forward: 5' GAAGGAGATATACATATGGCGGTGTGCCTGTGCCAGGG 3'

Reverse: 5' CCCTGGCACAGGCACACCGCCATATGTATATCTCCTTC 3'

Y2F: Forward: 5' GGAGATATACATATGTTTGTGTGCCTGTGCCAGG 3'

Reverse: 5' CCTGGCACAGGCACACAAACATATGTATATCTCC 3'

L5A: Forward: 5' CATATGTATGTGTGCGCGTGCCAGGGTGTGAC 3'

Reverse: 5' GTCACACCCTGGCACGCGCACACATACATATG 3’

K40A: Forward: 5' GCACCCAGTGCGGCGCGTGCGCAAGCCTGG 3'

Reverse: 5' CCAGGCTTGCGCACGCGCCGCACTGGGTGC 3'

***Protein Expression and Purification*.**

Recombinant BfrB (wild type and mutants) was expressed and purified using a previously reported protocol [29] with the following modifications: *E. coli* Arctic express RIL cells harboring the recombinant pET11a/*bfrB* construct were cultured overnight at 37 °C in 50

mL LB medium containing 100 μg/mL ampicillin and 20 μg/mL gentamicin. The cells were then cultured in 1L of fresh LB containing no antibiotics for 3 h at 30 °C, transferred to a shaker incubator pre- equilibrated at 10 °C and incubated for 45 min before protein expression was induced by addition of 1 mM 1-thio-D-galactopyranoside (IPTG). Cells were cultured for an additional 48 h at 10 °C before they were harvested by centrifugation and stored at -20 °C. To lyse the cells cell paste was suspended in a solution containing 50 mM Tris-Base (pH 7.6), 5 mM dithiothreitol (DTT), 0.5 mM phenylmethanesulfonylfluoride (PMSF) and 0.5% Triton™ X-100 (Sigma) and sonicated on ice. Cell debris were pelleted by centrifugation at 4 °C and 19,500 rpm and the supernatant was dialyzed against 50 mM Tris-Base (pH 7.6), then loaded onto a Q-Sepharose Fast Flow column (12 cm × 2.5 cm i.d.) equilibrated with the same buffer, and eluted with a gradient of 0 to 600 mM NaCl. Fractions containing BfrB were dialyzed against 50 mM potassium phosphate buffer (pH 7.6) containing 1 mM TCEP, loaded onto a hydroxyapatite Bio-Gel column (10 cm × 2.5 cm i.d.) equilibrated with the same buffer, and eluted with a 50 mM to 800 mM potassium phosphate gradient (pH 7.6), 1 mM TCEP. Isolating fractions containing BfrB and repeating this chromatographic step a second time yields pure BfrB. The separation of 24-mers from incompletely assembled protein was carried out by FPLC (AKTA GE Healthcare) in a Hiload™ 16/600 superdex™ 200 pg column equilibrated and eluted with 100 mM potassium phosphate (pH 7.0). BfrB purified in this manner is nearly devoid of heme. To reconstitute with heme, a previously described method [30] was used with some modifications: Hemin chloride was dissolved in 0.1 M sodium hydroxide solution, diluted with potassium phosphate buffer (100 mM, pH 7.0) to a final concentration of 1.5 mM. Insoluble material was removed by centrifugation. BfrB (3 μM) in 100 mM potassium phosphate (pH 7.0) and 1 M NaCl was equilibrated at 80 °C for 1 min in a dry bath (LabDoctor Dry Bath Plus), followed by the addition of a first aliquot of heme, which delivered 6 heme

molecules per 24-mer BfrB, and the mixture was incubated for 10 min at 80 °C. The temperature was then increased to 90 °C prior to addition of a second aliquot of heme delivering 6 heme molecules per 24-mer BfrB, followed by incubation at 90 °C for 10 min. The temperature was then increased to 95 °C prior to addition of a third aliquot of heme delivering 6 heme molecules per 24-mer, followed by incubation of the mixture at 95 °C for 10 min. The resultant mixture was cooled in ice, and loaded onto a Hiload^{TM} 16/600 superdex^{TM} 200 pg column equilibrated and eluted with 100 mM potassium phosphate (pH 7.6) at 4 °C. The desired fractions were collected and supplemented with 1 mM TCEP. The heme content of BfrB was analyzed according to a previously described method [31]. Reconstitution of BfrB with an iron core was carried out as reported previously [32]. Upon addition of 500 Fe ions/BfrB the protein solutions were incubated overnight at 4 °C and then passed through a superdex^{TM} 200 10/300 GL column using FPLC (AKTA) to separate them from non-incorporated iron. The content of iron in bacterioferritin, before and after reconstitution with an iron core, was measured using a previously reported protocol [29, 33].

BfrB Mutations Crystallization and Data Collection

All crystallization experiments were conducted in Compact Jr. (Emerald Biosystems) sitting drop vapor diffusion plates at 20 °C. Equal volumes of BfrB (10 mg/mL in 100 mM potassium phosphate, pH 7.6 and 1mM TCEP) and crystallization solution were equilibrated against 75 µL of crystallization solution at 20 °C. For BfrB E81A, crystals displaying a plate morphology were obtained in 1-2 days from the Wizard 3-4 screen (Rigaku Reagents) condition F12 (2.4 M sodium malonate) . For BfrB L68A, crystals displaying a prismatic morphology were obtained in 1-2 days from the Wizard 3-4 screen (Rigaku Reagents) condition E10 (50% (v/v) PEG 200, 100 mM Na cacodylate pH 6.5, 200 magnesium chloride). For BfrB E85A,

crystals displaying a plate morphology were obtained in 1-2 days from the Wizard 3-4 screen (Rigaku Reagents) condition F4 (15% (v/v) PEG 550MME, 100 mM MES pH 6.5). For L68A/E81A, prismatic crystals were obtained in 1-2 days from the Wizard 1 screen (Emerald Biosystems) condition D11 (1.26 M ammonium sulfate, 100 mM Tris pH 8.5, 200 mM lithum sulfate). Table 3-1 to 3-4 list crystallographic data for BfrB E81A, L68A, E81A/L68A and E85A respectively.

Table 3-1. Crystallographic data for BfrB E81A refined to 2.50 Å resolution.

	BfrB E81A
Data Collection	
Unit-cell parameters (Å, °)	*a*=128.48, *b*=186.34, *c*=200.68
Space group	$C222_1$
Resolution (Å)[1]	48.85-2.50 (2.55-2.50)
Wavelength (Å)	1.0000
Temperature (K)	100
Observed reflections	537,539
Unique reflections	83,211
$\langle I/\sigma(I)\rangle$[1]	10.6 (1.5)
Completeness (%)[1]	100 (100)
Multiplicity[1]	6.5 (5.5)
R_{merge} (%)[1, 2]	17.5 (116.8)
R_{meas} (%)[1, 4]	19.1 (129.6)
R_{pim} (%)[1, 4]	7.5 (55.4)
$CC_{1/2}$ [1, 5]	0.994 (0.589)
Refinement	
Resolution (Å)	46.79-2.50
Reflections (working/test)[6]	78,989/4,125
R_{factor} / R_{free} (%)[3]	16.5/23.0
No. of atoms (protein/heme/K^+/water)	15,110/301/3/282
Model Quality	
R.m.s deviations	
Bond lengths (Å)	0.010
Bond angles (°)	0.999
Average *B* factor (Å^2)	
All Atoms	37.5
Protein	37.5
Heme	44.3
K^+	20.8
Water	35.4
Coordinate error, maximum	0.33

likelihood (Å)	
Ramachandran Plot	
Most favored (%)	99.3
Additionally allowed (%)	0.7

5) Values in parenthesis are for the highest resolution shell.
6) $R_{merge} = \Sigma_{hkl}\Sigma_i |I_i(hkl) - \langle I(hkl)\rangle| / \Sigma_{hkl}\Sigma_i I_i(hkl)$, where $I_i(hkl)$ is the intensity measured for the ith reflection and $\langle I(hkl)\rangle$ is the average intensity of all reflections with indices hkl.
7) $R_{factor} = \Sigma_{hkl} ||F_{obs}(hkl)| - |F_{calc}(hkl)|| / \Sigma_{hkl} |F_{obs}(hkl)|$; Rfree is calculated in an identical manner using 5% of randomly selected reflections that were not included in the refinement.
8) R_{meas} = redundancy-independent (multiplicity-weighted) R_{merge}[34, 35]. R_{pim} = precision indicating (multiplicity-weighted) R_{merge}[36, 37].
9) $CC_{1/2}$ is the correlation coefficient of the mean intensities between two random half-sets of data [38, 39].
10) Friedel pairs were treated as independent reflections for refinement of the anomalous scattering atoms. Therefore, the number of working reflections in refinement is greater than the number of unique reflections observed during data scaling.

Table 3-2. Crystallographic data for BfrB L68A refined to 2.20 Å resolution.

	BfrB L68A
Data Collection	
Unit-cell parameters (Å, °)	a=117.86 Å, b=169.99 Å, c=125.66 Å
Space group	$P2_12_12$
Resolution (Å)[1]	48.43-2.20 (2.24-2.20)
Wavelength (Å)	1.0000
Temperature (K)	100
Observed reflections	869,801
Unique reflections	126,857
$\langle I/\sigma(I)\rangle$[1]	10.7 (2.1)
Completeness (%)[1]	99.0 (98.3)
Multiplicity[1]	6.9 (7.1)
R_{merge} (%)[1, 2]	15.3 (121.2)
R_{meas} (%)[1, 4]	16.5 (130.6)
R_{pim} (%)[1, 4]	6.3 (48.5)
$CC_{1/2}$ [1, 5]	0.997 (0.772)
Refinement	
Resolution (Å)	48.43-2.20
Reflections (working/test)[6]	244,942/12,163
R_{factor} / R_{free} (%)[3]	20.2/26.3
No. of atoms	15,099/301/3/12/669

(protein/heme/Arsenic/Mg^{2+}/water)	
Model Quality	
R.m.s deviations	
Bond lengths (Å)	0.012
Bond angles (°)	1.134
Average *B* factor (Å^2)	
All Atoms	39.0
Protein	38.9
Heme	45.0
Arsenic	27.0
Mg^{2+}	42.3
Water	38.5
Coordinate error, maximum likelihood (Å)	0.33
Ramachandran Plot	
Most favored (%)	97.5
Additionally allowed (%)	2.3

1) Values in parenthesis are for the highest resolution shell.
2) $R_{merge} = \Sigma_{hkl}\Sigma_i |I_i(hkl) - \langle I(hkl)\rangle| / \Sigma_{hkl}\Sigma_i I_i(hkl)$, where $I_i(hkl)$ is the intensity measured for the *i*th reflection and $\langle I(hkl)\rangle$ is the average intensity of all reflections with indices hkl.
3) $R_{factor} = \Sigma_{hkl} ||F_{obs}(hkl)| - |F_{calc}(hkl)|| / \Sigma_{hkl} |F_{obs}(hkl)|$; Rfree is calculated in an identical manner using 5% of randomly selected reflections that were not included in the refinement.
4) R_{meas} = redundancy-independent (multiplicity-weighted) R_{merge}[34, 35]. R_{pim} = precision-indicating (multiplicity-weighted) R_{merge}[36, 37].
5) $CC_{1/2}$ is the correlation coefficient of the mean intensities between two random half-sets of data [38, 39].

Table 3-3. Crystallographic data for BfrB E85A refined to 2.55 Å resolution.

	BfrB E85A
Data Collection	
Unit-cell parameters (Å, °)	a=b=205.56, c=115.77
Space group	$P4_22_12$
Resolution (Å)[1]	48.98-2.55 (2.60-2.55)
Wavelength (Å)	1.0000
Temperature (K)	100
Observed reflections	733,536
Unique reflections	80,992
$\langle I/\sigma(I)\rangle$[1]	10.3 (1.7)
Completeness (%)[1]	100 (100)
Multiplicity[1]	9.1 (9.4)

R_{merge} (%)[1, 2]	21.5 (143.5)
R_{meas} (%)[1, 4]	22.7 (151.9)
R_{pim} (%)[1, 4]	7.5 (49.5)
$CC_{1/2}$ [1, 5]	0.994 (0.620)
Refinement	
Resolution (Å)	42.72-2.55
Reflections (working/test)[6]	76,947/3,978
R_{factor} / R_{free} (%)[3]	18.0/26.1
No. of atoms (protein/heme/K^+/water)	14,997/301/3/361
Model Quality	
R.m.s deviations	
Bond lengths (Å)	0.010
Bond angles (°)	1.018
Average *B* factor (Å^2)	
All Atoms	40.1
Protein	40.3
Heme	38.7
K^+	29.4
Water	35.2
Coordinate error, maximum likelihood (Å)	0.39
Ramachandran Plot	
Most favored (%)	97.8
Additionally allowed (%)	2.0

1) Values in parenthesis are for the highest resolution shell.
2) $R_{merge} = \Sigma_{hkl}\Sigma_i |I_i(hkl) - \langle I(hkl)\rangle| / \Sigma_{hkl}\Sigma_i I_i(hkl)$, where $I_i(hkl)$ is the intensity measured for the *i*th reflection and $\langle I(hkl)\rangle$ is the average intensity of all reflections with indices hkl.
3) $R_{factor} = \Sigma_{hkl} ||F_{obs}(hkl)| - |F_{calc}(hkl)|| / \Sigma_{hkl} |F_{obs}(hkl)|$; Rfree is calculated in an identical manner using 5% of randomly selected reflections that were not included in the refinement.
4) R_{meas} = redundancy-independent (multiplicity-weighted) R_{merge}[34, 35]. R_{pim} = precision-indicating (multiplicity-weighted) R_{merge}[36, 37].
5) $CC_{1/2}$ is the correlation coefficient of the mean intensities between two random half-sets of data [38, 39].
6) Friedel pairs were treated as independent reflections for refinement of the anomalous scattering atoms. Therefore, the number of working reflections in refinement is greater than the number of unique reflections observed during data scaling.

Table 3-4. Crystallographic data for BfrB L68A/ E81A refined to 1.60 Å resolution.

	BfrB L68A E81A
Data Collection	
Unit-cell parameters (Å, º)	*a*=182.2, *c*=128.5
Space group	*H*3
Resolution (Å)[1]	48.82-1.60 (1.63-1.60)
Wavelength (Å)	1.0000
Temperature (K)	100
Observed reflections	1,057,867
Unique reflections	209,085
$\langle I/\sigma(I)\rangle$[1]	10.4 (2.5)
Completeness (%)[1]	99.7 (100)
Multiplicity[1]	5.1 (5.1)
R_{merge} (%)[1, 2]	9.7 (63.4)
R_{meas} (%)[1, 4]	10.9 (70.8)
R_{pim} (%)[1, 4]	4.8 (31.3)
$CC_{1/2}$ [1, 5]	0.995 (0.753)
Refinement	
Resolution (Å)	34.84-1.60
Reflections (working/test)	198,565 / 10,492
R_{factor} / R_{free} (%)[3]	17.6 / 20.1
No. of atoms (protein/heme/K^+/sulfate/water)	10,079/172/2/21/1060
Model Quality	
R.m.s deviations	
Bond lengths (Å)	0.008
Bond angles (º)	0.915
Average *B* factor (Å^2)	
All Atoms	18.9
Protein	17.9
Heme	16.4
K^+	29.5
sulfate	41.9
Water	28.2
Coordinate error, maximum likelihood (Å)	0.16
Ramachandran Plot	
Most favored (%)	100
Additionally allowed (%)	-

1) Values in parenthesis are for the highest resolution shell.
2) $R_{merge} = \Sigma_{hkl}\Sigma_i |I_i(hkl) - \langle I(hkl)\rangle| / \Sigma_{hkl}\Sigma_i I_i(hkl)$, where $I_i(hkl)$ is the intensity measured for the *i*th reflection and $\langle I(hkl)\rangle$ is the average intensity of all reflections with indices hkl.

3) $R_{factor} = \Sigma_{hkl} ||F_{obs}(hkl)| - |F_{calc}(hkl)|| / \Sigma_{hkl} |F_{obs}(hkl)|$; Rfree is calculated in an identical manner using 5% of randomly selected reflections that were not included in the refinement.
4) R_{meas} = redundancy-independent (multiplicity-weighted) R_{merge}[34, 35]. R_{pim} = precision-indicating (multiplicity-weighted) R_{merge}[36, 37]. $CC_{1/2}$ is the correlation coefficient of the mean intensities between two random half-sets of data [38, 39].

Measurement of the BfrB-Bfd Binding Affinity by Surface Plasmon Resonance (SPR).

SPR experiments were performed at 22 °C using a Biacore 3000 instrument (GE Healthcare). BfrB was immobilized on a CM5 sensor chip using amine coupling methodology [40]: The sensor chip surface was pre-conditioned with 50 mM NaOH, 10 mM HCl, 0.1% SDS and 0.085% H_3PO_4 and activated by injecting 0.1 M N-hydroxysuccinimide (NHS) and 0.4 M 1-ethyl-3-(3-dimethylaminopropyl) carbodiimide (EDC) in water. The running buffer was PBS with 1.5 mM TCEP, pH 7.4. Immobilization of BfrB was carried out by flowing (10 µL/min) a 100 nM solution of BfrB in 10 mM sodium acetate buffer (pH 5.0) for 32.5 min, followed by quenching surface-activated sites not coupled to BfrB by flowing (10 µL/min) 1.0 M aqueous ethanolamine-HCl (pH 8.5) for 7 min. A cell activated by NHS/EDC and quenched by ethanolamine but not containing BfrB was used as the reference surface, and a cell immobilized with bovine serum albumin (BSA) was used as control. To determine the BfrB/Bfd binding affinity, a solution of Bfd in 50 mM potassium phosphate (pH 7.0), 150 mM NaCl, 5 mM DTT was simultaneously flown (25 µL/min) over the cell containing immobilized BfrB, the reference cell, and the cell containing immobilized BSA at 25 µL/min. Bfd solutions with the following concentrations were used to construct a binding curve: 0.5 µM, 1 µM, 2 µM, 5 µM, 10 µM, 20 µM, and 40 µM. The corresponding responses were double-referenced by subtracting the bulk refractive index change caused by difference in buffer compositions, as well as by subtracting the response from the reference cell. Experiments were conducted in triplicate.

Measurement of the BfrB-Bfd Binding Affinity by Isothermal Titration Calorimetry (ITC)

Prior to each experiment, BfrB and Bfd were exchanged into 100 mM potassium phosphate buffer (pH 7.0), 150 mM NaCl, and 1 mM TCEP by passage through a superdex^{TM} 200 10/300 GL, or superdex^{TM} 75 10/300 GL column, respectively. ITC was performed at 22 °C using a MicroCal auto ITC instrument (GE Healthcare). The cell was loaded with 1.45 mL of 18 μM Bfd, and titrated with a total volume of 0.25 mL of 20 μM BfrB in 25 injections, each lasting 20 s and delivering 10.02 μL, with 300 s between injections. A similar titration of BfrB into buffer served as control to measure the heat of dilution. The experiments were repeated three times.

Mobilization of iron from BfrB

These experiments were carried out in an anaerobic chamber according to a previously described method [29] with small modifications: A 1 cm path-length cuvette was filled with a solution consisting of BfrB (0.18 μM) reconstituted with 500 ± 20 Fe^{3+} ions/BfrB, Bfd (0.9 μM), FPR (7.2 μM) and α,α'- bipyridine (bipy), 3 mM. The reactions leading to mobilization of Fe^{2+} from BfrB were initiated by addition of 1 mM NADPH, and the process was monitored by tracking the time-dependent formation of the $[Fe(bipy)_3]^{2+}$complex, which absorbs at 523 nm. The percentage of iron released was calculated by normalizing the intensity of the 523 nm band to the intensity expected upon mobilization of the 500 iron ions stored in BfrB.

RESULTS

Characterization of the BfrB-Bfd Interaction by SPR

The X-ray crystal structure of the BfrB-Bfd complex showed that each Bfd binds at the interface of a BfrB subunit, near the two-fold axis of symmetry, placing the [2Fe-2S] cluster of Bfd approximately 15.1 Å from the heme in BfrB. Studies in solution showed that Bfd binding to BfrB makes the BfrB-heme conductive, accelerates reduction of the Fe^{3+} mineral core and facilitates mobilization of Fe^{2+} [29, 41]. As part of the study reported herein, we investigated the binding affinity of the BfrB-Bfd complex using SPR. Figure 3-3A shows the reference- and baseline-subtracted responses obtained from flowing Bfd over BfrB immobilized on a sensor chip. At each Bfd concentration the corresponding response reaches a plateau, indicating steady state equilibrium. Plotting each response at the steady state as a function of Bfd concentration results in the hyperbolic binding curve defined by the black circles in Figure 3-3B. The interpretive model used to fit these data is described below.

In SPR experiments BfrB is immobilized on the surface and free Bfd is in the flow. Hence, [$BfrB_f$] is the concentration of immobilized BfrB not bound to Bfd, [Bfd_f] is the concentration of Bfd in the flowing solution, which is maintained constant by the flow system, and [*BfrB-Bfd*] is the concentration of the protein complex at the surface. For a case where Bfd binding is homogeneous and the stoichiometry is 1:1, the expression for the dissociation constant (K_d) can be written as in equation 1, where the total concentration of immobiled BfrB is given by [$BfrB_t$] = [$BfrB_f$] + [*BfrB-Bfd*].

$$\frac{[BfrB - Bfd]}{[BfrB_t]} = \frac{[Bfd_f]}{K_d + [Bfd_f]} \quad (1)$$

Since the X-ray crystal structure showed that Bfd binds to multiple sites on BfrB, equation (1) was modified to expression (2), which indicates that *n* sites in BfrB can be occupied by Bfd, with corresponding dissociation constants.

$$[BfrB - Bfd] = [BfrB - Bfd_1] + [BfrB - Bfd_2] + \cdots + [BfrB - Bfd_n]$$

$$= \frac{[BfrB_t][Bfd_f]}{K_{d1} + [Bfd_f]} + \frac{[BfrB_t][Bfd_f]}{K_{d2} + [Bfd_f]} + \cdots$$

$$+ \frac{[BfrB_t][Bfd_f]}{K_{dn} + [Bfd_f]} \qquad (2)$$

The X-ray crystal structure of the BfrB-Bfd complex showed that up to 12 Bfd molecules can bind to 12 identical binding sites on BfrB. Thus, assuming that the 12 Bfd binding sites on BfrB are identical and non-interacting, expression 2 can be reduced to equation 3 [42], which is similar to equation 1, except for the inclusion of the complex stoichiometry, *n*.

$$[BfrB - Bfd] = \frac{n[BfrB_t][Bfd_f]}{K_d + [Bfd_f]} \qquad (3)$$

At each of the Bfd concentrations ($[Bfd_f]$) used to obtain the sensograms in Figure 3-3A, when the system reaches steady state equilibrium (plateau) the concentration of the BfrB-Bfd complex at the surface is proportional to the magnitude of the SPR response at the pleateau, which is termed $R_{eq.}$ Hence, equation 3 can be re-written as equation 4, where R_0, corresponds to the response when every immobilized BfrB molecule is bound by one Bfd molecule, and the remainder terms are defined as above.

$$R_{eq} = \frac{nR_0[Bfd_f]}{K_d + [Bfd_f]} \qquad (4)$$

$$R_0 = \frac{MW_{Bfd}}{MW_{BfrB}} \times R_{immo} \quad (5)$$

Setting initial values of n = 12 and R_0 = 520 ± 18, respectively, and fitting the values of R_{eq} obtained at each [Bfd_f] (circles in the plot of Figure 3-3B) to equation 4, a K_d value 3.3 ± 0.5 µM (Table 3- 5), n = 12.7 and R_0 = 624 ± 18 were obtained. The initial value of R_0 was calculated from equation 5 [43], where R_{immo} is the SPR response obtained upon immobilizing BfrB, MW_{BfrB} is the molecular mass of BfrB (452,672 Da) and MW_{Bfd} is the molecular mass of Bfd (7,984 Da). As can be seen from the fitted line in Figure 3-3B and from the small residuals, the binding curve is well fitted by equation 4. In addition, the linear behavior observed from analysis of the binding curve by the Scatchard plot, which is a powerful tool for identifying deviations from simple binding models [42, 44], supports the idea implicit in equation 4, that the 12 binding sites in BfrB are equivalent and independent.

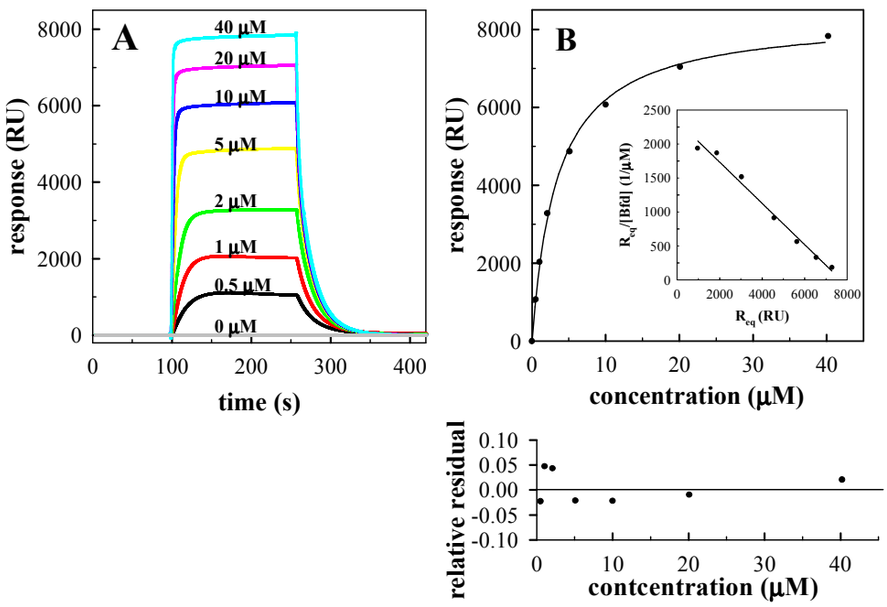

Figure 3-3 Measuring the affinity of the BfrB-Bfd interaction using SPR. (A) Overlay of double referenced sensorgrams resulting from the injection of different concentrations of Bfd

(0~40 μM) over immobilized BfrB. (B) The BfrB-Bfd binding affinity determined by steady state affinity analysis. Responses at steady state are plotted as a function of Bfd concentrations (black circles in the top panel) and fitted to the 1:1 Langmuir model (solid line). The scatchard plot is shown in the inset. The residuals plotted in the bottom panel shows the relative response difference between the generated fit and the experimental data.

Table 3-5. Thermodynamics and kinetics of the BfrB-Bfd Binding[a]

	K_d (μM)	k_{on} ($\mu M^{-1}s^{-1}$)	k_{off} (s^{-1})	ΔH (kcal/mol)	ΔS (cal/(mol.K))[c]	ΔG (kcal/mol)[b]
SPR steady state analysis	3.0 ± 0.5	_	_	_	_	_
SPR kinetic analysis	2.6 ± 0.4	0.026 ± 0.002	0.069 ± 0.01	_	_	_
ITC analysis	4.0 ± 0.7	_	_	1.6 ±0.3	30.1 ± 0.7	-7.3 ± 0.1

[a] The reported thermodynamic and kinetic parameters obtained from triplicate experiments.

[b] Calculated from $\Delta G = -RTln\ (1/K_d)$

[c] Calculated from $\Delta S = (\Delta H - \Delta G)/T$

Having shown that the 12 binding sites on a BfrB molecule are identical and independent, kinetic analysis of the BfrB-Bfd interaction was carried out assuming the 1:1 binding model described by equations 6 and 7, where $BfrB_s$ indicates one of the 12 binding sites in each immobilized BfrB molecule, $[BfrB_{ts}]$ is the total concentration of binding sites (12/BfrB molecule) on the surface, $[BfrB_{bs}]$ is the concenration of BfrB sites bound to Bfd, k_a is the association rate constant, and k_d is the dissociation rate constant. Equation 7 can be re-written in terms of the SPR response as equation 8, where R is the response caused by Bfd binding and R_{max} is the response when all the binding sites are occupied by Bfd [45]. Hence, values of k_a and

k_d (Table 3-5) were obtained from global fitting of the SPR data to equation 8 (Figure 3-4A) with the aid of BIAevaluation software. Note that the ratio of the constants (k_a/k_d) is very similar to the value of K_d obtained from steady state analysis described above, an observation that strengthens the conclusion that the Bfd binding sites on BfrB are independent and equivalent.

$$BfrB_s + Bfd \underset{k_{off}}{\overset{k_{on}}{\rightleftarrows}} BfrB_s - Bfd \tag{6}$$

$$\frac{d[BfrB_{bs}]}{dt} = k_a([BfrB_{ts}] - [BfrB_{bs}])[Bfd_f] - k_d[BfrB_{bs}] \tag{7}$$

$$\frac{dR}{dt} = k_a(R_{max} - R)[Bfd_f] - k_dR \tag{8}$$

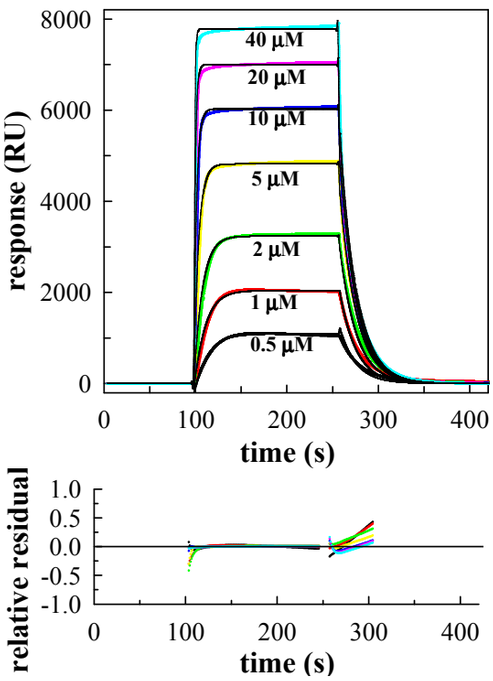

Figure 3-4. Kinetic analysis of the BfrB-Bfd interaction. Top panel: fits generated (black lines) by globally fitting the rate equations derived from the 1:1 Langmuir model to the association and dissociation phases of all seven injections simultaneously. Bottom panel: the relative residual errors from the fits.

Characterization of the BfrB-Bfd interaction in solution by ITC

The interaction between BfrB and Bfd was also studied by ITC. The top panel in Figure 3-5 shows the binding isotherms obtained from titrating Bfd with BfrB, which show that formation of the BfrB-Bfd complex is an endothermic process. The ITC data were integrated, normalized for nonspecific heat effects, and fitted using a non-linear least square algorithm (minimization of χ^2) with the aid of the Origin software package provided by MicroCal. Since the 12 binding sites on BfrB are equivalent and independent, the data was fitted to the 1:1 binding model described by equation 6, where the concentration of titrant (BfrB) is the concentration of Bfd-binding sites. Fitting the integrated (bottom panel in Figure 3-5) allowed us to obtain the ΔH, ΔS, and K_d values listed in Table 3-5, which indicate that the BfrB-Bfd association is entropically driven. Note that the value of K_d obtained from these measurements is also in good agreement with the K_d values obtained from the SPR experiments, thus providing additional support for the idea that the 12 Bfd-binding sites in BfrB are identical and independent.

Below is the deduction of the equations. According to equation (6), at equilibrium,

$$\frac{[BfrB_{fs}][Bfd_f]}{[BfrB_s - Bfd]} = K_D = \frac{1}{K_A} \tag{9}$$

Where [$BfrB_{fs}$] represents free binding sites on BfrB. Equation (9) can be rewritten as:

$$\frac{[BfrB_s - Bfd]}{[Bfd_t]} = \frac{[BfrB_{fs}]}{K_D + [BfrB_{fs}]} \tag{10}$$

Where [Bfd_t] is the initial total concentration of Bfd in the cell and equals to [Bfd_f]+[$BfrB_s$:Bfd]

Equation (10) can be rewritten as:

$$K_A = \frac{1}{K_D} = \frac{\theta}{(1-\theta)[BfrB_{fs}]} \tag{11}$$

Where θ is the fraction of Bfd bound by protein BfrB binding sites.

$$[BfrB_{ts}] = [BfrB_{fs}] + n\theta[Bfd_t\ ] \tag{12}$$

Where [$BfrB_{ts}$] is the total concentration of protein BfrB binding sites, and n is the number of binding sites on Bfd. In this case, n=1. Combining equation (11) and (12) gives:

$$\theta^2 - \theta\left[1 + \frac{[BfrB_{ts}]}{[Bfd_t]} + \frac{1}{[Bfd_t]K_A}\right] + \frac{[BfrB_{ts}]}{[Bfd_t]} = 0 \tag{13}$$

At the beginning of the reaction, the working cell is filled with protein Bfd and the volume of the working cell is V_0. The working cell is sensed calorimetrically. As BfrB is titrated to the cell, the increase of the total volume is ΔV. Because of the total-fill nature of the working cell, the increased volume is pushed into the inactive tube.

Therefore, the heat evolved during the titration process in the working cell is:

$$Q = \theta[BfrB_{ts}]\Delta H V_0 \tag{14}$$

Where ΔH is the molar enthalpy change of the binding. Therefore, the equation (14) can be rewritten as:

$$Q = \frac{[BfrB_{ts}]\,\Delta HV_0\left\{1+\frac{[BfrB_{ts}]}{[Bfd_t]}+\frac{1}{K_A[Bfd_t]}-\left[\left(1+\frac{[BfrB_{ts}]}{[Bfd_t]}+\frac{1}{K_A[Bfd_t]}\right)^2-\frac{4[BfrB_{ts}]}{[Bfd_t]}\right]^{\frac{1}{2}}\right\}12}{2} \quad (15)$$

After the i[th] titration, the heat evolved is called *Q(i)*. Since the parameter being measured is the heat change upon each injection, therefore, the heat change caused by the i[th] injection is:

$$\Delta Q(i) = Q(i) - Q(i-1) \quad (16)$$

However, the equation (16) assume the total bulk protein concentration of [$BfrB_{ts}$] and [Bfd_t] remain the same as the initial value by supposing the reaction volume remains V_0, not considering the added volume of ΔV will cause a dilution of [$BfrB_{ts}$] and [Bfd_t]. But in reality, although the volume of the working cell sensed calorimetrically remains V_0, the real reaction volume is $V_0+\Delta V$. For a certain addition (i[th] addition), a volume of ΔV_i will be pushed out from the working cell into the inactive tube due to the i[th] addition. However, this part of the solution still contributes to the heat effect before it is passed out the working cell. The heat effect caused by the displaced volume will contribute about 50% of the heat effect of an equal volume inside the working cell, therefore, the equation (16) needs to be modified with the correction factor for displaced volume

$$\Delta Q(i) = Q(i) - Q(i-1) + \frac{\Delta V_i}{V_0}\left[\frac{Q(i)+Q(i-1)}{2}\right] \quad (17)$$

Where $\frac{\Delta V_i}{V_0}\left[\frac{Q(i)+Q(i-1)}{2}\right]$ is the correction factor for the displaced volume.

The data was fitted using Origin® scientific plotting software. The fitting process involves initial guess of parameters *n,* K_A and ΔH, followed by calculation of $\Delta Q(i)$. $\Delta Q(i)$ is compared with

experimental measured value of evolved heat caused by its corresponding injection. Standard Marquardt method is used for the fitting to improve the obtained values of *n,* K_A and ΔH. The process is repeated until no further significant improvement in the fitting can be obtained.

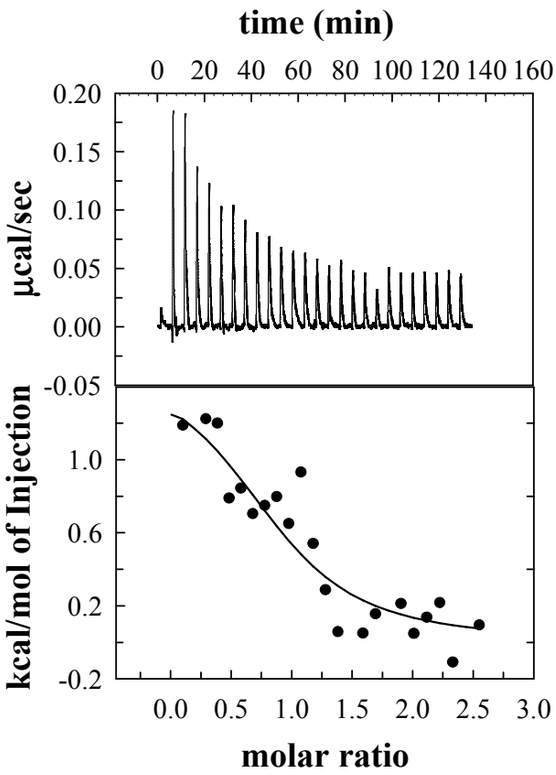

Figure 3-5. ITC characterization of the BfrB-Bfd interaction. The top panel shows the raw ITC data and the bottom panel shows the plot of integrated area under each titration peak (black circle) fitted to the 1:1 Langmuir binding model (solid line).

Dissecting the Interacting Surface of the BfrB-Bfd Complex.

The structure of the BfrB-Bfd complex shows that L68, E81 and E85 in BfrB interact with M1, Y2 and L5 in Bfd (see Figure 3-2C), forming a contiguous set of interactions that is likely to contribute significantly to the stability of the complex. To study the relative

contribution of these interactions to the formation of the complex, we prepared the L68A, E81A, E85A, L68A/E81A mutants of BfrB, and the Y2A, Y2F, L5A and K40A mutants of Bfd. It has been shown that in BfrB, breathing motions of the protein shell link relatively distant sections in the structure, and that for example, mutations in some of the pores can affect the reactivity of relatively distant ferroxidase centers.[9] The main objective of the mutations introduced in BfrB for this study is to determine their effect on the stability of the BfrB-Bfd interaction and inhibition of mobilization of core iron stored in the bacterioferritin. Consequently, we characterized the BfrB mutants to determine that the mutations, which were designed to affect only the BfrB interaction, did not cause significant changes in the structure of the protein, or its ability to oxidize Fe^{2+} and store Fe^{3+}. The biochemical characterization is described immediately below, and the structural analysis is presented later.

Biochemical characterization of BfrB mutants

The ability of the mutant proteins to assemble into 24-mers was analyzed with the aid of a calibrated size exclusion column. The results show that retention volumes exhibited by all the mutants are nearly identical to the retention volume displayed by wild type BfrB (Figure 3-6), indicating that all mutants assemble into 24-mers. The UV-vis absorption spectrum displayed by each of the BfrB mutants is identical to that of wt BfrB (Figure 3-7): The heme in the oxidized form gives rise to a Soret band at 418 nm, whereas in its reduced form the Soret band is at 425 nm with peaks in the visible at 527 and 567 nm. In wt BfrB, the ratio $A_{280}/A_{418} = 0.67$ is indicative of a 24-mer protein harboring 12 heme molecules [29]. In the UV-vis spectra obtained from each of the BfrB mutants the A_{280}/A_{418} ratio is also ≈ 0.67, indicating that the mutants also harbor 12 hemes in a 24-mer assembly. This conclusion is also supported by analysis of heme content.

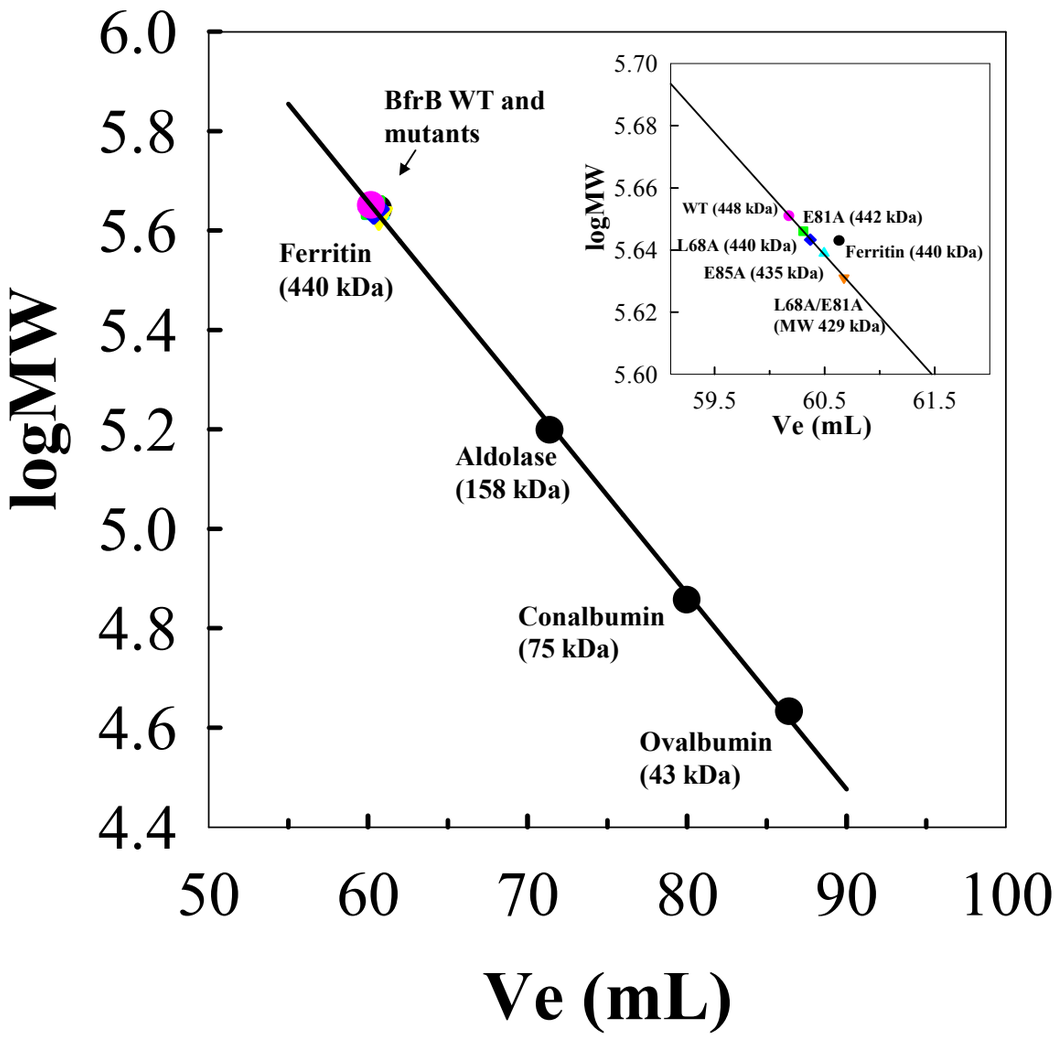

Figure 3-6 Elution volumes (Ve) of the BfrB mutants from a calibrated Superdex 200 column. BfrB wild type (magenta) 60.2 mL; BfrB L68A 60.4 mL (blue); BfrB E81A (green) 60.3 mL; BfrB E85A (cyan) 60.5 mL; BfrB L68A/E81A (orange) 60.7 mL. Inset: A zoomed-in view of the elution volumes of the BfrB WT and mutants with calibrated molecular weight.

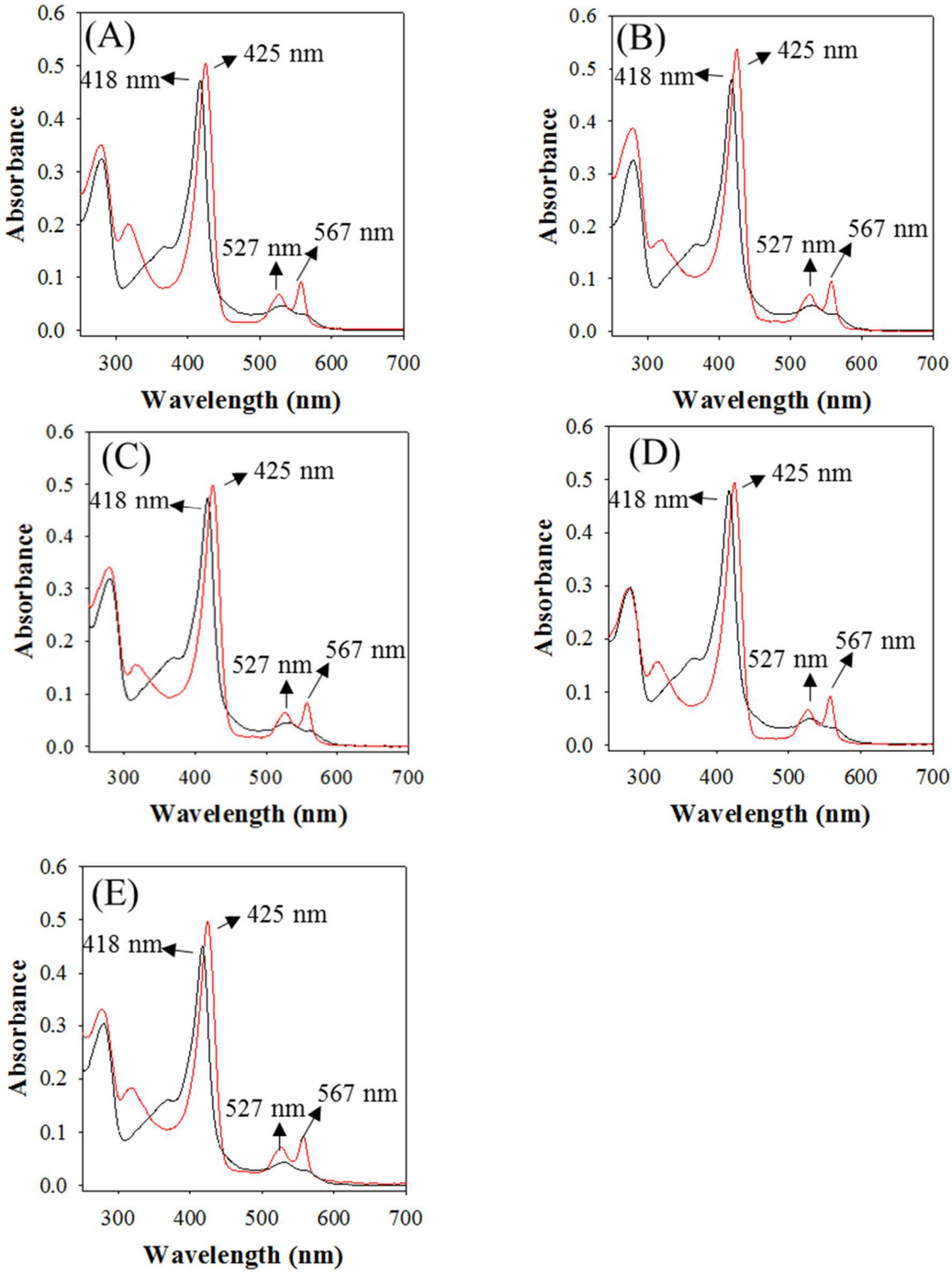

Figure 3-7 Oxidized (black) and reduced (red) spectra of (A) BfrB WT, (B) L68A, (C) E81A, (D) E85A and (E) L68A/E81A.

The iron oxidation and uptake function of each mutant was evaluated by reconstituting each of the proteins with 500 iron ions, while monitoring the process with the aid of UV-vis spectrophotometry, as described previously for wt BfrB [26, 27]. The spectral families (Figure 3-8) obtained from titrating a solution of BfrB with aliquots delivering 50 Fe^{2+} ions /BfrB show a gradual increase in the absorption at 300 nm, which is associated with the growth of ferric mineral in the core of ferritin-like molecules [29]. After addition of 500 Fe ions/BfrB the solution was incubated overnight at 4 °C and then passed through a Sephadex G-25 column. Subsequent determination of iron content in BfrB showed that each of the proteins captured >450 Fe ions/BfrB. Having determined that the BfrB mutants assemble into 24-mer molecules that are fully functional to oxidize Fe^{2+} and store Fe^{3+} in their core, the effect of the mutations on the ability of Bfd to bind BfrB mutants and promote the mobilization of core iron was examined, and the results are presented below.

Mobilization of core iron from the BfrB mutants is compromised

We have previously demonstrated that mobilization of iron stored in BfrB requires Bfd [12, 26]. The process of iron mobilization involves Bfd binding to BfrB, which permits electron transfer from the [2Fe-2S] cluster in Bfd to the core iron in BfrB via its heme. Consequently, to determine the effect of the BfrB mutations on the ability of Bfd to bind and promote the mobilization of iron we reconstituted wt and each of the BfrB mutants with 500 ± 20 iron ions in their core. The mobilization of iron was monitored by UV-vis in a cuvette containing the appropriate mixture of proteins and excess bipy, a Fe^{2+} chelator. Addition of excess NADPH initiates the reactions and the release of Fe^{2+} from BfrB is monitored by ΔA_{523}, which tracks the time-dependent formation of the $[Fe(bipy)_3]^{2+}$ complex. The black circles in Figure 3-9A track ΔA_{523} normalized to the total absorbance change expected on removal of the 500 iron ions in the

wt BfrB core, following addition of excess NADPH to a solution containing wt BfrB, FPR and Bfd. In comparison, the red circles track ΔA_{523} on addition of NADPH to a mixture containing only wt BfrB and FPR. Clearly, Bfd is necessary for the efficient and quantitative mobilization of Fe^{2+}. Similar experiments conducted with the BfrB mutants show that the mutations significantly decrease the efficiency of iron mobilization from BfrB: Replacement of Leu68, Glu81, or Glu85 for Ala causes significant decrease in the rate of iron release from BfrB, as shown by the cyan, green and orange traces in Figure 3-9A, and iron release from the Leu68Ala/Glu81Ala double mutant is nearly completely abolished, as shown by the blue trace.

The accompanying plots in Figure 3-9B track the time-dependent shift of the Soret band from 418 nm (oxidized heme) to 425 nm (reduced heme). In the case of wt BfrB, as the reaction progresses and the ferric mineral core has been ≈ 80% mobilized, the heme is completely reduced, indicating that the flux of electron transfer from Bfd to heme in BfrB is faster than electron transfer from the heme to the diminished ferric core. In stark contrast, in the case of the E81A/L68A BfrB mutant, the ferric core is not mobilized (Figure 3-9A), and the Soret band remains at 417 nm, an observation that is consistent with the idea that E81A/L68A BfrB cannot form productive interactions with Bfd, thus inhibiting electron transfer between the [2Fe-2S] cluster in Bfd and heme in BfrB. When L68A, E81A or E85A are present in the reaction vessel, the corresponding ferric cores are mobilized more slowly than that in wt BfrB, and the steady state of reduced heme accumulates more gradually, but it does not reach complete reduction in the 60 min that the reactions were monitored. Together, the observations summarized in Figure 3-9 indicate that the BfrB single mutants undergo productive interactions with Bfd less frequently than wt BfrB, and that productive interactions between E81A/L68A BfrB and Bfd are extremely rare.

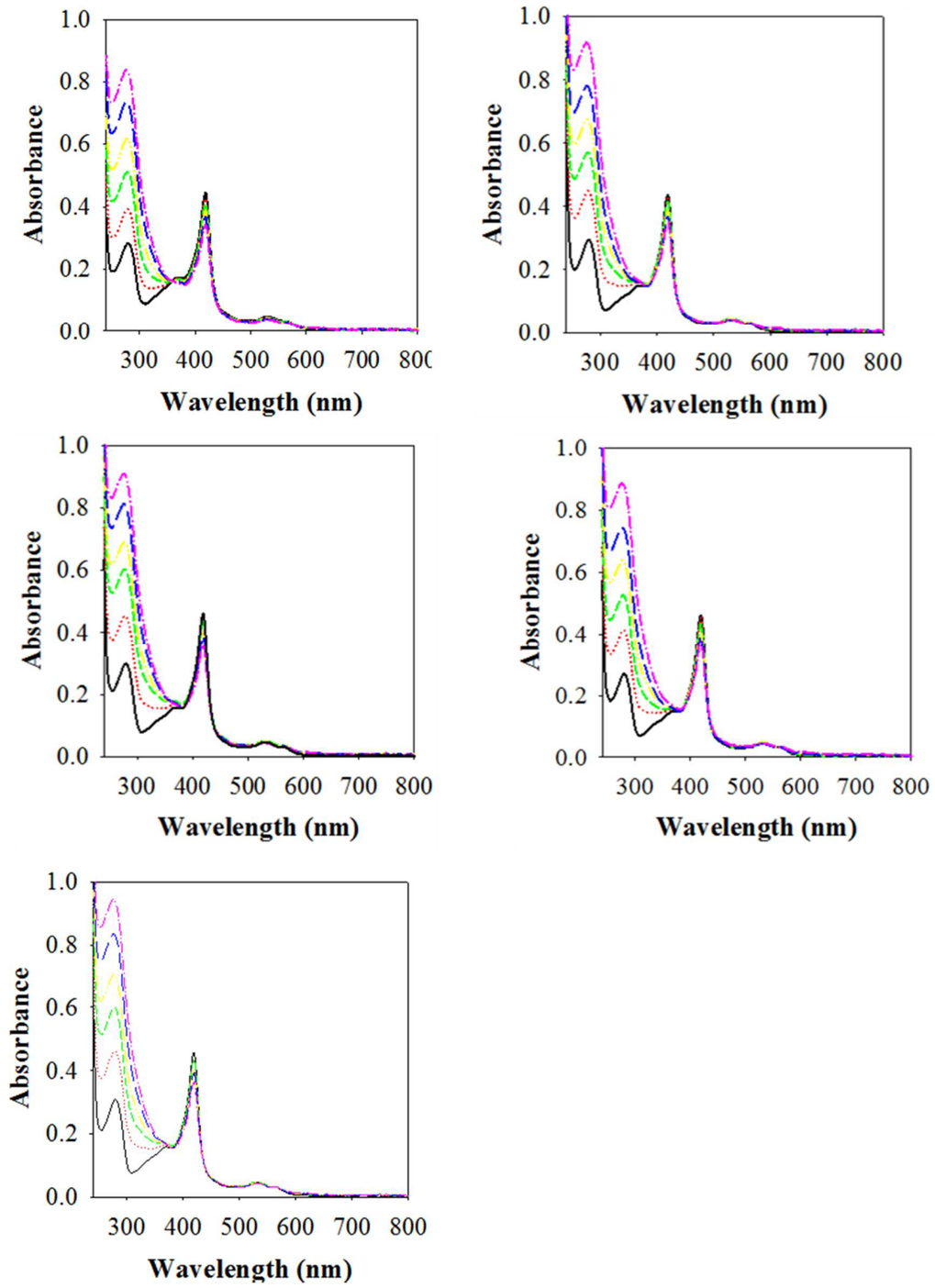

Figure 3-8 Iron uptake in (A) WT BfrB (B) BfrB L68A (C) BfrB E81A (D) BfrB E85A (E) BfrB L68A/E81A

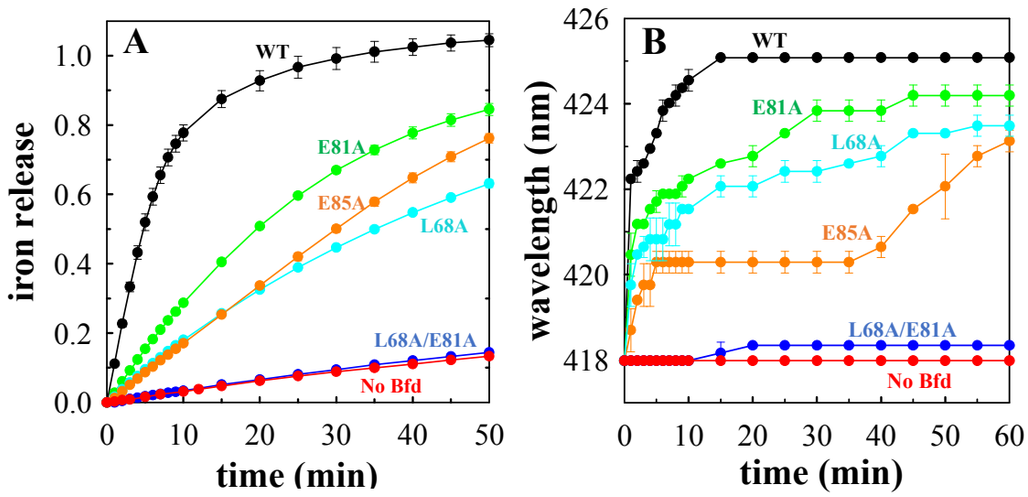

Figure 3-9 Bfd facilitated iron mobilization from the wild type and mutant BfrB. (A) Time-dependent plot of the percentage iron mobilized from BfrB wild type (black), E81A (green), L68A (cyan), E85A (orange) and L68A/E81A (blue). The iron release in the absence Bfd is shown in red. (B) Time-dependent change in the position of the Soret band during the iron mobilization process shown in (A). 418 nm and 425 nm represent fully oxidized and fully reduced heme respectively.

The BfrB mutants have significantly reduced affinity for Bfd

The findings described in the section above suggest that relative to wt BfrB, the BfrB mutants form less stable complexes with Bfd. Experimental support for this idea was obtained by measuring the binding constant for the associations between Bfd and each of the BfrB mutants using SPR, in a manner similar to that described above for the association between wt BfrB and Bfd. Figures 3-10 A-C illustrate the reference- and baseline-subtracted responses obtained from flowing Bfd over immobilized L68A, E81A, and E85A BfrB, respectively. For each of the mutants, the corresponding response reaches a plateu at each of the Bfd concentrations, indicating steady state equilibrium. Hence, the data was fitted to equation 4 to

obtain the corresponding K_d values. At each concentration of Bfd the corresponding response reaches a plateau, indicating steady state equilibrium. Plotting each response at the steady state as a function of Bfd concentration produces the binding plots defined by the black (E81A), red (L68A) and green (E85A) circles in Figure 3-10E. Fitting the data to equation 4 produced the corresponding K_d values (Table 3-5), which indicate that the association between Bfd and L68A or E81A BfrB is ≈ 100 times weaker than the corresponding association with wt BfrB, and that the E85A mutation results in the lowest affinity for Bfd, which is ≈170 times lower than that measured for wt BfrB. In comparison, the reference- and baseline-subtracted responses obtained from flowing Bfd over immobilized L68A/E81A BfrB (Figure 3-10D) indicate that the association between these two proteins is so low, as to become undetectable by SPR. The affinity of Bfd for BfrB decreases in the order wt >>E81A ≈ L68A > E85A >> L68A/E81A (Table 3-6), which could be taken to suggest that the efficiency of core iron mobilization should follow a similar order. The efficiency of iron mobilization, however, follows the order wt >> E81A > L68A ≈ E85A >> L68A/E81A. The explanation for these seeming discrepancies likely resides in the fact that biding affinity is not the only determinant for electron transfer between the two proteins. Rather, a productive interaction must place the [2Fe-2S] cluster of Bfd in relative close (optimum) proximity to the heme in BfrB so that electron transfer is facilitated. Consequently, it is possible that although the binding affinity of L68A > E85A, the latter undergoes more frequent interactions that are conducive to electron transfer.

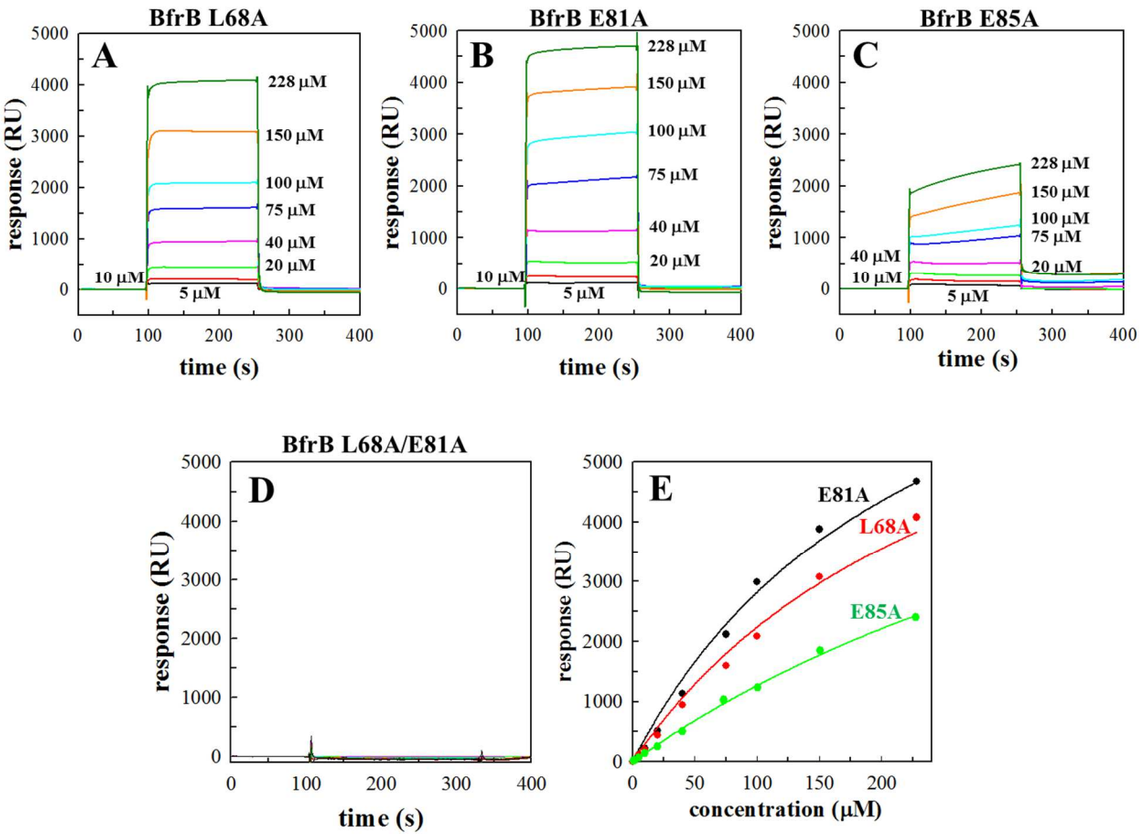

Figure 3-10 Measuring the binding affinity between Bfd and mutant BfrB by SPR. Overlay of double referenced sensorgrams resulting from the injections of different concentrations of Bfd (0~ 228 µM) over immobilized BfrB L68A (A), E81A (B), E85A (C) and L68A/E85A (D). (E) The steady state affinity fitting plots of Bfd binding to E81A, L68A and E85A are shown in black, red and green respectively.

Table 3-6. Initial iron release rates and binding affinities of wild type and mutant BfrB-Bfd interactions

Protein	Initial Rate (min $^{-1}$)	K_d (µM)
Wild Type	0.099 ± 0.007	3.0 ± 0.5
BfrB E81A	0.031 ± 0.0003	258.5 ± 21.5

BfrB L68A	0.019 ± 0.0003	298.5 ± 20.5
BfrB E85A	0.018 ± 0.0006	590± 2
BfrB L68A/E81A	0.0038 ± 0.0002	not measureable
Bfd Y2F	0.097 ± 0.004	3
Bfd K40A	0.090 ±0.002	12.8
Bfd L5A	0.044 ± 0.0005	98

X-Ray Crystal Structures of Mutant BfrB

The structure of the BfrB-Bfd complex showed that Bfd binding to BfrB is accompanied by relatively small rearrangements on the BfrB surface [12]. The most significant are the reorientation of the L68B, E81A and E85A side chains on BfrB, which enable hydrophobic and hydrophilic interactions with Bfd: The closer proximity of the L68 and E85 side chains narrows the cleft formed by the two side chains and stabilizes the burial of the Y2 side chain from Bfd (Figure 3-11A). The new conformation of the L68 side chain also participates in stabilizing the burial of the L5 side chain from Bfd. The side chain reorientations of E81 and E85 also enable H-bonding interactions between the backbone carbonyl oxygen of Y2 in Bfd and the carboxylic group of E81, as well as the backbone N-H of M1 in Bfd and the carboxylic group in E85. These interactions, in turn, allow the side chain of Met1 in Bfd to interact hydrophobically with the BfrB surface.

The X-ray crystal structures of BfrB L68A, BfrB E81A and BfrB E85A show that the overall organization of both proteins is nearly identical to that of the wt protein. Close inspection of the Bfd-binding site in L68A BfrB (Figure 3-11B) shows that the conformation of the E81 side chain remains as in the wt protein, but that the shorter side chain of A68 makes the cleft shallower on one side. This is expected to affect the extent of burial of the Bfd Y2 side

chain, and also affect the pocket where Bfd L5 anchors on the BfrB surface. The structure of the E81A mutant (Figure 3-11C) suggests than in addition to a shallower more open cleft where the burial of Y2 from Bfd is likely to be less efficient, a hydrogen bond between the NH of M1 in Bfd and a carboxyl O in BfrB E81 is lost. The shorter A85 side chain in the E85A mutant (Figure 3-11D) allows the E81 side chain to move away from the cleft and therefore create a wider gap, which is likely unfavorable for efficient burial of the Bfd Y2 side chain. In addition the hydrogen bonds between NH of M1 in Bfd and the carboxyl oxygens in BfrB E85 are no longer possible, which in turn may have an unfavorable effect on how the side chain of M1 in Bfd packs against the BfrB surface. In aggregate the E85A mutation eliminates more interactions than the L68A or E81A mutations, which is in agreement with the observation that the K_d measured for the interaction between Bfd and E85A BfrB is approximately 2-fold larger than the K_d values measured for the complexes formed between Bfd and L68A BfrB or E81A BfrB. Finally, the structure of the L68A/E81A mutant (Figure 3-11E) shows a very wide cleft, where the Y2 side chain in Bfd is unlikely to undergo any meaningful interactions, which is likely the reason why the association between Bfd and the double mutant is not measurable, which consequently inhibits the mobilization of core iron stored in E68A/E81A BfrB.

Mutations in Bfd

The X-ray crystal structure of the BfrB-Bfd complex revealed for the first time the Bfd fold, which consists of a helix-turn-helix motif, where the four Cys ligands to iron in the [2Fe-2S] cluster are located in two hairpin loops (Figure 3-12). It is noteworthy that iron ligands C4 and C6 are located in the same hairpin loop that contains M1, Y2 and L5, whose side chains anchor Bfd on the BfrB surface. We prepared the Y2A, Y2F, L5A and K40A mutants to study the effect of these mutations on the effectiveness of the mutants to promote the mobilization of

core iron from BfrB, and the stability of the corresponding complexes with BfrB. The Y2A mutant cannot form a stable [2Fe-2S] cluster, likely because the Y2 side chain helps stabilize the hairpin containing C4 and C6 via packing interactions with G8 and T10 (Figure 3-11). Since the Y2A mutant couldn't be studied, we prepared the Y2F mutant, in an attempt to understand the role played by the phenolic OH on Y2 in the stabilization of the BfrB-Bfd interaction. All the Bfd mutants (Y2F, L5A and K40A) have similar UV-vis spectroscopic features as the wild type Bfd (Figure 3-13). The binding affinity measurements by SPR show that replacement of Leu5 to Ala decreases the binding affinity to ~ 98 μM, while the mutation of Lys40 to Ala only decrease the binding affinity to ~ 12.8 μM and the mutation of Tyr2 to Ala show a similar binding affinity as the wild type protein (Table 3-6). As shown in Figure 3-14 and Table 3-6, for mobilization of iron from BfrB, among the three mutations, only L5A causes significant decreases in the rate of iron mobilization from BfrB, as shown by the red trace in Figure 3-14. The rate of iron mobilization with Y2F or K40A is nearly the same as the wild type Bfd, as shown by the black and green traces in Figure 3-14.

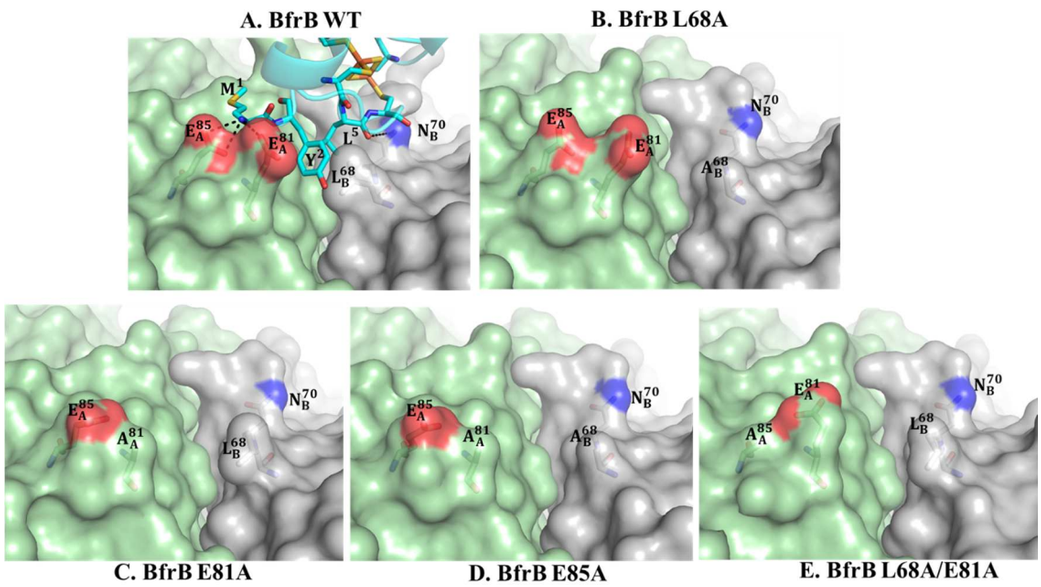

Figure 3-11. View of wild type BfrB-Bfd interface and the Bfd binding sites on mutant BfrB surface. (A) Bfd (cyan) binds to wild type BfrB at the interface of a BfrB subunit dimer (subunit A in green and subunit B in gray). BfrB E_A^{81}, L_B^{68} and E_A^{85} interact with Bfd Y2, L5 and M1 through hydrophobic interactions and electrostatic interactions; O and N atoms are shown in red and blue respectively. (B)-(E) The same view as (A) to show the Bfd binding sites on the BfrB surface upon mutating the L68 to Ala (B); E81 to Ala (C); E85 to Ala (D) and L68/E81 to Ala (E).

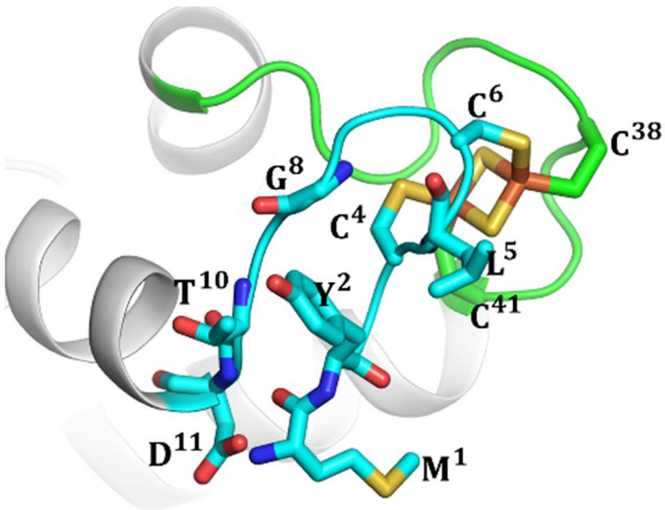

Figure 3-12. Structural organization of Bfd (PDB 4E6K). Y2 interacts with G8 and T10 to stabilize the hairpin containing C4 and C6 (cyan). O, N and S atoms are shown in red, blue and yellow respectively.

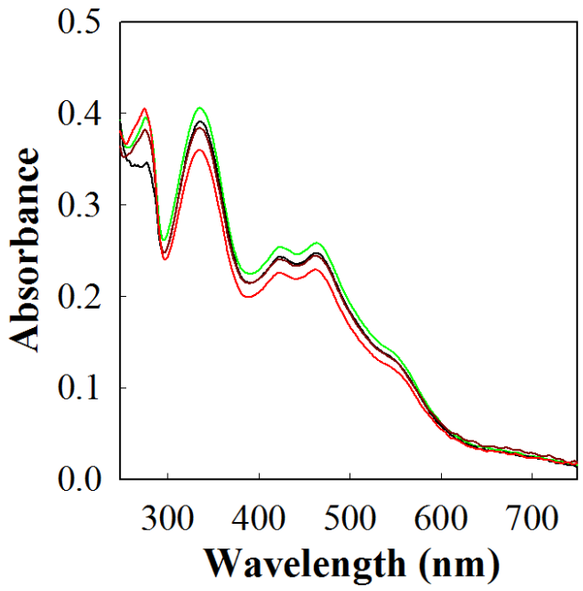

Figure 3-13 UV-vis spectra of Bfd wild type (brown) and mutant Y2F (black), L5A (red) and K40A (green)

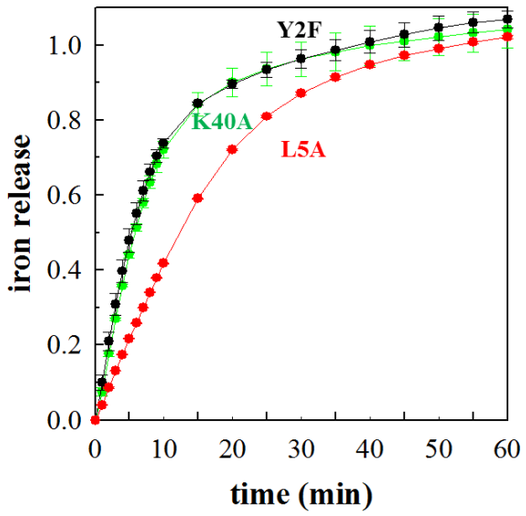

Figure 3-14 Iron mobilization from BfrB in the presence of Bfd mutant Y2F (black), K40A (green) and L5A (red).

Discussion

Identification of the hotspot

Based on the K_d values, the changes in BfrB-Bfd binding free energy (ΔΔG) caused by the different mutations are shown in Figure 3-15 A and B. The mutation that causes the most change in the binding free energy is BfrB E85A, followed by BfrB L68A and E81A, indicating the residues E_A^{85}, E_A^{81}, L_B^{68} in BfrB contribute most to stabilize the BfrB-Bfd complex. Bfd L5 has slightly less contribution than the residues above, yet it still significantly stabilizes the BfrB-Bfd complex. In contrast, Bfd K40 has much lower contribution to the binding free energy and the phenolic OH on Y2 does not show any stabilization of the BfrB-Bfd complex. The residues that have the most contributions to stabilize the complex (interaction hotspot) are summarized in Figure 3-15C, where a Bfd molecule (cyan) binds to a BfrB subunit dimer between the subunit A (green) and B (gray). A hot region is formed by the hotspot residues BfrB E_A^{85}, E_A^{81}, L_B^{68}, Bfd Y2 and L5, which indicates that the cleft and pocket on BfrB where the side chains of Y2 and L5 bury to anchor Bfd are essential to the stability of the BfrB complex.

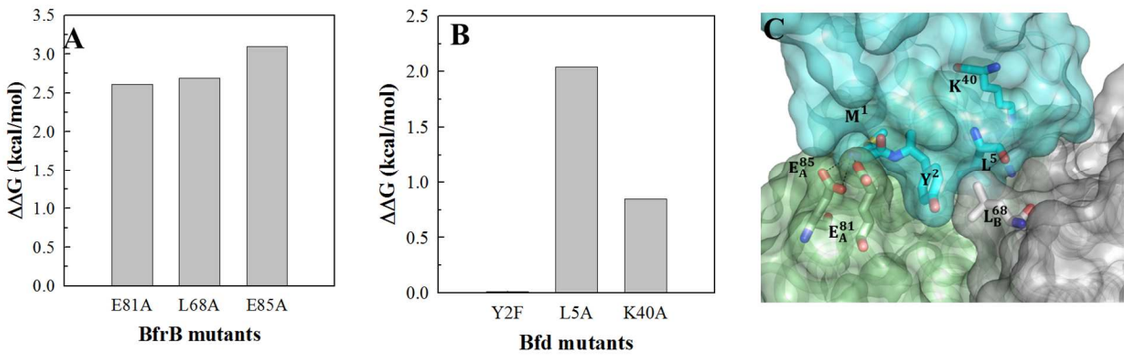

Figure 3-15 Identification of hotspot of the BfrB-Bfd interaction. The change in BfrB-Bfd binding free energy (ΔΔG) caused upon mutation to BfrB and Bfd are shown in (A) and (B) respectively. The hotspot residues are highlighted in (C), with O in red and N in blue.

BfrB-Bfd Binding is an Endothermic Reaction.

As shown in Table 3-5, the small positive value of ΔH indicates that BfrB/Bfd association is endothermic. The negative value of ΔG is contributed by the large positive value of TΔS, indicating that the reaction is driven by entropy. The BfrB-Bfd binding, as indicated by the crystal structure, is dominated by hydrophobic interactions. Therefore, it is possible that the entropy increase is due to the hydrophobic interactions between BfrB and Bfd that cause water molecules being released from the binding interface. An analysis of this process is shown in Figure 3-16, the binding clefts in free BfrB which are composed by the BfrB $E_A^{81}$and L_B^{68} as well as by L_B^{68}, P_B^{69}, N_B^{70}, L_B^{71}, Q_B^{72}, L_A^{77} and I_A^{79} are occupied with water molecules (Figure 3-16A). Binding of Bfd Y2 and L5 to this cleft exclude the water molecules from the cleft to the surroundings (Figure 3-16B).

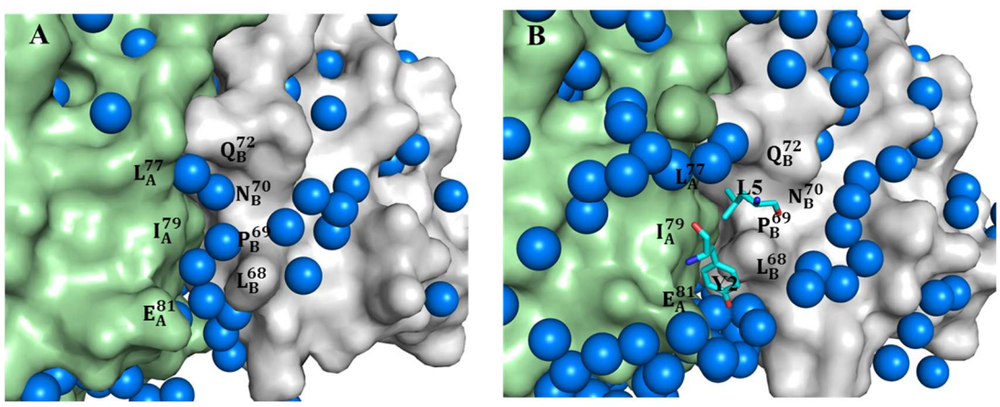

Figure 3-16 X-ray crystal structures of (A) Free BfrB binding cleft filled with water molecules (blue sphere) (B) Bfd binding to the BfrB cleft to exclude water molecules to the surrounding

References

1. Cornelis, P., et al., *Iron homeostasis and management of oxidative stress response in bacteria.* Metallomics, 2011. **3**(6): p. 540-9.
2. Weinberg, E.D., *Iron Availability and Infection.* Biochim. et Biophys. Acta, 2009. **1790**: p. 600-605.
3. Bullen, J.J., et al., *Iron and Infection: The Heart of the Matter.* FEMS Immunol. Med. Microbiol., 2005. **43**: p. 325-330.
4. Touati, D., *Iron and oxidative stress in bacteria.* Arch Biochem Biophys, 2000. **373**(1): p. 1-6.
5. Keyer, K. and J.A. Imlay, *Superoxide Accelerates DNA-Damage by Elevating Free-Iron Levels.* Proc. Natl. Acad. Sci. USA, 1996. **193**: p. 13635-13649.
6. Honarmand Ebrahimi, K., P.L. Hagedoorn, and W.R. Hagen, *Unity in the biochemistry of the iron-storage proteins ferritin and bacterioferritin.* Chem Rev, 2015. **115**(1): p. 295-326.
7. Rivera, M., *Bacterioferritin: Structure Function and Protein-Protein Interactions*, in *Handbook of Porphyrin Science*, K.K. Kadish, K.M. Smith, and R. Guilard, Editors. 2014. p. 136-179.
8. Andrews, S., et al., *Control of iron metabolism in bacteria.* Met Ions Life Sci, 2013. **12**: p. 203-39.
9. Yao, H., et al., *Concerted motions networking pores and distant ferroxidase centers enable bacterioferritin function and iron traffic.* Biochemistry, 2015. **54**(8): p. 1611-27.

10. Ruvinsky, A.M., I.A. Vakser, and M. Rivera, *Local packing modulates diversity of iron pathways and cooperative behavior in eukaryotic and prokaryotic ferritins.* J Chem Phys, 2014. **140**(11): p. 115104.

11. Andrews, S.C., A.K. Robinson, and F. Rodríguez-Quiñones, *Bacterial Iron Homeostasis.* FEMS Microbiology Reviews, 2003. **27**: p. 215-237.

12. Yao, H., et al., *The Structure of the BfrB-Bfd Complex Reveals Protein-Protein Interactions Enabling Iron Release from Bacterioferritin.* Journal of the American Chemical Society, 2012. **134**(32): p. 13470-81.

13. Escolar, L., J. Perez-Martin, and V. De Lorenzo, *Opening the Iron Box: Transcriptional Metalloregulation by the Fur Protein.* J. Bacteriol., 1999. **181**: p. 6223-6229.

14. Vasil, M.L., *How We Learnt About Iron Acquisition in Pseudomonas aeruginosa: A Series of Very Fortunate Events.* Biometals, 2007. **20**: p. 587-601.

15. Oglesby-Sherrouse, A.G. and E.R. Murphy, *Iron-responsive bacterial small RNAs: variations on a theme.* Metallomics, 2013. **5**(4): p. 276-86.

16. Masse, E., C.K. Vanderpool, and S. Gottesman, *Effect of RyhB small RNA on global iron use in Escherichia coli.* J Bacteriol, 2005. **187**(20): p. 6962-71.

17. Pandey, R. and G.M. Rodriguez, *A ferritin mutant of Mycobacterium tuberculosis is highly susceptible to killing by antibiotics and is unable to establish a chronic infection in mice.* Infect Immun, 2012. **80**(10): p. 3650-9.

18. Reddy, P.V., et al., *Iron storage proteins are essential for the survival and pathogenesis of Mycobacterium tuberculosis in THP-1 macrophages and the guinea pig model of infection.* J Bacteriol, 2012. **194**(3): p. 567-75.

19. Chen, C.Y. and S.A. Morse, *Neisseria gonorrhoeae bacterioferritin: structural heterogeneity, involvement in iron storage and protection against oxidative stress.* Microbiology, 1999. **145 (Pt 10)**: p. 2967-75.

20. Expert, D., A. Boughammoura, and T. Franza, *Sidreophore-Controlled Iron Assimilation in the Enterobacterium Erwinia chrysanthemi.* J. Biol. Chem., 2008. **283**: p. 36564-36572.

21. Andrews, S.C., P.M. Harrison, and J.R. Guest, *Cloning, Sequencing, and Mapping of the Bacterioferritin Gene (bfr) of Escherichia coli K-12.* J. Bacteriol., 1989. **171**: p. 3940-3947.

22. Quail, M.A., et al., *Spectroscopic and Voltammetric Characterization of Bacterioferritin-Associated Ferredoxin of Escherichia coli.* Biochem. Biophys. Res. Commun., 1996. **229**: p. 635-642.

23. Garg, R.P., et al., *A [2Fe-2S] Protein Encoded by an Open Reading Frame Upstream of the Escherichia coli Bacterioferritin Gene.* Biochemistry, 1996. **35**: p. 6297-6301.

24. Ochsner, U.A., et al., *GeneChip Expression Analysis of the Iron Starvation Response in Pseudomonas Aeruginosa: Identification of Novel Pyoverdine Biosynthesis Genes.* Mol. Microbiol., 2002. **45**: p. 1277-1287.

25. Palma, M., S. Worgall, and L.E.N. Quadri, *Transcriptome Analysis of the Pseudomonas aeruginosa Response to Iron.* Arch. Microbiol., 2003. **180**: p. 374-379.

26. Weeratunga, S., et al., *Binding of Pseudomonas aeruginosa Apobacterioferritin-Associated Ferredoxin to Bacterioferritin B Promotes Heme Mediation of Electron Delivery and Mobilization of Core Mineral Iron.* Biochemistry, 2009. **48**: p. 7420-7431.

27. Weeratunga, S., et al., *Structural Studies of Bacterioferritin B (BfrB) from Pseudomonas aeruginosa Suggest a Gating Mechanism for Iron Uptake via the Ferroxidase Center.* Biochemistry, 2010. **49**: p. 1160-1175.

28. Wang, A., et al., *X-Ray Crystallographic and Solution State Nuclear Magnetic Resonance Spectroscopic Investigations of $NADP^+$ Binding to Ferredoxin NADP Reductase from Pseudomonas aeruginosa.* Biochemistry, 2008. **47**: p. 8080-8093.

29. Weeratunga, S.K., et al., *Binding of Pseudomonas aeruginosa apobacterioferritin-associated ferredoxin to bacterioferritin B promotes heme mediation of electron delivery and mobilization of core mineral iron.* Biochemistry, 2009. **48**(31): p. 7420-31.

30. Wong, S.G., et al., *Fe-haem bound to Escherichia coli bacterioferritin accelerates iron core formation by an electron transfer mechanism.* Biochem J, 2012. **444**(3): p. 553-60.

31. Berry, E.A. and B.L. Trumpower, *Simultaneous determination of hemes a, b, and c from pyridine hemochrome spectra.* Anal Biochem, 1987. **161**(1): p. 1-15.

32. Weeratunga, S.K., et al., *Structural studies of bacterioferritin B from Pseudomonas aeruginosa suggest a gating mechanism for iron uptake via the ferroxidase center.* Biochemistry, 2010. **49**(6): p. 1160-75.

33. Ringeling, P.L., et al., *Iron metabolism in Rhodobacter capsulatus. Characterisation of bacterioferritin and formation of non-haem iron particles in intact cells.* Eur J Biochem, 1994. **223**(3): p. 847-55.

34. Evans, P.R., *An introduction to data reduction: space-group determination, scaling and intensity statistics.* Acta Crystallogr D Biol Crystallogr, 2011. **67**(Pt 4): p. 282-92.

35. Evans, P., *Scaling and assessment of data quality.* Acta Crystallogr D Biol Crystallogr, 2006. **62**(Pt 1): p. 72-82.

36. Diederichs, K. and P.A. Karplus, *Improved R-factors for diffraction data analysis in macromolecular crystallography.* Nat Struct Biol, 1997. **4**(4): p. 269-75.

37. Weiss, M.S., *Global indicators of x-ray data quality.* Journal of Applied Crystallography, 2001. **34**: p. 130-135.

38. Karplus, P.A. and K. Diederichs, *Linking crystallographic model and data quality.* Science, 2012. **336**(6084): p. 1030-3.

39. Evans, P., *Biochemistry. Resolving some old problems in protein crystallography.* Science, 2012. **336**(6084): p. 986-7.

40. *Biacore sensor surface handbook.* 2003.

41. Rivera, M., *Bacterioferritin: Structure Function and Protein–Protein Interactions*, in *Handbook of Porphyrin Science (Volume 30)*. p. 135-178.

42. Wilkinson, K.D., *Quantitative analysis of protein-protein interactions.* Methods Mol Biol, 2004. **261**: p. 15-32.

43. *Biacore assay handbook.* GE healthcare life sciences.

44. Infectious Diseases Society of, A., *The 10 x '20 Initiative: pursuing a global commitment to develop 10 new antibacterial drugs by 2020.* Clin Infect Dis, 2010. **50**(8): p. 1081-3.

45. *BIAevaluation software handbook.* 2004.

CHAPTER IV

Designing an assay to determine the efficacy of compounds developed to inhibit the BfrB/Bfd interaction

Introduction

As mentioned in Chapter 1, the emergence of multi-drug resistant pathogen strains requires discovery of novel targets for antibiotic development. Bacterial iron homeostasis could provide such a target. In previous chapters, our studies towards understanding the protein-protein interactions that regulate the iron homeostasis in *Pseudomonas aeruginosa* have demonstrated that disrupting the BfrB-Bfd interaction could potentially disrupt the intracellular iron regulation in bacteria. As a long-term goal, we have initiated an effort towards designing drug molecules to disrupt the BfrB-Bfd interaction. Specifically, we are seeking compounds to bind BfrB at the Bfd binding site. Consequently, the compounds would displace Bfd binding to BfrB; therefore, it would disrupt the BfrB-Bfd interaction.

Discovery of chemical leads is the first crucial step for discovering potential drug candidates [1]. Chemical leads are molecules that have good potency to target mechanisms of interest. There are four most widely used approaches to obtain chemical leads: (1) Carrying out modifications on an existing lead or drug [2]. (2) Discovery of a natural product [3]. (3) High throughput drug screening (HTS) [4]. (4) Fragment based drug design (FBDD) [1, 5, 6].

For our purpose of disrupting the interaction between BfrB and Bfd, the first two methods are less feasible due to the unique and novel nature of our target interactions. HTS is currently a dominant method for lead identification used in industry. In this approach, several millions of compounds need to be screened against the target of interest. The identified hits are

further optimized into chemical leads with desired bioactivity [1, 5]. HTS, however, can be expensive due to the requirement of having to screen very large compound libraries.

In the last decade, FBDD has emerged as a viable alternative to HTS [1, 6-8]. The FBDD approach is based on the principle that drug molecules usually contain several interconnected functional fragments. The aim of FBDD is to identify the fragments with desired bioactivity (called "hits") and further optimize these hits into chemical leads with high potency [1]. Compared to HTS, the advantage of FBDD is that the fragments have a relatively simple molecular structure, lower molecular weight (150 kDa ~ 250 kDa), and higher solubility [5, 6, 9, 10]. In FBDD, typically ~1000 fragments are screened using biophysical approaches, which is a much smaller number compared to traditional HTS method [5]. The low chemical complexity can simplify the interpretation of the structure-activity relationship, which could benefit the later process of fragment optimization [6]. In addition, the simple ligand-receptor interaction model shows that fragments give higher hit rates than molecules with more complexity, because molecules of more complexity have higher chance to form mismatches with proteins through suboptimal interactions [5]. Although as a main disadvantage of FBDD, the fragments bind to target proteins with lower affinity, which requires high concentrations of soluble fragments, high amount of purified proteins, and high sensitive screening methods. Nevertheless, fragments may actually form interactions that are more efficient. Compared to binding affinity, ligand efficiency (LE) is a more powerful parameter to evaluate the relative optimizability of different sized molecules. LE equals to the free energy of binding divided by the number of heavy atoms [11, 12]. For example, given a LE value bigger than 0.3, a weak binding fragment (IC_{50} in mM range) could be carefully optimized into a chemical lead with IC_{50} in nM range [5].

Protein-protein interaction “hot spots” are a small number of residues that contribute to the vast majority of the stabilizing energy in a protein-protein complex [13]. Ligands that bind to target proteins with high affinity have stronger interactions with hot spots on the target protein surface, which allow the ligands to be properly oriented at the protein surfcae [6]. This idea is well-matched to FBDD approaches, as fragments often form interactions with the hot spots, which lead high ligand efficiency [6].

In chapter 3, three regions on the BfrB-Bfd binding interface were identified as the hot spots: (i) the binding cleft on BfrB surface formed by E_A^{81} and L_B^{68} which holds the Bfd Y2. (ii) The pocket on BfrB formed by BfrB L_B^{68}, P_B^{69}, N_B^{70}, L_B^{71}, Q_B^{72}, L_A^{77} and I_A^{79} which holds the Bfd L5. (iii) Bfd amine group in M1 forms hydrogen bonds with carboxyl side chains of E_A^{85} and E_A^{81} on BfrB and interacts hydrophobically with BfrB L_A^{77} L_A^{78}, I_A^{79}, G_A^{80} and C_A^{89}. The identification of the hot spot for the BfrB-Bfd interaction and the structural information of the BfrB-Bfd interface have provided basis for designing the fragment library.

The standard process of FBDD includes establishing a fragment library, screening fragments, identifying initial hits, and optimizing the hits to chemical leads [5]. The strategy used by our group to find inhibitors to disrupt the BfrB-Bfd interaction is shown in Figure 4-1.

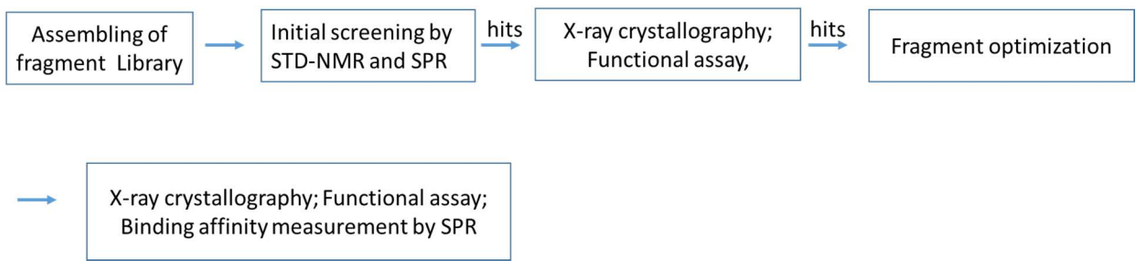

Figure 4-1 Process of finding inhibitors to disrupt the BfrB-Bfd interaction using FBDD.

Among the process in Figure 4-1, my work focused on testing the bioactivity of the fragment hits and derived analogs using *in vitro* functional assay. As mentioned in the previous chapters, iron mobilization from BfrB requires interaction between BfrB and Bfd. Therefore, the efficiency of iron mobilization from BfrB is a gauge to evaluate the efficiency of the potential inhibitors to disrupt the BfrB-Bfd interaction. Ideally, if the fragments/compounds compete with Bfd to bind to BfrB, we expect to observe a reduced iron mobilization efficiency because of reduced interaction between Bfd and BfrB.

Two sources of fragments/compounds were tested for their *in vitro* inhibition effect. The first source is a fragment library (FC library) composed of 225 fragments. This library was assembled by Dr. Allen B. Reitz from Fox Chase Chemical Diversity Center, Inc., Doylestown, Pennsylvania. The library was screened by Dr. Huili Yao in our group, who found that 6 fragments bind BfrB specifically at the Bfd-binding sites. By soaking crystals of BfrB in solutions containing these fragments, the structure of a fragment bound to BfrB was solved by Dr. Scott Lovell (Structural Biology Laboratory). The structural information obtained from this crystal structure was used to design several analogs with improved binding affinity for BfrB. The analogs were synthesized by Baskar Namwalar in Dr. Richard Bunce's laboratory at Oklahoma State University, Stillwater, Oklahoma. As shown in Figure 4-1, I studied the effect of both, fragments and analogs, on the inhibition of the BfrB/Bfd interaction. A second source of potential inhibitors of the BfrB/Bfd interaction was obtained from a virtual screen of the ZINC drugs catalog [14], which was carried out by David Johnson in Dr. John Karanicolas' laboratory (center for computational biology).

Experimental Procedures

Mobilization of iron from BfrB in the presence of compounds

In order to explore the inhibition of the BfrB-Bfd interaction caused by the compounds, the efficiency of iron mobilization from BfrB was evaluated in the presence of a variety of compounds, including the fragments from the FC library, analogs optimized from the fragments, and compound hits from the virtual screen of the ZINC library. Prior to the assay, the solubility of each compound/fragment in 50 mM potassium phosphate (pH 7.6) containing 10% DMSO was determined, so that the concentration of each compound could be maximized in the assay without compromising its solubility in aqueous buffer. In addition, the pH of the buffer containing the maximal concentration of each compound was also measured, so that the pH of each mixture could be adjusted to 7.6 prior to starting the assay.

In an anaerobic chamber, 0.08 μM BfrB (loaded with 500 ± 20 iron), 0.4 μM Bfd and 3.2 μM FPR (final concentrations) were mixed in a cuvette containing 50 mM potassium phosphate (pH 7.6) and 3 mM ferrozine. A small volume of compound dissolved in DMSO (stock solution) was added into the cuvette so that the compound reached the desired concentration and the total DMSO volume was 10% of the total volume. The effect of DMSO caused the final pH of the solution to be ~ 8. The reaction was initiated by addition of 1 mM NADPH and the release of Fe^{2+} from BfrB was monitored by tracking the time-dependent formation of the Fe(II)-ferrozine complex, which absorbs at 562 nm. The percentage of mobilized iron was calculated by normalizing the absorbance at 562 nm to the absorbance expected upon mobilization of all the iron stored in BfrB. For the compound hits in ZINC library, the concentration of FPR was reduced to 2.4 μM and the concentration of the NADPH

was reduced up to 0.5~ 0.1 mM. The control experiment was done by repeating the above process but in the absence of the compounds.

Results

Toward an inhibitor of the BfrB/Bfd interaction

Results obtained from testing fragment hits from the FC fragment library show that all the fragments which bind BfrB at the Bfd binding site do not inhibit the BfrB/Bfd interaction or affect the iron mobilization efficiency. This is not surprising, since fragments bind to protein surfaces with K_d values between 0.1 and 10 mM [5]. Our attempts at co-crystallizing fragments with BfrB showed that one of the fragments (FC996) binds BfrB at the cleft formed by L_B^{68}, P_B^{69}, N_B^{70}, L_B^{71}, Q_B^{72}, L_A^{77} and I_A^{79} (Figure 4-2A), which is the cleft being identified as the hot spot to hold Bfd L5. However, the mobilization of iron stored in BfrB (Figure 4-2B) indicates the reaction containing 10 mM FC996 (red) has the same iron mobilization efficiency as the control (black). This indicates that the fragment FC996 is not yet potent enough to exert *in vitro* inhibition effects because of its low molecular weight. However, the fact that it binds at the BfrB-Bfd interface suggests it has potential to be optimized to a more potent binder.

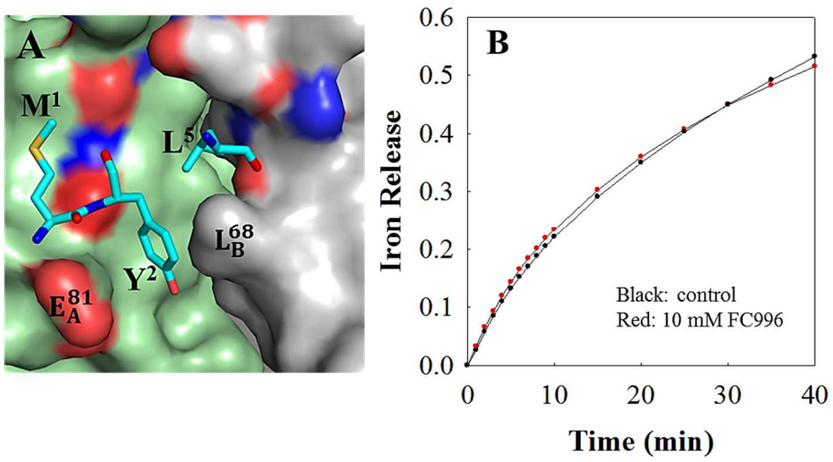

Figure 4-2 (A) Bfd Y2 and L5 insert into the binding pockets on the BfrB surface. (B) Iron mobilization from BfrB in the presence of 10 mM FC996 (red) compared to the control (black).

A series of larger compounds (MW ~ 300 Da) were synthesized by growing the structure of FC996 (FC996-optimized compounds). These compounds are less soluble than the initial fragments. However, some of them have shown significant inhibition of the BfrB/Bfd interaction, assessed by their ability to slow down the mobilization of iron from BfrB. A summary of the results is listed in Figure 4-3. In each plot, the efficiency of mobilizing iron stored in BfrB in the presence of a given compound is compared with the control, which is the iron mobilization reaction in the absence of compound. The black circles track the control and the red/green circles track the iron mobilization reaction in the presence of different concentrations of compounds. Among all the compounds, BNX111068, BNX111091 and BNX111093 show the most significant inhibition effects observed thus far, which are also concentration dependent.

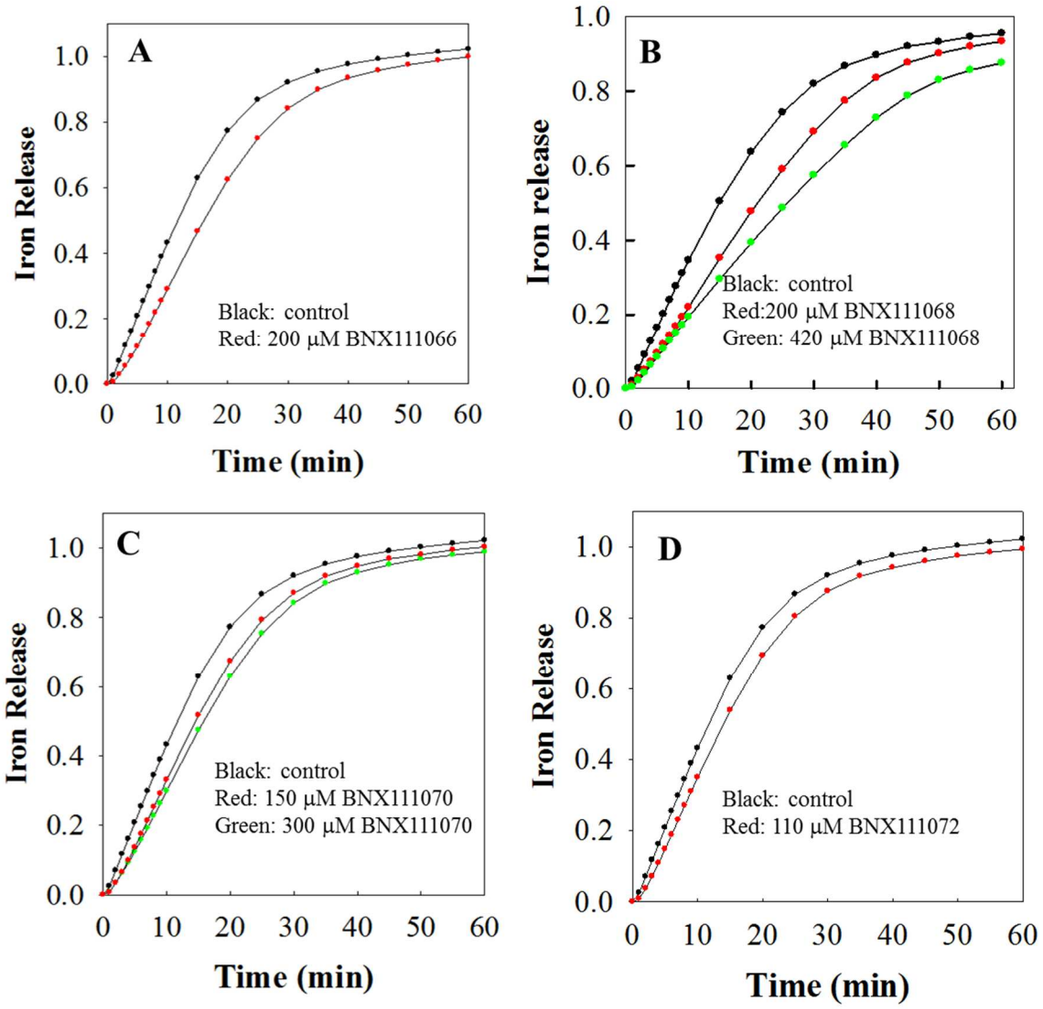
A
Iron Release
Time (min)
Black: control
Red: 200 µM BNX111066
B
Iron release
Time (min)
Black: control
Red:200 µM BNX111068
Green: 420 µM BNX111068
C
Iron Release
Time (min)
Black: control
Red: 150 µM BNX111070
Green: 300 µM BNX111070
D
Iron Release
Time (min)
Black: control
Red: 110 µM BNX111072

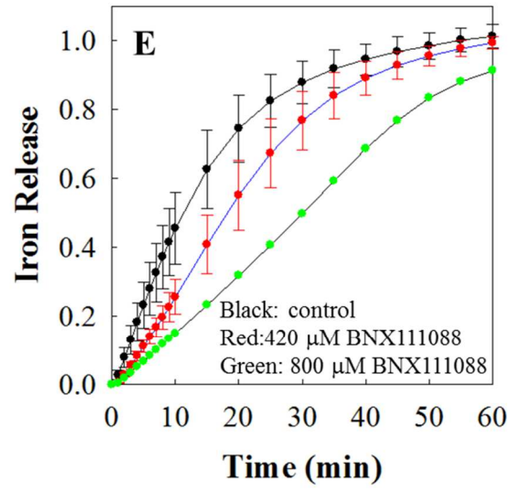
E
Iron Release
Time (min)
Black: control
Red:420 µM BNX111088
Green: 800 µM BNX111088

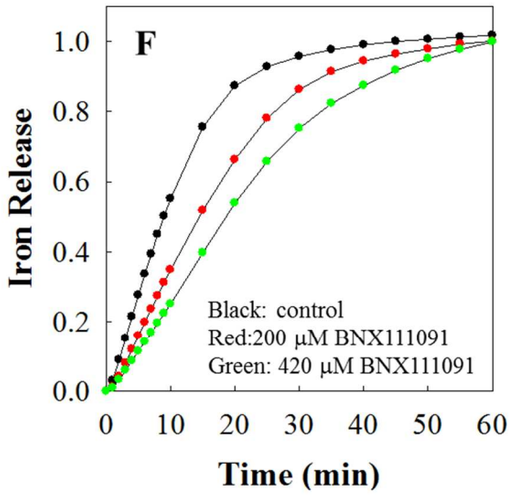
F
Iron Release
Time (min)
Black: control
Red:200 µM BNX111091
Green: 420 µM BNX111091

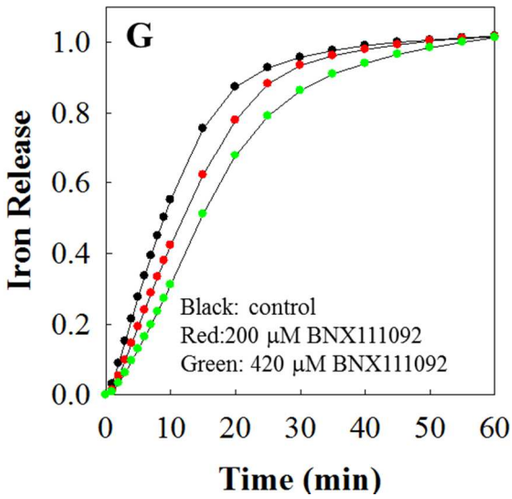
G
Iron Release
Time (min)
Black: control
Red:200 µM BNX111092
Green: 420 µM BNX111092

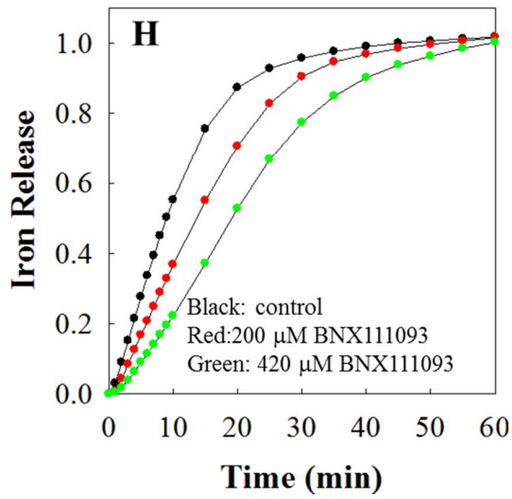
H
Iron Release
Time (min)
Black: control
Red:200 µM BNX111093
Green: 420 µM BNX111093

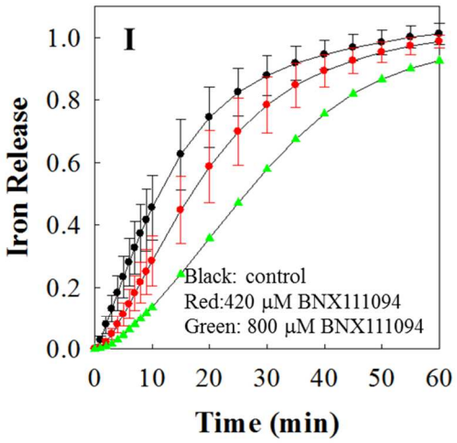
I
Iron Release
Time (min)
Black: control
Red:420 µM BNX111094
Green: 800 µM BNX111094

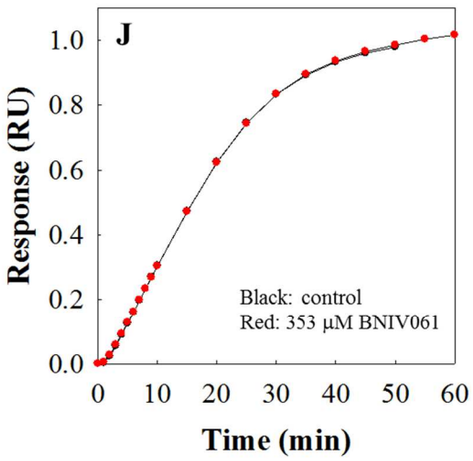
J
Response (RU)
Time (min)
Black: control
Red: 353 µM BNIV061

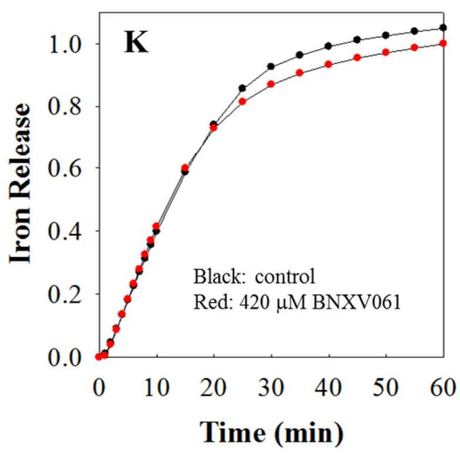
K
Iron Release
Time (min)
Black: control
Red: 420 µM BNXV061

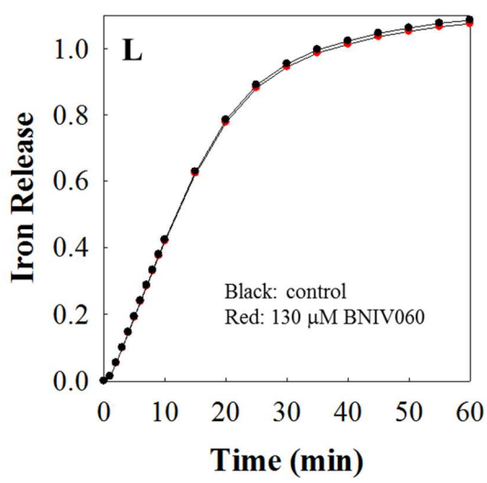
L
Iron Release
Time (min)
Black: control
Red: 130 µM BNIV060

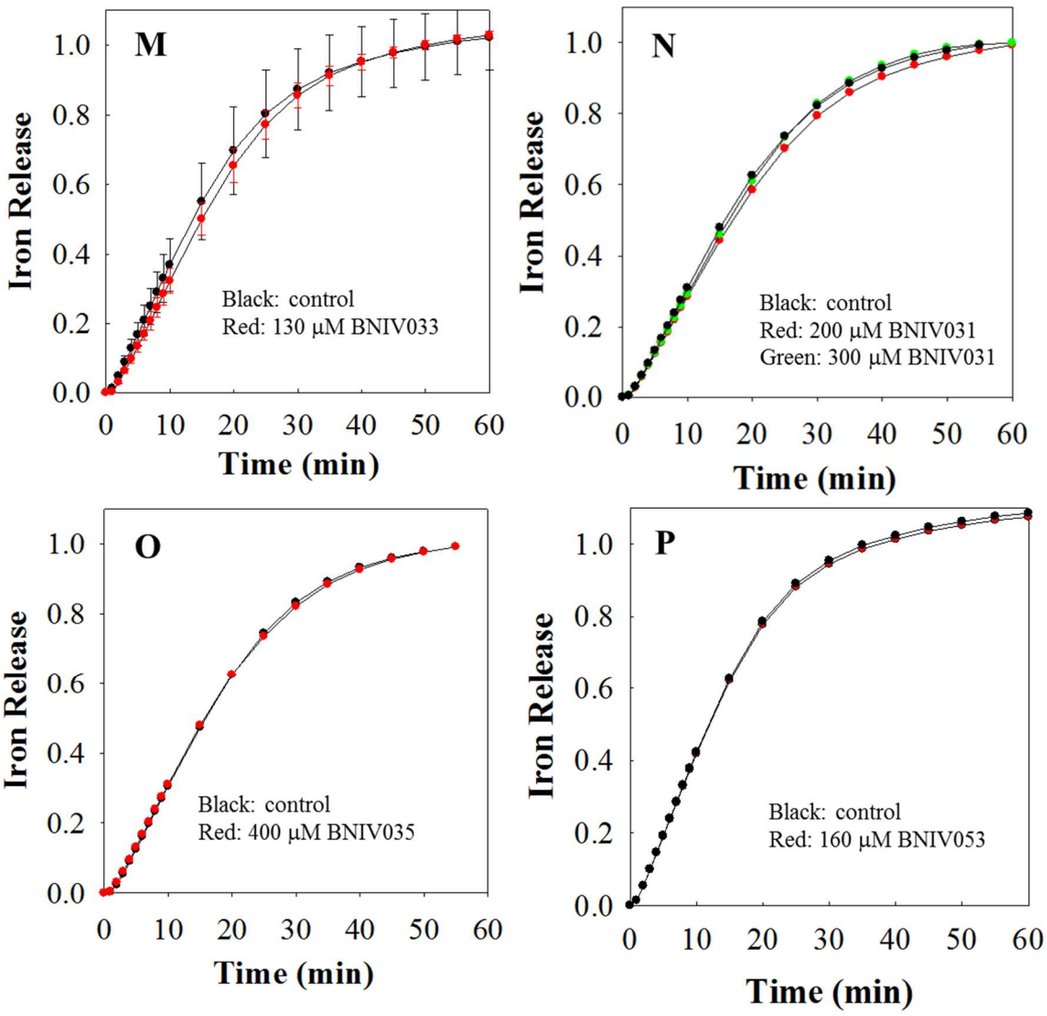
M
Iron Release
Time (min)
Black: control
Red: 130 µM BNIV033
N
Black: control
Red: 200 µM BNIV031
Green: 300 µM BNIV031
O
Black: control
Red: 400 µM BNIV035
P
Black: control
Red: 160 µM BNIV053

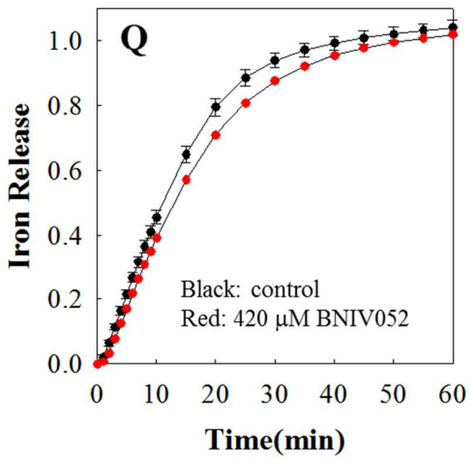
Q
Iron Release
Time(min)
Black: control
Red: 420 µM BNIV052

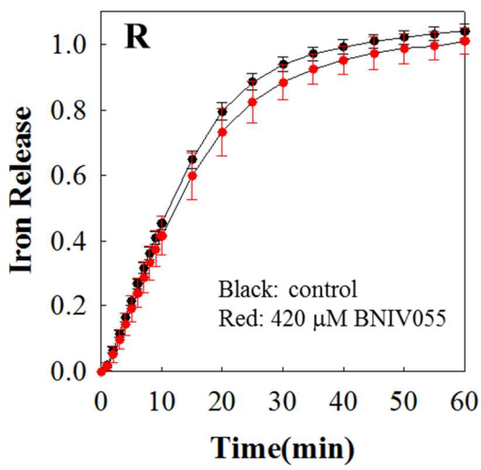
R
Iron Release
Time(min)
Black: control
Red: 420 µM BNIV055

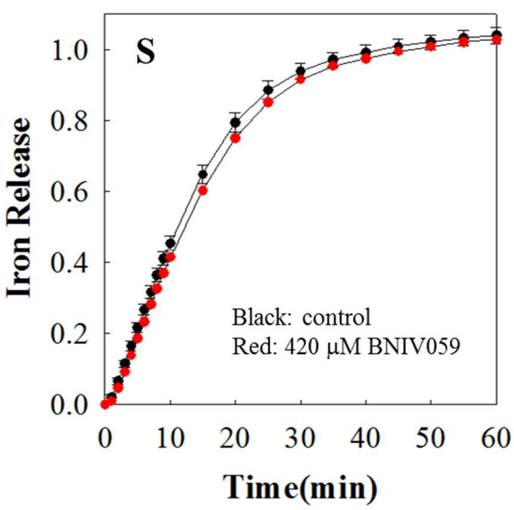
S
Iron Release
Time(min)
Black: control
Red: 420 µM BNIV059

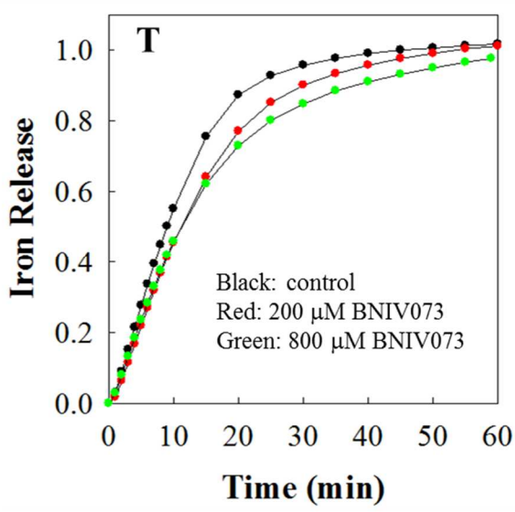
T
Iron Release
Time (min)
Black: control
Red: 200 µM BNIV073
Green: 800 µM BNIV073

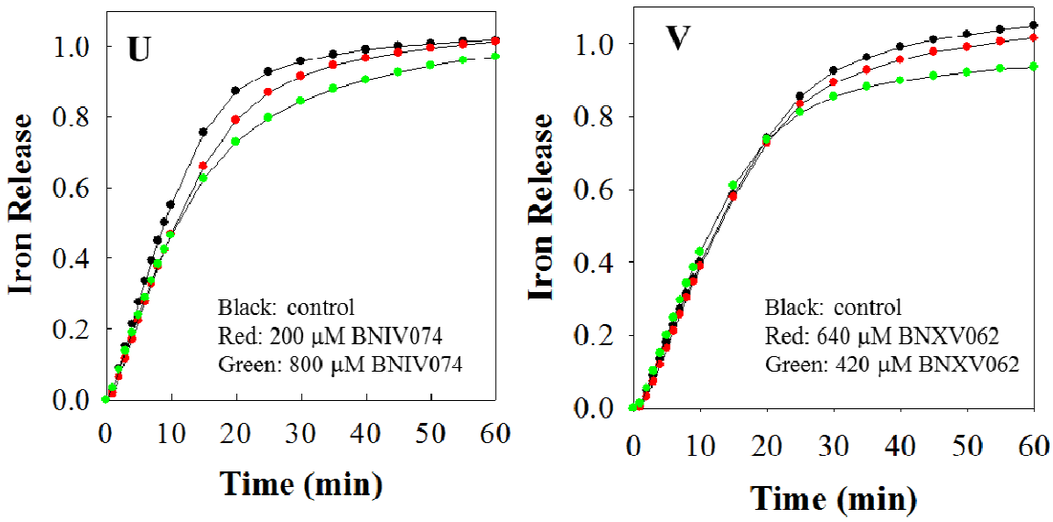

Figure 4-3 Iron mobilization assay in the presence of several analogs designed from the structural information obtained in the co-crystal structure of FC996 bound to BfrB (A-V). The ID and concentration of the compounds are listed in the right corner of each plot. The black trace tracks the control; the red/green traces track each compound at different concentrations.

For the hits obtained from a virtual screening of the ZINC library, the results are summarized in Figure 4-4. Since the assays were carried out with lower concentration of NADPH (0.1 ~ 0.5 mM) and FPR (2.4 µM) compared to the experiments above (1 mM NADPH and 3.2 µM FPR), the iron release rates are generally lower for both, the control and the reactions in the presence of compound. Nevertheless, the iron mobilization efficiency for a a given compound is always compared to the control experiment carried out under the exact same conditions. Among all the ZINC compounds, only DJ0010 and DJ0016 show concentration dependent inhibition effects. Note that compound DJ 0010 causes the rate of iron mobilization to drop ~ 50% at a concentration of 5 mM (Figure 4-4G blue trace), and compound DJ 0016 causes nearly complete inhibition at 9.0 mM (Figure 4-4J cyan trace).

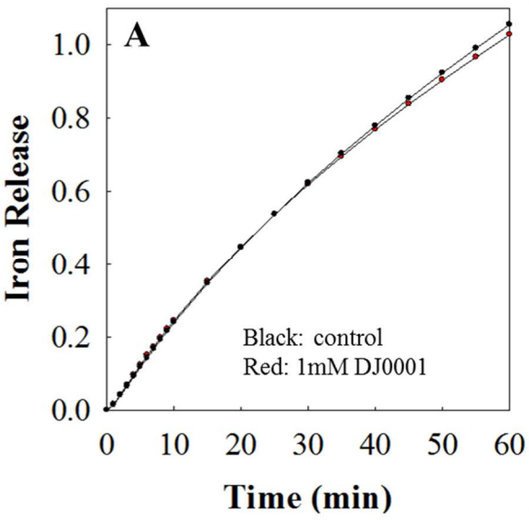
A
Iron Release
Time (min)
Black: control
Red: 1mM DJ0001

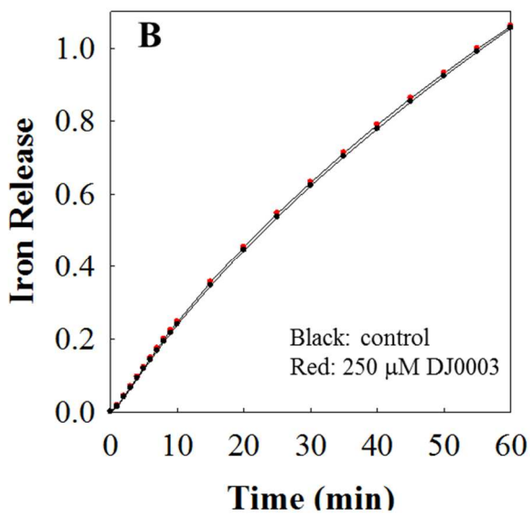
B
Iron Release
Time (min)
Black: control
Red: 250 µM DJ0003

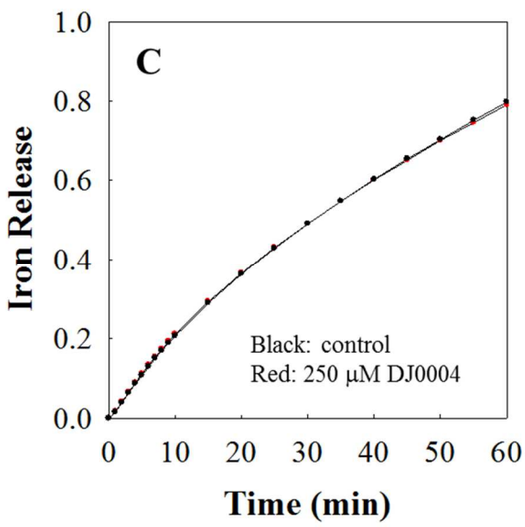
C
Iron Release
Time (min)
Black: control
Red: 250 µM DJ0004

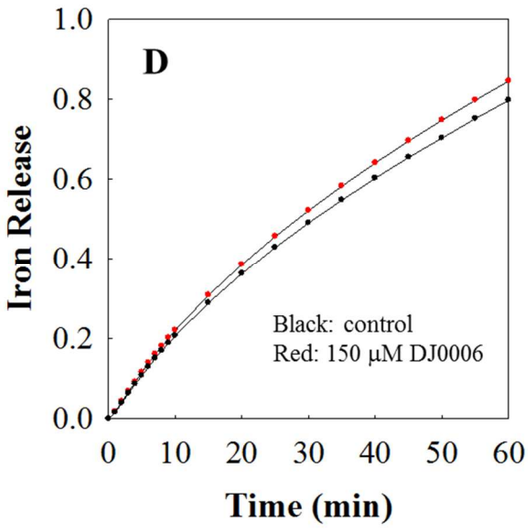
D
Iron Release
Time (min)
Black: control
Red: 150 µM DJ0006

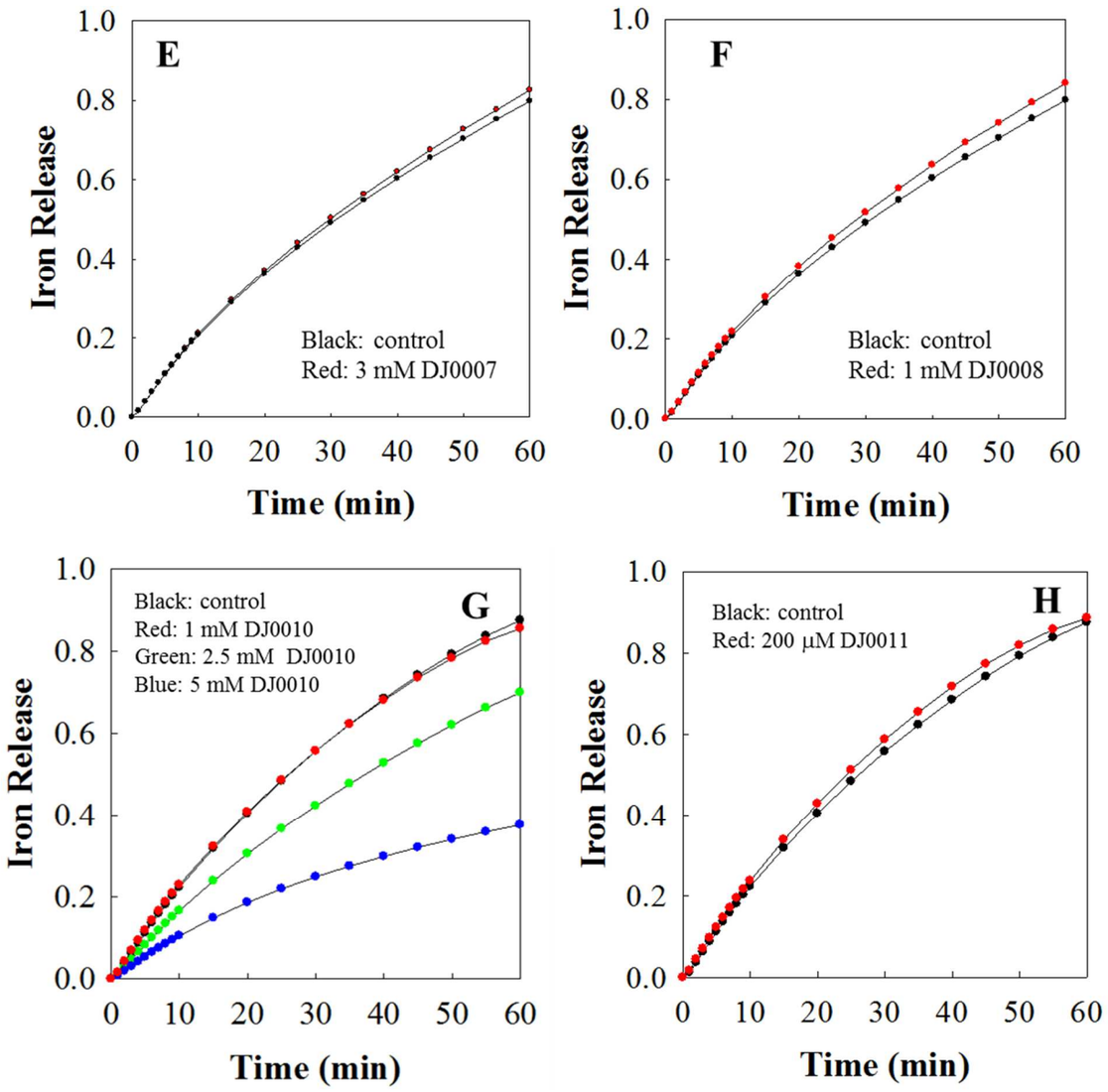
E
Black: control
Red: 3 mM DJ0007
F
Black: control
Red: 1 mM DJ0008
G
Black: control
Red: 1 mM DJ0010
Green: 2.5 mM DJ0010
Blue: 5 mM DJ0010
H
Black: control
Red: 200 µM DJ0011
Iron Release
Time (min)

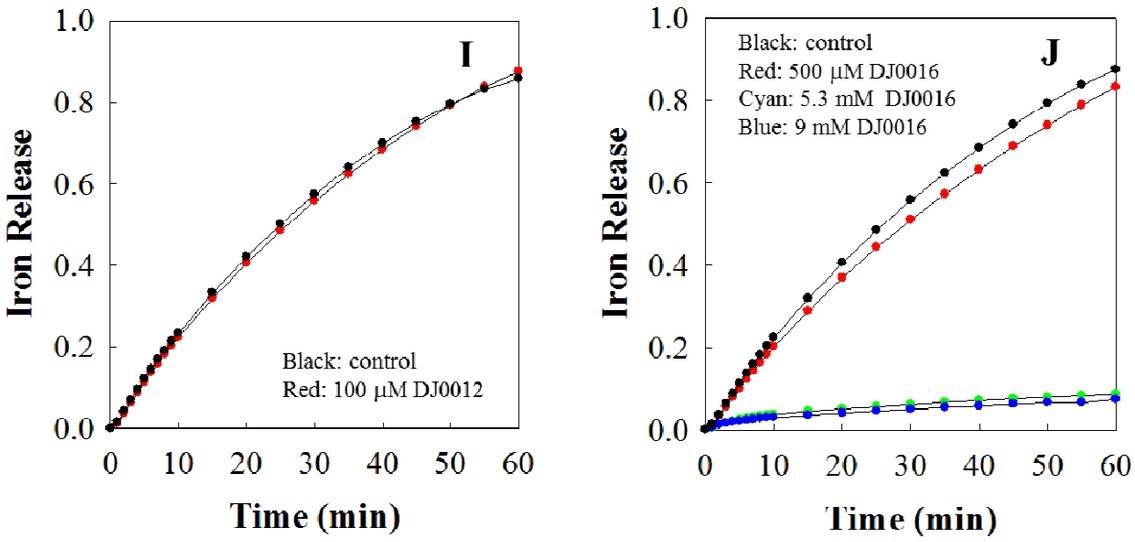

Figure 4-4 Iron mobilization from BfrB in the presence of different compounds identified to bind BfrB at the Bfd binding site from an *in silico* screen of the ZINC database (A-J). The largest concentration of compound in each of the plots corresponds to a value close to the solubility of the compound in phosphate buffer containing 10% (v/v) DMSO

Discussion

Factors affecting the BfrB iron mobilization efficiency

The main challenge of using the assay of mobilization of iron from BfrB as a method to detect the *in vitro* inhibition of the compounds lies in that many factors in the system could affect the iron mobilization efficiency, including the molar ratio of the proteins, concentration of NADPH, pH, temperature, etc.

The first parameter we sought to optimize is the molar ratio of Bfd to BfrB in the system. Our studies suggested that with a ratio [Bfd]/[BfrB] < 5 and 40-fold excess of FPR, the efficiency of iron release shows a dependency on the concentration of Bfd. The higher the ratio, the faster the iron release. However, when the [Bfd]/ [BfrB] reaches 5, the rate of iron release

reaches its maximum and is not affected by a higher [Bfd]/ [BfrB]. This suggests that for facilitating iron mobilization from BfrB, there will be an unnecessary excess of Bfd if the Bfd concentration is greater than 5 times of the BfrB concentration in the system. Consequently, the excess Bfd would only add to the cost of running the assay. However, if the [Bfd]/[BfrB] <5, any slight (pipetting) error in the addition of Bfd and BfrB to the system would cause a change in the rate of iron release, which would make the assay less reproducible. Consequently, we used [Bfd]/[BfrB] = 5 for all the assays.

The second parameter is the ratio of [FPR]/[BfrB]. We found that a lower concentration of FPR leads to a slower iron mobilization rate. Consequently, lowering the concentration of FPR to [FPR]/BfrB < 30 may be beneficial to detect inhibition by weak binders, such as fragments. This could be attributed to the idea that reducing FPR concentration would limit the electron transfer from NADPH to Bfd. Nevertheless, the data show that as the compounds become stronger binders, the functional developed here can be a useful guide to select compounds capable of blocking the BfrB/Bfd interaction and therefore preventing the mobilization of iron in BfrB.

References

1. Wang, T., et al., *Fragment-based drug discovery and molecular docking in drug design.* Curr Pharm Biotechnol, 2015. **16**(1): p. 11-25.
2. Juillerat-Jeanneret, L. and F. Schmitt, *Chemical modification of therapeutic drugs or drug vector systems to achieve targeted therapy: looking for the grail.* Med Res Rev, 2007. **27**(4): p. 574-90.
3. Newman, D.J., *Natural products as leads to potential drugs: an old process or the new hope for drug discovery?* J Med Chem, 2008. **51**(9): p. 2589-99.
4. Gribbon, P. and A. Sewing, *High-throughput drug discovery: what can we expect from HTS?* Drug Discov Today, 2005. **10**(1): p. 17-22.
5. Murray, C.W. and D.C. Rees, *The rise of fragment-based drug discovery.* Nat Chem, 2009. **1**(3): p. 187-92.
6. Joseph-McCarthy, D., et al., *Fragment-based lead discovery and design.* J Chem Inf Model, 2014. **54**(3): p. 693-704.
7. Bollag, G., et al., *Clinical efficacy of a RAF inhibitor needs broad target blockade in BRAF-mutant melanoma.* Nature, 2010. **467**(7315): p. 596-9.
8. Edink, E., et al., *Fragment growing induces conformational changes in acetylcholine-binding protein: a structural and thermodynamic analysis.* J Am Chem Soc, 2011. **133**(14): p. 5363-71.
9. Baker, M., *Fragment-based lead discovery grows up.* Nat Rev Drug Discov, 2013. **12**(1): p. 5-7.
10. Fattori, D., *Molecular recognition: the fragment approach in lead generation.* Drug Discov Today, 2004. **9**(5): p. 229-38.

11. Hopkins, A.L., C.R. Groom, and A. Alex, *Ligand efficiency: a useful metric for lead selection.* Drug Discov Today, 2004. **9**(10): p. 430-1.

12. Kuntz, I.D., et al., *The maximal affinity of ligands.* Proc Natl Acad Sci U S A, 1999. **96**(18): p. 9997-10002.

13. Keskin, O., et al., *Principles of protein-protein interactions: what are the preferred ways for proteins to interact?* Chem Rev, 2008. **108**(4): p. 1225-44.

14. ; Available from: zinc.docking.org.